RIGA TECHNICAL UNIVERSITY

Līga Maskova

ESTIMATION AND EXTENSION OF THE CYCLE LIFE OF $LiNi_xCo_YMn_{1-X-Y}O_2$ CATHODE MATERIAL FOR Li-ION BATTERIES

Doctoral Thesis

RTU Press
Riga 2026

RIGA TECHNICAL UNIVERSITY
Faculty of Natural Sciences and Technology
Institute of Technical Physics

Līga Maskova
Doctoral Student of the Study Programme "Chemistry, Materials Science and Engineering"

ESTIMATION AND EXTENSION OF THE CYCLE LIFE OF $LiNi_xCo_yMn_{1-x-y}O_2$ CATHODE MATERIAL FOR LI-ION BATTERIES

Doctoral Thesis

Scientific supervisors:
Dr. phys.
GINTS KUČINSKIS
Professor Dr. habil. phys.
MĀRIS KNITE

Riga 2026

The doctoral thesis was carried out at the Faculty of Natural Sciences and Technology, Riga Technical University, Institute of Technical Physics, Material Physics Laboratory in the period from September 2021 to January 2026.

SCIENTIFIC SUPERVISORS:

Dr. phys. Gints Kucinskis

Dr. habil. phys., Professor Maris Knite

The work has been carried out as part of the Latvian Council of Science project “Cycle life prediction of lithium-ion battery electrodes and cells, utilizing current-voltage response measurements”, project No. LZP-2020/1–0425 and the M-Era.net project "Inert Coatings for Prevention of Ageing of NMC Cathode for Lithium-Ion Batteries" (InCoatBat), Project Reference Number 10341.

The work has been completed with the support of a PhD grant from the project No 5.2.1.1.i.0/2/24/I/CFLA/003 "Implementation of consolidation and management changes at Riga Technical University, Liepaja University, Rezekne Academy of Technology, Latvian Maritime Academy and Liepaja Maritime College for the progress towards excellence in higher education, science and innovation" funded by the EU Recovery and Resilience Facility

Submitted for defense at the RTU P-02 Promotional Council of the Materials Science branch of the Riga Technical University in 2025.

ACKNOWLEDGEMENTS

Above all, my appreciation extends towards both of my scientific supervisors – Gints Kucinskis and Maris Knite – who led me to become a more independent and capable researcher. Their guidance, efforts, and time is what will shape my future as a scientist. Besides my direct supervisors, I would like to thank all my colleagues, also from other laboratories, for their guidance. In addition to being extremely helpful and forthcoming, most of my colleagues have genuinely cared for me and helped me through some tough times, which gave me strength to continue – for this I wish to thank everyone, but especially Rita Leimane, Gints Kucinskis, Inara Nesterova, Paula Malnaca, and Kaspars Kaprans!

I would not have completed this mountain of a task if I had not had the support of the people in my life. Firstly, I wish to express my full gratitude to my Sirsniņa – Andris Maskovs! Thank you for the unwavering support and holding space for me to grow. Secondly, I would like to thank the rest of my family with all my heart! My sisters – Rasa, Marta, Anna, and Laura – and my brothers – Miks and Māris – I can always rely on you for good laughs! Thirdly, thank you, Dad, so much, for supporting me! And, finally, I wish to thank you, Mom! You made me the person I am today.

My gratitude also extends to my friends who have been very patient with me throughout the thesis-writing journey and are just a joy to be around! Thank you, Ībļi (Zane, Daira, and Ralfs), Dita, Alma, Haralds, Kristīne, and Dace!

Finally, I would like to acknowledge my little Peciņa. Although never here, you gave me the strength to finish this and carry on, and I will love you forever…

Thank you!

ANNOTATION

This doctoral thesis research focuses on two key aspects of the lithium-ion battery (LIB) life cycle: its estimation and extension.

Within the first part battery ageing trends are explored via in-depth electrochemical characterization methods and correlations between simple voltage hysteresis measurements and the states of health (SoHs) of a battery are drawn, laying the groundwork to a possible method for easy SoH determination of used batteries. The second part of the research is focused on preventing the ageing of LIBs by mitigating degradation of the cathode material via surface coating. Here, the importance of a proper reference for correct evaluation of the effects from coating is also highlighted.

A meta-analysis comprising more than 40 literature sources is conducted within the literature review. It compiles the improvements to the capacity retention from coating or doping the cathode active material, indirectly revealing the main degradation mechanisms – surface or bulk based – plaguing $LiNi_xCo_yMn_{1-x-y}O_2$ (NCM) cathode materials of different compositions.

ANOTĀCIJA

Šajā doktora disertācijā tiek pētīti divi galvenie litija jonu akumulatoru (LIB) dzīvildzes aspekti: tās noteikšana un pagarināšana.

Pirmajā daļā, izmantojot padziļinātas elektroķīmiskās raksturošanas metodes, tiek pētītas akumulatora novecošanās tendences, un tiek veidotas korelācijas starp vienkāršiem sprieguma histerēzes mērījumiem un akumulatora veselības stāvokli (SoH), kas varētu kalpot par pamatu metodei, ar kuru iespējams viegli noteikt lietotu akumulatoru novecošanās stāvokli un dzīvildzi. Pētījuma otrā daļa ir vērsta uz LIB novecošanās novēršanu, mazinot katoda materiāla degradāciju, izmantojot virsmas pārklājumu. Šeit tiek uzsvērta arī atbilstoša references parauga nozīme, lai adekvāti novērtētu tieši pārklājuma ietekmi.

Literatūras apskatā iekļauta arī metaanalīze, kas ietver vairāk kā 40 publikācijas. Tajā apkopoti ciklēšanas stabilitātes uzlabojumi, pārklājot vai leģējot katoda aktīvo materiālu, netieši atklājot galvenos degradācijas mehānismus – virsmas vai tilpuma –, kas skar dažāda sastāva $LiNi_xCo_yMn_{1-x-y}O_2$ (NCM) katodmateriālus.

TABLE OF CONTENTS

Glossary 7
Introduction 9
Theses to Defend 12
1. Theoretical Background 13
1.1 Li-ion batteries and materials 13
1.2 Li-ion battery ageing 17
1.3 Degradation mechanisms of NCM cathodes 22
1.4 Cathode degradation mitigation 36
1.5 Summary of NCM cathode degradation and mitigation 43
2. Experimental 45
2.1 Materials 45
2.2 Methods 45
3. Results and Discussion 52
3.1 State of Health estimation from voltage hysteresis 52
3.2 NCM ageing mitigation by wet-chemical coating synthesis 58
4. Conclusions 74
References 76
Approbation 92

GLOSSARY

AIP – aluminum isopropoxide, $Al(OC_3H_7)_3$
ALD – atomic layer deposition
BV – Butler-Volmer
CAM – cathode active material
CC – constant current
CCCV – constant current, constant voltage
CE – Coulombic efficiency
CEI – cathode-electrolyte interphase
CTM – charge transfer multiplet
CVD – chemical vapor deposition
EDS – energy-dispersive X-ray spectroscopy
EoL – end of life
EV – electric vehicle
FEC – fluoroethylene carbonate
FIB – focused ion beam
HR-TEM – high resolution transmission electron microscopy
ICP-MS – inductively coupled plasma mass spectrometry
ICP-OES – inductively coupled plasma optical emission spectroscopy
IRMS – isotope ratio mass spectrometry
LAM – loss of active material
LCO – $LiCoO_2$
LFP – $LiFePO_4$
LIB – Li-ion battery
LLI – loss of lithium inventory
NCA – $LiNi_xCo_yAl_{1-x-y}O_2$
NCM – $LiNi_xCo_yMn_{1-x-y}O_2$
NEXAFS – near-edge X-ray absorption fine structure spectroscopy
NMP – N-methyl-2-pyrrolidone
OCV – open circuit voltage
OEMS – online electrochemical mass spectrometry
PVDF – polyvinylidene fluoride
RLC – residual lithium compound
SEI – solid-electrolyte interphase
SEM – scanning electron microscopy
SoC – state of charge
SoH – state of health
STEM – scanning transmission electron microscopy

TEM – transmission electron microscopy
TM – transition metal
TTE – 1,1,2,2-tetrafluoroethyl-2,2,3,3-tetrafluoropropyl ether
VC – vinylene carbonate
XAS – X-ray absorption spectroscopy
XPS – X-ray photoelectron spectroscopy
XRD – X-ray diffraction

INTRODUCTION

Lithium-ion batteries (LIBs) have become indispensable in modern energy storage applications, powering everything from consumer electronics to electric vehicles. Their widespread application results in large amounts of waste generated recycling of which requires plenty of energy and human resources. Understanding and limiting the rate of ageing of LIBs and their components, mainly the cathode material, would thus decrease the amount of battery waste generated.

A key insight into LIB ageing pertains to the evolution of voltage hysteresis during battery cycling. As the cell degrades or is subjected to higher currents, the hysteresis in the charge-discharge curve widens. Within the scope of this thesis a correlation between state-of-health (SoH) and voltage hysteresis has been established for state-of-art $LiNi_{0.8}Co_{0.1}Mn_{0.1}O_2$ (NCM811) LIBs, allowing SoH estimation via two methods: a direct function of hysteresis which is linear above 70% SoH and exponential below and through a fitting of C rate measurements with a Butler–Volmer-like function. These tools present non-invasive methods to diagnose battery health.

Among the various cathode chemistries employed, nickel-rich layered oxide materials, particularly $LiNi_xCo_yMn_{1-x-y}O_2$ (NCMs), have emerged as promising candidates due to their high energy density and relatively low cost. However, the increased nickel content that enhances capacity also introduces critical challenges related to material degradation, especially during prolonged cycling and high-voltage operation[1]. Understanding and mitigating the degradation mechanisms of NCM cathodes, especially those with high nickel content, is therefore essential for extending battery life and ensuring reliable performance.

Ageing in NCM cathode materials manifests through both surface and bulk degradation, with bulk degradation becoming increasingly prominent at higher states of charge (SoC), particularly beyond 80%[2]. For high-Ni content NCMs (≥ 80%), such SoC levels are reached at lower voltages (~4.3 V) compared to lower-Ni variants (~4.6 V), making them more susceptible to structural degradation such as microcracking. This highlights a fundamental limitation in the structural resilience of high-Ni materials, requiring strategies that go beyond surface stabilization alone, such as doping or structural modification.

To address these challenges, numerous strategies including surface coating and elemental doping have been explored. A meta-analysis of ageing mitigation strategies (coating and doping) conducted in this thesis reveals a composition-dependent trend: while surface protection plays a dominant role in NCM111, doping becomes increasingly critical for NCM622 and reaches equal importance with surface protection in NCM811. These findings underscore the necessity of combining surface protection and doping for effectively stabilizing high-Ni NCMs where bulk-related degradation dominates.

Additionally, the efficacy of surface coatings is influenced not just by the coating material, but also by the processing methods. Wet-chemical procedures, commonly used for applying coatings, can inadvertently introduce degradation through solvent interactions, such as ethanol washing leading to carbonate impurity formation as demonstrated in this work. However, subsequent

sintering has been shown to reverse much of this degradation both in literature[3] and in this work. This emphasizes the importance of carefully designed reference samples when evaluating coating effectiveness, as misattributing improvements to the coating effect alone can lead to misleading conclusions.

In this context, a wet-chemically applied $Al_2O_3/LiAlO_2$ coating developed in in this work has shown promising results in comparison to a properly prepared reference sample. For NCM111, this coating method improved capacity retention from 65% in pristine samples to 79% in reference samples, to 88% in coated samples after 500 cycles at 1 C. Similarly, the capacity retention of NCM811 improved from 44% in re-sintered reference material to 54% in coated samples. While the absolute improvement is less pronounced in NCM811, due to the dominance of microcracking which coatings cannot fully prevent, the relative gain still represents a meaningful advancement in extending battery lifespan.

Aim of the Thesis

The aims of this work are to explore the possibility of using simple voltage hysteresis measurement for the determination of the SoH of a LIB, as well as prolong the cycle life of NCM cathodes with the use of a protective coating, simultaneously establishing a proper reference for comparison.

Tasks

Establish a relationship between SoH and voltage hysteresis and determine the best fit function to describe this relationship. Evaluate the possibility of determining the SoH from a simple voltage hysteresis measurement. Consider alternatives.

Conduct a meta-analysis on coating and doping effect on capacity retention and determine the dominant ageing mechanisms in NCM cathode materials based on Ni content.

Develop a sustainable wet-chemical method to coat NCM cathodes with an inert protective coating. Establish a proper reference for the coating study. Achieve cycle life extension for the coated sample when compared to the proper reference.

Scientific novelty

Based on available information, there is no simple method to determine the SoH of a given battery of unknown history, as the SoH of a battery is usually based on its initial state. Thus, knowing the SoH at any point would require storing large amounts of data or knowing where the battery came from. We explore the possibility of using a simple voltage hysteresis measurement to determine the SoH with a certain precision. This could greatly simplify the assessment of used batteries for possible second life applications.

Currently high-nickel NCMs (Ni $\geq$ 80%), despite their advantageous capacity (> 200 mAh/g) are not dominating the market due to their intrinsic stability issues. Coating the active material has shown to improve stability, however, usually it is done by slow and costly methods (ALD) or toxic substances like toluene or trimethyl aluminium are used. In the second part of this work we focus on improving the stability of the state-of-art NCM cathode materials by developing a coating

method which omits often used harmful chemicals and is possible to up-scale, thus prolonging the lifetime of NCM batteries sustainably.

Practical significance

A simple method for the determination of the SoH of batteries from scrap yards could enable assessment of their possible use in second-life applications, thus reducing the amount of dangerous waste which needs to be recycled.

When considering the currently used cathode materials with the highest energy densities, most of them contain cobalt or suffer from stability issues. Our wet-chemical coating method is sustainable and can be transferred to industrial scale to enable low-Co, high energy density cathode materials to enter the market.

Theses to Defend

1. Voltage hysteresis increases as the state of health (SoH) of NCM811-lithium half-cells decreases, allowing SoH assessment based on this correlation using a quick and simple voltage hysteresis measurement.
2. Improvement in capacity retention from coating or doping NCM cathode materials with different Ni content indirectly indicates the dominant (surface or bulk) aging mechanisms in these materials – larger improvements from surface coating indicate dominant surface aging mechanisms (formation of a cathode-electrolyte interphase, dissolution of transition metals, surface phase transitions, and oxygen evolution), while larger improvements from doping indicate dominant bulk aging mechanisms (cation mixing, microcrack formation).
3. The chemical coating process, involving mixing the material to be coated in a solvent and heating it at high temperatures, changes the surface structure and composition of the material, which, if left unaccounted for, leads to ambiguous conclusions about how the effect of the coating itself changes cycling stability.
4. A simple, sustainable, ethanol-based wet-chemical coating synthesis on NCM cathode materials with different Ni compositions improves their long-term cycling stability in Li-ion cells by hindering degradation of the cathode material surface.

1. THEORETICAL BACKGROUND

1.1 Li-ion batteries and materials

Li-ion batteries (LIBs), the most popular kind of rechargeable batteries, have been studied for decades. Although lithium shows good performance and light weight, due to its high reactivity and fire hazard, it was only first commercialized by Sony in 1991, when the risks were somewhat neutralized by careful engineering. Coinciding with the wireless revolution, the emergence of rechargeable batteries in the 90's paved a way for more convenient and sustainable mobile phones.

A typical LIB consists of a cathode, anode, separator, electrolyte, current collectors, all enveloped in a battery cell casing (fig. 1.1). LIB stores electrical energy in the form of chemical potential. Lithium ion is the main charge carrier within the battery, whereas in the external circuit it is the electron. When the battery is charged, Li^+ exits the cathode and travels through the ion-conducting electrolyte to the anode side while an electron leaves the cathode to compensate for the loss of a positive charge and reaches the anode via the external circuit, since the electrolyte is an electronic insulator. In the anode Li^+ once again combines with the electron and intercalates into the anode as Li. During the discharge process the reverse process occurs. The driving force of the spontaneous discharge reaction is the difference in lithium chemical potential between the cathode and anode (high potential, weaker bonding in the anode, low potential, stronger bonding in the cathode). The electrolyte-soaked separator between the electrodes allows ion diffusion but prevents contact between the electrodes to avoid short circuiting the battery cell.

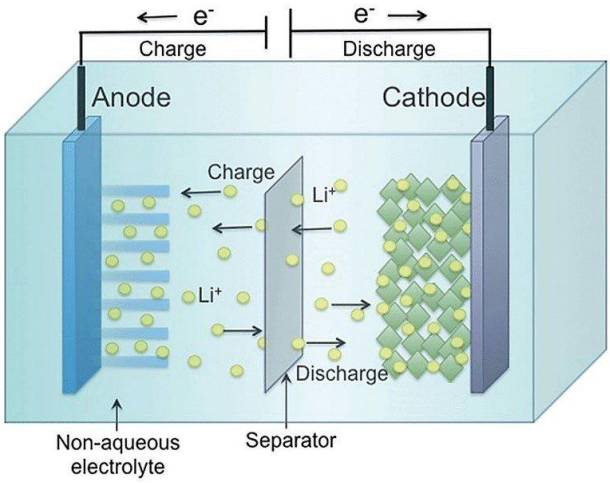

Fig. 1.1. Li ion battery composition and working principle[4].

The most important components of LIBs, which ensure that energy can be stored and obtained, are the cathode and anode materials. The operating voltage and capacity of a battery cell is mainly limited by the cathode properties, whereas the anode hosts lithium in a charged cell. The cathode and anode materials mainly used in LIBs are discussed in further sections.

Cathode materials

Cathode materials for rechargeable LIBs have been extensively studied for more than 30 years, yet the demand for ever higher capacities, longer lifetimes and more power is never-ending, driving the research of battery scientists. One of the first cathode materials proposed for LIBs was layered TiS_2, which was reported by Stanley Wittingham in 1976[5]. However, with its relatively low voltage vs. Li/Li^+ (~2.2 V), TiS_2 cathode could not achieve high energy densities. Realizing that oxides may stabilize the oxidized transition metals (TMs) better than the sulfides, allowing for more lithium to be extracted, John B. Goodenough along with co-workers demonstrated lithium extraction from $LiCoO_2$ that showed voltage vs Li/Li^+ of 4.0 V in 1980[6]. However, struggles with arousing companies' interest led to the commercialization of the first rechargeable battery with a $LiCoO_2$ cathode and graphite anode only a decade later. Since then, oxide cathode materials have been on the forefront of LIB cathode material research.

One way to classify LIB oxide cathode materials is by their crystal structure. The three main types are olivine ($LiMPO_4$, where M = Mn, Fe, Ti, etc.), layered ($LiMO_2$, where M = Co, Ni, etc.), and spinel (LiM_2O_4, where M = Mn, V, Ti, etc.) which differ in the dimensionality of Li diffusion and pathways. In the spinel materials Li moves in three dimensions from one tetrahedral site to another via an intermediate octahedral site, in a layered oxide Li diffusion occurs in 2 dimensions (within the Li layer) from one octahedral site to another via an intermediate tetrahedral site[7], whereas in an olivine material Li diffuses in one direction between octahedral sites[8]. Due to the three-dimensional lithium diffusion pathways, spinel oxides offer good Li conductivity. Furthermore, the material offers good electric conductivity and great stability upon lithium extraction, meaning that spinel oxide cathodes offer high power and good reversibility of lithium insertion-extraction. Olivine materials, on the other hand, exhibit inferior electrochemical properties due to the lower conductivity, however, their intrinsic safety and lower cost makes them an attractive alternative for energy storage[9]. Finally, layered oxides have the highest energy density, and are discussed in detail below.

Layered oxides

$LiCoO_2$ (LCO) was the first layered oxide cathode material developed for rechargeable LIBs[6] and still used in many LIBs nowadays. However, delithiation of LCO by more than 50 % can lead to irreversible oxygen oxidation to O_2, cell bloating and structural collapse[7]. This limits the practical capacity to approximately 140 mAh/g and has driven research into alternative compositions that replace Co with other TMs, such as $LiNiO_2$, $LiMnO_2$, $LiNi_xCo_yMn_{1-x-y}O_2$, $LiNi_xCo_yAl_{1-x-y}O_2$. Among these alternatives, $LiNi_xCo_yMn_{1-x-y}O_2$ (NCM) materials have gained significant popularity.

Like $LiCoO_2$, NCMs exhibit an O3 layered structure, where "O3" refers to lithium occupying octahedral sites and three layers of lithium, TMs, and oxygen forming a repeating unit[10]. These materials belong to the *R3m* space group. The primary particles in these cathode materials are composed of alternating layers of TMs and lithium, with atoms arranged in a hexagonal configuration and enclosed by face-sharing oxygen octahedra (fig. 1.2). Lithium ions can easily move along the 2D lithium plane as described before.

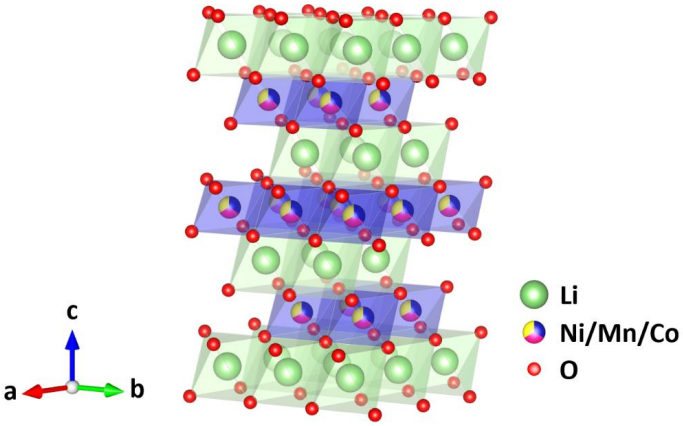

Fig. 1.2. Crystal structure of NCM cathode material[[11]*.

NCMs are divided into low Ni-content NCMs ($x<0.8$) and high Ni content NCMs ($x\geq0.8$). The significance of Ni comes from its charge compensation capabilities, thus increasing the practical capacity attainable at lower voltages. For example, the capacity of NCM111 (numbers denote the stoichiometric ratio of TMs in the material) in the voltage range 2.7 V - 4.3 V vs. Li/Li^+ is around 170 mAh/g, whereas NCM811 cycled under the same conditions can reach a capacity of 200 mAh/g. The theoretical capacity (obtained when all Li is extracted from the NCM lattice), however, is the same for all NCMs – around 275 mAh/g. The lower voltage required to access the same amount of capacity for higher Ni content NCMs may seem undesirable due to lowering the energy density, however, the operating voltage of higher Ni content NCMs is actually higher than that of lower Ni content NCMs[12], leading to practically higher energy densities. Additionally, to obtain higher capacity from NCM111 the voltage needs to be increased to 4.7 V, which is outside the electrochemical stability window of most liquid electrolytes. Thus, along with reducing the amount of cobalt in the material, research and industry strive for higher nickel content NCMs to achieve improved electrochemical performance.

* Author's original publication.

Anode materials

Although the gravimetric capacity of the battery is largely limited by the cathode, the performance and availability of anode materials also plays a role in designing low-cost, efficient LIBs. Generally, anodes are adjusted to the cathodes used in batteries – they usually have a slightly higher area and capacity to allow full utilization of the cathode's capabilities. Moreover, the anode stability plays a key role in battery degradation as well. Thus, careful consideration goes into designing anodes for LIBs to lower the weight of the battery without compromising the stability, and most importantly – to not limit the utilization of battery cathode.

Materials for LIB anodes include carbon-based materials with graphite as the most popular, silicon-based materials, alloy materials, and conversion-type TM compounds[13]. The two most popular materials for LIB anodes are graphite and silicon – the former shows excellent stability but a lower capacity and rate capability when compared to the latter. Silicon, with an impressive theoretical capacity of 4200 mAh/g and good rate performance is an excellent contender for applications where fast charging-discharging and high power output is necessary, however, the limited cycle life due to vast expansion upon lithiation leading to microcracking and rapid SEI growth on exposed surfaces currently prevents silicon to be utilized in long-term applications. Despite the progress in stabilizing silicon-based anode materials[14], [15], [16], graphite is still the most used anode material in commercial cells. Thus, it is also the material of choice for assembling full cells in this work. Besides full cells to test full battery performance half cells are assembled to deconvolute the results of both electrodes and study the cathode independently. The anode of choice in half cells is lithium metal, providing unlimited lithium supply and fast charging.

Graphite

The safety, availability, and reliable performance of graphite makes it the most commonly used anode material in commercial lithium-ion batteries[13]. The layered structure of graphite allows lithium ion insertion without major structural change to the graphite anode. Additionally, graphite ensures a decent capacity of 372 mAh/g in a fully lithiated state, which makes cathode materials, usually displaying lower gravimetric capacity, comprise a significantly higher proportion of the total weight of the battery cell.

During charging lithium in graphite anodes intercalates between the graphene sheets, increasing the interlayer distance. During battery charging solvated Li^+ is transported through the electrolyte to the anode where it intercalates into graphite particles by becoming de-solvated and migrating through the solid-electrolyte interphase (SEI) which forms during the first few charge cycles. After intercalating Li^+ diffuses within the graphite particle to allow further Li^+ intercalation until maximum capacity is reached as the stoichiometry reaches LC_6 for a fully charged graphite anode[17]. During discharging the reverse process occurs and Li^+ travels to the cathode.

Lithium

Lithium metal is considered to be the ideal anode material for LIBs with a virtually limitless gravimetric capacity, high rate of discharge, and a low and stable redox potential (-3.05 V vs.

reference hydrogen electrode) enabling high energy densities. For these reasons it is also the negative electrode of choice, acting as both the counter and reference electrode, when the performance of other battery electrodes (cathodes, other anodes) is to be studied in half cells. Although half cells are frequently utilized to study different LIB electrodes, it is important to keep in mind that the ageing of the lithium electrode, just like any other counter electrode, has a considerable contribution on the performance of the cell[18]. SEI growth and Li plating in the form of dendrites on the surface of the anode leads to rise in internal resistance and loss of lithium inventory, which may not be as crucial in cells with a lithium electrode. However, the growing dendrites may breach the separator and connect the two electrodes leading to short circuit in the battery cell.

Electrolyte and separator

The main role of the electrolyte in LIBs is Li^+ transport between the electrodes through the separator. Thus, good ionic conductivity and lithium ion transference of the electrolyte is a key factor in LIBs not to limit the rate capability of the cell[19]. Li^+ are transported between the electrodes in a solvated form (solvent molecules and anions coordinate around the Li^+ once it exits one electrode and leave the Li^+ when it enters the other electrode)[20], [21]. Thus, an additional consideration in enabling good rate performance in LIBs is the rate of solvation/de-solvation of lithium ions at the electrode interfaces[22].

There are many types of electrolytes that can be used in LIBs, ranging from aqueous electrolytes to solid-state electrolytes, however, in this study a standard organic electrolyte was used consisting of $LiPF_6$ salt dissolved in mixed carbonate solvents, since the focus of the study is on cathode materials rather than electrolytes. In some cases, additives such as fluoroethylene carbonate (FEC) or vinylene carbonate (VC) are added to the electrolyte[23] to form a stable, low-resistance SEI[24], prevent Li plating[23], or hinder electrolyte degradation[25].

The main role of the separator in the battery cell is to prevent contact between the anode and the cathode to avoid direct electron transport between the electrodes, thus, short-circuiting the battery. While the separator must be an electronic insulator, it must be porous to allow electrolyte percolation and ion transport between the electrodes. Although the separator itself is electrochemically inactive, it plays an important role in battery safety. Thus, separator research is focusing largely on reducing the size and weight of the separators without compromising battery safety[26].

1.2 Li-ion battery ageing

LIB ageing stems mainly from the ageing of battery components – the individual cells. The ageing within cells is related to the degradation of its components, mainly the anode, cathode and electrolyte. The degradation mechanisms are based on several interconnected physical and chemical phenomena which are yet to be explained and evaluated fully due to their complexity.

The degradation within battery cells can be classified under two main outcomes – loss of lithium inventory (LLI, from electrolyte and electrodes) and loss of active material (LAM, from electrodes). Both are evident from the eventual loss of capacity during battery cycling. The main degradation mechanisms within the cell which lead to LLI and LAM are

1) cathode related (NCM):
    - growth of a passivating cathodic solid-electrolyte interphase (CEI);
    - microcracking;
    - surface phase transitions from layered to spinel and rock salt;
    - oxygen evolution (associated with surface phase transitions);
    - TM dissolution and migration to the anode side;
    - cation mixing;
    - binder decomposition;
    - loss of contact between the cathode and current collector.
2) anode related (graphite):
    - continuous SEI growth;
    - structural changes, microcracking, and exfoliation;
    - li dendrite growth;
    - binder decomposition;
    - loss of contact between the anode and current collector.
3) electrolyte related (carbonate):
    - electrolyte decomposition and consumption at the anode, participation in SEI growth;
    - electrolyte reaction with the evolved oxygen at the cathode, participation in CEI growth.

Loss of lithium inventory (LLI)

Loss of lithium inventory (LLI) is one of the major ageing modes of LIBs. It occurs when lithium inside the battery can no longer participate in the charge-discharge reactions and becomes "dead lithium" within the cell. The causes of LLI are

- decomposition of electrolyte – $LiPF_6$ can react with water present in the cell from adsorbing to electrodes or other cell components, or HF formed in the cell during operation. Electrolyte decomposition products also continuously participate in forming the SEI layer during battery cycling[27];
- growth of SEI and CEI – lithium in the form of electrolyte decomposition products or inorganic species (LiF, Li_2CO_3) participates in the growth of the passivating layers on top of both electrodes[28], [29];
- lithium plating – lithium plating on the negative electrode occurs mainly when charging at low temperatures or high currents[30], [31], [32]. Low temperatures slow down lithium diffusion in the anode causing Li to accumulate on the surface. Similarly, high

currents cause lithium ions to arrive at the anode surface faster than they can intercalate and diffuse in the anode, again causing an accumulation of lithium ions on the surface.

Due to LLI the amount of lithium available for electrochemical reactions is lowered, thus decreasing the capacity of the cell.

Loss of active material (LAM)

Loss of active material (LAM) can occur from both the positive and the negative electrode[33]. It usually involves degradation of the active material and binder, loss of contact between the electrode and current collector and loss of contact within the electrode.

- Loss of cathode active material occurs when, due to different degradation mechanisms, discussed in detail in the subsequent chapters, part of it becomes electrochemically inactive. The degradation mechanisms include microcracking, surface phase transitions, oxygen loss, and TM dissolution.
- Loss of anode active material is analogous to LAM of the cathode, and it occurs due to particle cracking, graphite delamination (in graphite electrodes), lithium plating. For more in-depth explanation of anode-related ageing, please refer to the following articles[32], [34], [35], since the focus of this work is the cathode material.

Ageing determination

The various degradation phenomena, although mostly known, are not yet fully investigated and understood. However, they clearly lead to battery capacity fading, or deterioration of the state-of-health (SoH) during cycling. The SoH at a given point in battery lifetime is determined by expressing the capacity of the battery at any cycle as percentage of the initial capacity of the battery. SoH is a useful parameter which shows how close to the end of life (EoL) a given battery is. The cycle when SoH reaches 80 % is generally accepted to be the EoL of a battery. However, such batteries can still give sufficient energy for second life applications such as stationary energy storage. The issue arises when a given battery's initial state is not known (e.g. a battery from an EV from a scrapyard) and only the capacity of the given cycle can be determined by charging and discharging the battery. In such cases a quick method to determine the SoH of a battery, which doesn't depend on the battery's history, would be preferential.

Prediction of the SoH can roughly be sorted in three distinct methods: data-driven approach, model-driven approach, and a combination of both. The data-driven approach implements artificial intelligence and machine learning from several data samples to build a predictive model[36], [37]. Although possessing relatively accurate predictive powers, this approach requires a large amount of data, is computationally very heavy and complex, and is thus very expensive and inconvenient for everyday applications. The model-driven approach utilizes parameters based on theory and empirical results to build a model based on the current knowledge on battery ageing[37], [38]. This approach similarly to the data-driven one can be computationally very complex, since the parameters which influence battery ageing are manifold, can evolve during battery ageing, and can

be interdependent. Combining both data-driven and model-based approaches may bring the predictive models closer to real-life situations when compared to simple model-based methods[39], however, it still does not allow the model to be transferred between different battery chemistries or reduce the computational complexity and processing time[40]. Thus, great effort has been dedicated to finding simple and fast methods for SoH estimation of LIBs.

State of health as a function of voltage hysteresis

As aforementioned, degradation of LIBs is a complex phenomenon which involves several interdependent ageing mechanisms. However, although ageing mechanisms are various and different, many of them are reflected in the voltage hysteresis of the charge-discharge curve[41], [42] (fig. 1.3). Voltage hysteresis is the sum of the overpotentials of the charge and discharge curve at any given cycle. Overpotential is the difference between the open circuit voltage (OCV) and the operating voltage of the cell. Usually during charge the operating voltage is higher than the OCV (more energy is needed for charging the cell than is stored in it) whereas during discharge it is lower (less energy is obtained from the cell than is stored in it). Overpotential represents total energy dissipation during charging and discharging of the cell[43], [44]. Hence, as a battery cell ages and internal resistance grows, more energy is required to overcome it, and the overvoltage and voltage hysteresis grows.

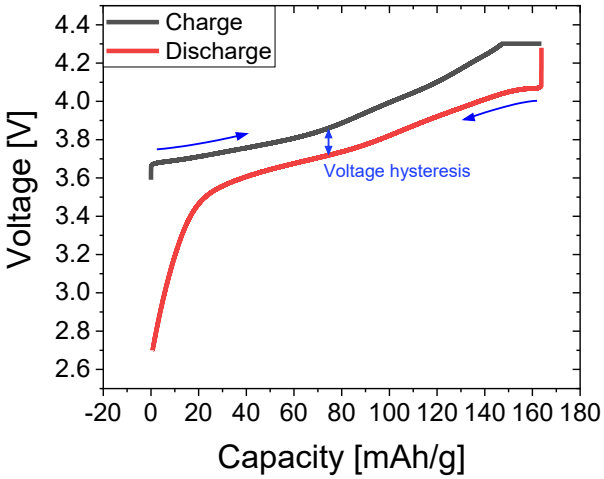

Fig. 1.3. Voltage hysteresis of a typical charge-discharge curve of a LIB containing an NCM811 cathode.

The total overpotential is the sum of several smaller overpotentials originating from different resistances within the battery. These include charge transfer resistance due to activation energy of the charge transfer reactions at the electrode surfaces, lithium ion diffusion resistance in the

electrolyte and in the bulk of the electrode materials, contact resistance between the different materials of the electrodes and current collectors, and ohmic resistance from electronic conductivity of the current collector and electrode active materials and ionic conductivity of the electrolyte[45].

Specific current j as a function of the voltage difference between the electrode and bulk electrolyte η (overpotential) is expressed by the Butler-Volmer (BV) equation:

$$j = j_0 \left[\exp\left(\frac{\alpha_a z F}{RT}\eta\right) - \exp\left(-\frac{\alpha_c z F}{RT}\eta\right) \right] \quad (1.1)$$

where j_0 – exchange current density, A/m^2;

α_a – anodic charge transfer coefficient, dimensionless;

α_c – cathodic charge transfer coefficient, dimensionless;

F – Faraday constant, C/mol;

R – universal gas constant, J/(K·mol);

z – number of electrons transferred in an electrochemical reaction;

T – temperature, K

η – overpotential.

The exchange current density is analogous to the rate constant used to describe the kinetics of chemical reactions, the anodic and cathodic charge transfer coefficients are kinetic parameters usually ranging from 0.2 to 2 and describe how much one direction of the electrochemical reaction is favored over the other based on the applied potential, and for LIBs $z = 1$. The first and second terms in the parentheses of equation (1.1) describe the rate of the anodic and cathodic reaction, respectively, and the difference in these rates gives the net rate of reaction at an electrode.

The way that the anodic and cathodic reactions overtake one another at positive and negative potential respectively can be clearly seen in the graphical depiction of the BV equation (fig. 1.4).

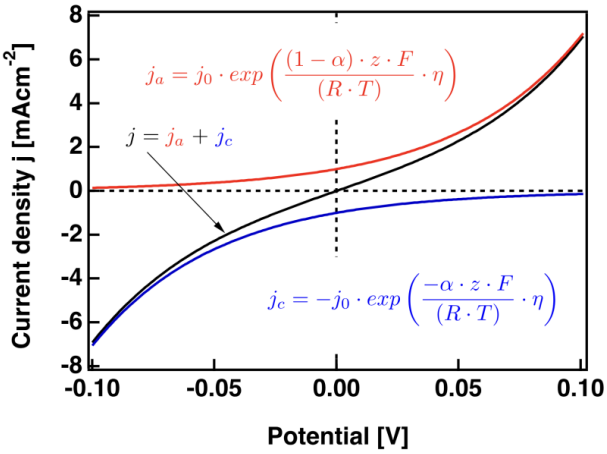

Fig. 1.4. Graphical depiction of the Butler-Volmer equation[46].

When a LIB is charged the cathode is delithiated, meaning that lithium is extracted from the lower energy, stronger bonding state in the cathode and inserted into the anode where it is bonded more weakly and has a higher energy. The Li^+ that exits the cathode has "lost an electron" (although the electron is lost by a TM in an oxide cathode for charge compensation purposes) in the process of oxidation and the anodic current or reaction (red line in fig. 1.4) dominates the overall current. The opposite is true for the discharge or lithiation process (blue line in fig. 1.4).

In this work we attempt to utilize the relationship between the SoH and voltage hysteresis to establish a straightforward method for the determination of the SoH of a given battery based on a simple voltage hysteresis measurement – a task which usually requires storing large amounts of data and high computational power. Here, we test the ability to determine the SoH from voltage hysteresis by fitting simple functions to the obtained data and calculating the error with which one could read the SoH value from the data plot if an unknown battery of the same composition was compared against it. Additionally, the SoH determination from one C rate measurement is explored as an alternative method.

1.3 Degradation mechanisms of NCM cathodes

The following sub-sections are based on the author's publication "A review of the degradation mechanisms of NCM cathodes and corresponding mitigation strategies"[11][*].

NCM cathodes contain 3 TMs – Ni, Co and Mn. While $LiMnO_2$ cannot be synthesized in the desired O3 layered structure and $LiNiO_2$ encounters structural and chemical stability issues, combining Ni, Co, and Mn enhances energy density and structural stability. Ni is the main redox

[*] Author's original publication.

active TM, Mn acts as a structural stabilizer, and Co improves both structural stability and electrical conductivity[7]. Economic considerations, geopolitical factors, and the scarcity of Co, combined with the growing demand for higher energy density, have shifted the composition of NCM towards Ni-rich materials. Consequently, NCM materials have evolved from NCM111, with the specific composition first reported in 2001 by T. Ohzuku et al.[47], to NCM532, NCM622, NCM811, and beyond (where the numbers indicate the ratio between Ni, Co, and Mn). Unfortunately, although energy density increases with higher Ni content, high-Ni NCMs also experience a more rapid capacity decline during cycling (fig. 1.5). This challenge has spurred efforts to better understand and extend the cycle life of Ni-rich NCMs while taking advantage of their high energy density.

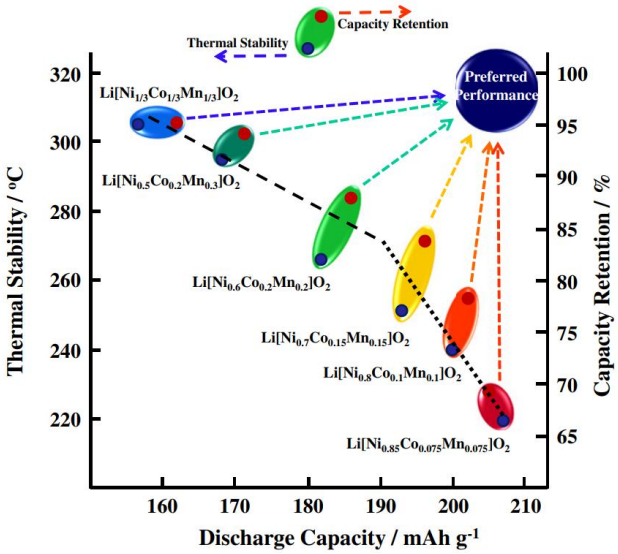

Fig. 1.5. discharge capacity, capacity retention, and thermal stability of NCMs with different Ni composition[48].

The degradation mechanisms associated with the NCM cathode are illustrated in fig. 1.6 and primarily arise from two sources: the synthesis and handling of the cathode material and the operation of the battery (lithiation-delithiation of the cathode) once the cathode is integrated into the cell. Both aspects are examined in detail in subsequent sections. During synthesis it is crucial to control lithium content to prevent under-lithiation of the active material which can lead to subpar performance. However, when excess lithium is used in active material synthesis, it can remain on the particle surface and participate in the formation of residual lithium compounds (RLCs). RLCs can also grow during improper handling and storage of the NCM material, exposing it to air. RLCs lead to lithium inventory loss in the assembled cell and participate in undesirable reactions with

the electrolyte. Besides handling and storage, NCM undergoes the most critical and complex degradation during cycling.

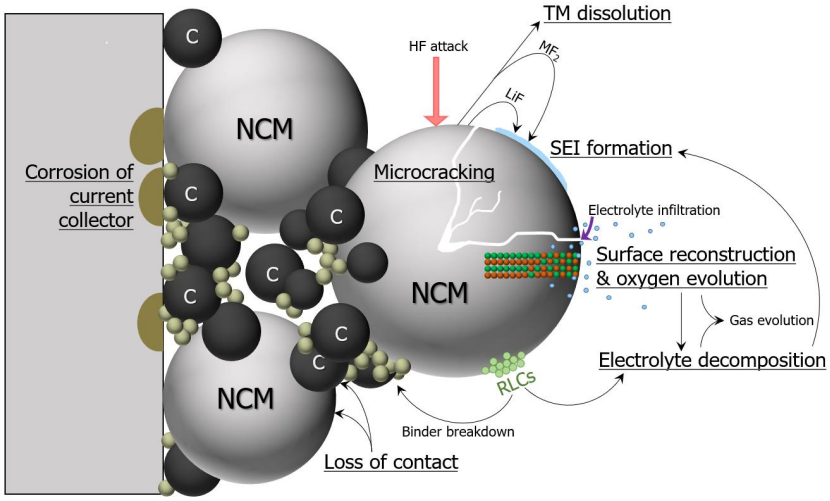

Fig. 1.6. NCM cathode degradation mechanisms[11][*].

Key degradation mechanisms for any NCM cathode material during cycling include CEI formation, surface reconstruction, oxygen release, TM dissolution, and microcracking, creating new reactive surfaces. These degradation mechanisms are deeply interconnected and can be a trigger for further degradation outside of the cathode. The wide range of decomposition mechanisms (with some causing secondary degradation effects) and the variety of NCM compositions contribute to the challenges in fully understanding the relative contribution and significance of each degradation mechanism in quantifiable terms.

Degradation during synthesis and storage

Various synthesis techniques have been developed for NCM, including sol-gel, hydrothermal, solid-state, and pulse combustion methods[49]. Among these, co-precipitation is the most commonly used approach[50]. This process involves the co-precipitation of TM salts, typically sulfates, in precise stoichiometric ratios. These salts are chelated by ammonia and then reacted with hydroxide ions in an aqueous solution, forming an NCM precursor. After drying, the TM hydroxide precursor is blended with a lithium source (such as $LiOH{\cdot}H_2O$ or Li_2CO_3) and subjected to high-temperature sintering (approximately 900 °C) to produce the final $LiNi_xCo_yMn_zO_2$ compound. However, at elevated temperatures, lithium evaporation occurs due to its high vapor pressure, leading to nickel migration to lithium sites and increasing cation mixing[51], [52]. To mitigate

[*] Author's original publication.

these effects and maintain optimal performance, an excess of lithium is typically introduced during NCM synthesis. This excess is particularly important for Ni-rich NCM compositions, as nickel readily occupies lithium sites, exacerbating lithium sublimation. Since the same number of lithium atoms can be incorporated into NCM111 and NCM811 structures, but more lithium is added during NCM811 synthesis, a larger amount of residual lithium accumulates on the particle surface. Studies have also identified a correlation between nickel content in NCM and RLCs on the material's surface[48], [51], [53].

Ni-rich NCM materials exhibit heightened sensitivity to moisture (H_2O) and carbon dioxide (CO_2) due to their increasing alkalinity with higher nickel content[54], [55]. Exposure to ambient humidity or wet processing can result in Li^+/H^+ exchange[56], [57], contributing to the formation of RLCs as the lithium which is extracted from the structure reacts with O_2, CO_2, and H_2O, forming Li_2O, Li_2CO_3, and LiOH.

RLCs on the NCM surface can participate in several detrimental side reactions within a battery cell, reducing efficiency and stability:

1. Electrochemical decomposition of Li_2CO_3 via a peroxodicarbonate intermediate, generating singlet oxygen: $2Li_2CO_3 \rightarrow 4Li^+ + 4e^- + 2CO_2 + {}^1O_2$ (> 3.8 V)[58].
2. LiOH reaction with PVDF binder: $LiOH + (CH_2\text{-}CF_2)_n \rightarrow (CH{=}CF)_n + LiF + H_2O$.
3. LiOH reaction with $LiPF_6$ in the electrolyte: $LiOH + LiPF_6 \rightarrow 3LiF + PF_3O + H_2O$.
4. Li_2O reaction with H_2O generated by electrolyte degradation: $Li_2O + H_2O \rightarrow 2LiOH$.
5. RLCs reacting with hydrofluoric acid (HF), which is produced during electrolyte decomposition:
    a) $Li_2CO_3 + 2HF \rightarrow CO_2 + H_2O + 2LiF$;
    b) $LiOH + HF \rightarrow LiF + H_2O$;
    c) $Li_2O + HF \rightarrow LiF + H_2O$.

The presence of HF, which forms due to the decomposition of $LiPF_6$ in the electrolyte, further exacerbates battery degradation through reactions such as:

6. $LiPF_6 + H_2O \rightarrow LiF + PF_3O + 2HF$.
7. $PF_3O + H_2O \rightarrow HF + HPO_2F_2$.
8. $LiPF_6 + H^+ \rightarrow Li^+ + PF_5 + HF$.

HF generated from these reactions can attack RLCs on the cathode surface (reaction 5) and react with TM oxides in the active material, forming slightly more soluble TMF_2 salts. These salts can dissolve in the electrolyte, diffuse to the anode, and degrade the SEI or remain on the cathode, contributing to the CEI formation[53], [59]. Additionally, HF can corrode the copper current collector[60], whereas on an aluminium current collector, it reacts with the native Al_2O_3 layer, forming AlF_3, which provides protection against further Al corrosion[60], [61]. Conversely, in strongly alkaline (pH > 11) aqueous environments (such as water-based NCM, NCA, or LFP slurries), Al_2O_3 dissolves to $Al(OH)_4^-$, leading to aluminium foil degradation and potential loss of electrical contact[61].

By generating H_2O, reactive singlet oxygen ($^1O_2$), and various gaseous byproducts (CO_2, CO, O_2), RLCs contribute to electrolyte degradation, further side reactions, active material breakdown, and CEI formation. These effects lead to increased internal resistance and cell swelling, potentially causing thermal runaway and compromising battery safety. Experimental studies have shown that CO_2 is the primary gas released from the NCM cathode, with CO and O_2 detected in smaller amounts[62]. For further details on gas evolution experiments in liquid- and solid-electrolyte-based batteries, readers may refer to the comprehensive review cited in reference[62].

Degradation during battery operation

The rate and nature of degradation affecting NCM cathodes during lithiation and delithiation is influenced by various factors, including the cycling voltage range, operating temperature, and the relative proportions of TMs in the active material, with nickel content playing a particularly critical role[63]. The most pronounced chemical and structural transformations occur at high levels of delithiation (elevated voltages) and as the nickel concentration in the cathode material increases.

As the voltage rises during charging, different degradation mechanisms become significant depending on the cathode's state of charge (SoC) or degree of delithiation. Here, SoC is defined such that 100 % SoC corresponds to complete lithium extraction from the cathode, while 0 % SoC represents the fully lithiated state ($LiNi_xMn_yCo_zO_2$)[63]. In the range from 0 % to approximately 56 % SoC, NCM materials exhibit structural stability, and charge compensation occurs via reversible redox reactions, resulting in minimal degradation or capacity loss. Beyond 56 % SoC, irreversible charge compensation reactions have been observed for all NCM compositions. However, experimental studies analysing lattice parameter variations, oxygen evolution, and capacity retention indicate that major irreversible degradation effects do not become significant until around 70-80 % SoC[2], [64], [65], [66]. Once the 80 % SoC threshold is exceeded, the degradation process accelerates, manifesting as abrupt lattice parameter changes, oxygen release, and surface reconstruction. These effects contribute to a sharp decline in capacity retention across all NCM compositions, particularly when charging beyond their respective 80 % SoC voltage limits – 4.7 V for NCM111, 4.6-4.7 V for NCM622, and 4.3 V for NCM811[2], [64], [65], [66], [67], [68]. The voltage corresponding to 80 % SoC varies with nickel content, with NCM811 reaching this state at lower voltages when compared to NCM111. Although higher voltages are desirable for increased energy density, 4.7 V exceeds the electrochemical stability window of most conventional liquid electrolytes. Consequently, the progressive shift towards higher nickel content in NCM materials has been motivated, in part, by the ability to achieve the same capacity at lower voltages, thereby mitigating electrolyte degradation[64], [67].

The degradation mechanisms affecting NCM cathodes can be categorized into several key processes[2], [63]:

- lattice expansion and contraction during cycling, leading to volumetric changes and microcracking;
- phase transitions and associated oxygen release;

- TM dissolution, which leads to LAM and LLI;
- the growth of a passivating CEI, which increases impedance while contributing to LLI and LAM.

The degradation induced by repeated battery use has a more detrimental impact on cathode material stability than the effects associated with RLCs. While RLCs contribute to electrolyte and binder decomposition, their influence is most pronounced in the initial few cycles, after which they either disintegrate, become incorporated into the CEI, or undergo side reactions (reactions 1–5)[63]. In contrast, degradation arising from cycling persists throughout battery operation and significantly compromises the structural integrity of the cathode.

All degradation pathways within NCM cathodes are interconnected. For instance, oxygen evolution and surface reconstruction accelerate electrolyte breakdown, which in turn facilitates TM dissolution and promotes CEI growth. These interrelated mechanisms contribute to increased impedance, irreversible capacity loss, safety hazards, and a reduction in overall cycle life[63], [64], [65].

Evolution of lattice parameters and microcrack formation

NCM cathodes are typically composed of secondary particles, which consist of agglomerated, randomly oriented primary layered particles (fig. 1.7a)[69]. Microcracks that develop within the cathode material can be classified as either intragranular or intergranular. Intragranular cracks form within individual grains, often at the interface between the layered phase in the bulk of the primary particles and the spinel or rock salt phases near the surface. These cracks arise due to volume expansion and contraction in the layered phase, while the rigid rock salt surface phases undergo minimal volume change. Whereas intergranular cracks, which form between primary particles, are considered more detrimental to battery performance[69].

During delithiation, the crystal lattice of the NCM primary particles undergoes anisotropic expansion and contraction along the *a* and *c* directions, with the magnitude of these changes being somewhat dependent on nickel content and voltage (fig. 1.7b-d)[70]. In NCM811, a substantial collapse of the *c* lattice parameter occurs at voltages exceeding 4.0 V (fig. 1.7b). At 4.3 V, the *c* parameter becomes smaller than in the fully discharged state and continues to contract if charged further. In comparison, NCM111 exhibits only minimal shrinkage of the *c* parameter within this voltage range (fig. 1.7b)[70].

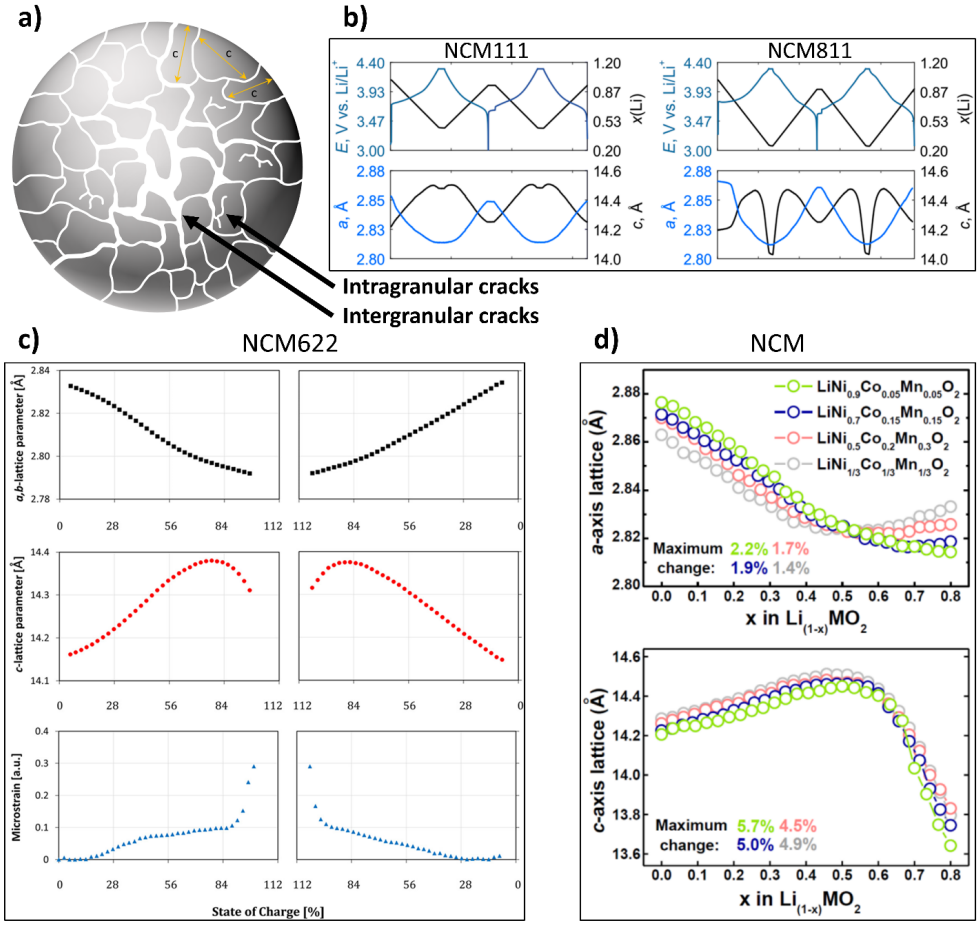

Fig. 1.7. a) Intragranular and intergranular cracks in NCM particle, b) NCM111 and NCM811 voltage, lithiation state, and lattice parameter evolution during charging and discharging[70], c) lattice parameter and microstrain evolution with SoC in NCM622[71], d) lattice parameter evolution with SoC in NCM cathodes with different Ni content[2].

However, when the variation of the *c* lattice parameter is analysed in relation to the SoC rather than voltage, all NCM compositions follow a similar trend (fig. 1.7d)[2]. For example, at 4.3 V, NCM811 has already reached 80 % SoC, whereas NCM111 is delithiated to only 60 % SoC. When charged to 80 % SoC, which corresponds to 4.7 V – significantly beyond the electrochemical stability window of most liquid electrolytes – NCM111 experiences a comparable *c* lattice collapse[2]. This suggests that the perceived structural instability of high-Ni NCMs arises from the lower voltage at which they reach critical SoC levels (80 % SoC at 4.3 V for NCM811 vs. 80 %

SoC at 4.7 V for NCM111). Consequently, comparing different NCM compositions solely within the same voltage range may not provide a fully accurate assessment of their degradation susceptibility, given the substantial differences in their lithiation states.

The abrupt shifts in lattice parameters introduce mechanical stress at the interfaces between randomly oriented primary particles, ultimately leading to their separation and the disintegration of secondary particles. While this results in an increased surface area that temporarily reduces impedance and enhances the rate capability of the cathode, it also accelerates undesirable side reactions with the electrolyte, promotes surface phase transitions, and facilitates CEI formation.

To mitigate intergranular microcracking, researchers have explored the use of single-crystalline NCM, which consists of individual crystallites rather than aggregates of primary particles[72]. Although single-crystalline NCMs exhibit inferior rate capability and reversible capacity compared to their polycrystalline counterparts due to a lower fraction of active surfaces their structural integrity is generally better preserved. This is advantageous because the drawbacks associated with secondary particle cracking, such as rapid capacity degradation and safety concerns, outweigh the temporary performance benefits it provides. As a result, finding solutions to mitigate microcracking in polycrystalline NCMs remains a key focus for the development of safer, cost-effective, and more durable cathode materials with optimized rate capability, reversible capacity, and cycle stability.

Another strategy to address this issue involves minimizing changes in volume or lattice parameters. However, achieving this is challenging and typically relies on the development of materials with either zero volume change (where the overall unit cell volume remains relatively constant despite lattice parameter variations) or zero strain (where lattice parameter changes are extremely limited)[73]. Zero volume change has been reported for NCM layered cathode materials by R. Zhang et al.[74], while zero strain behaviour – often observed alongside zero volume change – has so far been primarily identified in spinel or rock salt materials. These materials are typically engineered through doping, wherein select atoms (often TMs) are substituted with other metallic species to enhance structural stability[73], [74].

Structural degradation and oxygen evolution

During battery operation, the stoichiometric balance of NCM materials becomes disrupted as lithium ions are extracted, leading to instability in the layered structure. Beyond a certain level of delithiation, irreversible charge compensation reactions and structural transformations take place. These irreversible changes are accompanied by a progressive surface phase transition from a layered structure to spinel and subsequently to rock salt, along with oxygen evolution from the cathode material. While oxygen redox in NCM is generally considered reversible[75], significant oxygen release has been detected at high states of charge (above 80 % SoC) using online electrochemical mass spectrometry (OEMS)[64], [76]. Furthermore, operando emission spectroscopy has identified that the evolved oxygen exists in the form of highly reactive singlet oxygen ($^1O_2$)[77], which either undergoes quenching to form triplet oxygen or reacts with the

electrolyte, leading to further gas generation, primarily as CO and CO_2[64], [76], [77]. In addition to accelerating electrolyte oxidation, oxygen evolution also leaves behind an oxygen-depleted host structure, which destabilizes the material and drives the phase transformation from the layered (MO_2) phase to lower-oxygen-content phases such as spinel (M_3O_4) and rock salt (MO). The presence of these oxygen-deficient phases in cycled NCM has been confirmed via high-resolution transmission electron microscopy (HR-TEM)[78].

To better understand the simultaneous surface reconstruction and oxygen evolution in NCM materials, it is necessary to examine the underlying charge compensation mechanisms responsible for $^1O_2$ formation. Although some uncertainty remains regarding the redox activity of TMs in NCMs, nickel is widely recognized as the primary redox-active element. It has also been established that oxygen contributes to charge compensation by participating in electron-sharing interactions with TMs through hybridized TM-O orbitals[63], [65], [79], [80], [81]. A study conducted by Kleiner et al. in 2021[63] utilized near-edge X-ray absorption fine structure spectroscopy (NEXAFS) combined with charge transfer multiplet (CTM) calculations to demonstrate that charge transfer in NCMs primarily involves the oxidation of Ni^{2+} to Ni^{3+}. This oxidation is accompanied by an increase in the covalent character of the Ni-O bond, allowing oxygen to play an indirect role in charge compensation. The study concluded that only Ni and O exhibit redox activity across all NCM compositions, while the oxidation of Ni to Ni^{4+} was ruled out due to discrepancies between NEXAFS results and CTM calculations. Additionally, the involvement of Co in charge compensation was found to be negligible.

Conversely, another investigation into charge compensation mechanisms in NCM811 reported no observable redox activity for Co and Mn up to 75 % SoC but suggested that Ni oxidation continues up to Ni^{4+}, as indicated by hard X-ray absorption spectroscopy (hXAS)[65]. In contrast, several computational and experimental XAS studies on NCM111 have demonstrated Co involvement in charge compensation beyond 66 % SoC[82], [83], [84]. However, yet another study contradicted this, claiming that Co redox processes are absent in NCM111 up to 5 V, with Ni oxidation occurring up to Ni^{3+} at the surface and Ni^{4+} in the bulk[79]. These discrepancies likely stem from challenges in interpreting X-ray absorption spectroscopy data, as edge shifts can result from both oxidation state variations and alterations in the electronic and structural environment of the ligand field[79]. Therefore, further research is required to clarify whether Co contributes to charge compensation and whether Ni truly oxidizes to Ni^{4+} in NCMs. A clearer understanding of these mechanisms is crucial for elucidating oxygen evolution and other structural degradation processes in these materials. Nonetheless, it is widely accepted that oxygen evolution is driven by its redox activity and electron-sharing interactions with TMs via hybridized TM-O orbitals, ultimately enabling electron loss from oxygen. As a result, oxygen evolution is initiated at high SoC levels (around 80 %)[64], [77].

In the 2021 study by Kleiner et al.[63], it was also reported that the Ni–O bond in Ni^{2+} species is predominantly ionic, whereas the Ni–O bond in Ni^{3+} species exhibits strong covalency, facilitating electron sharing between Ni and O. Furthermore, their findings indicated that in

NCM111, 622, and 811 compositions, all Ni^{2+} is converted to Ni^{3+} beyond a capacity of 155 mAh/g (corresponding to 56 % SoC), after which irreversible degradation processes begin. Beyond this threshold, a slight increase in the fraction of Ni^{2+} was observed. Thus, if Ni^{4+} formation does not occur and Co does not partake in charge compensation, then up to 80 % SoC, charge compensation is ensured by electron-sharing interactions between nickel and oxygen without fully oxidizing oxygen, as major oxygen evolution is not detected within this range[64], [77]. However, beyond 80 % SoC, irreversible oxidation of oxygen occurs, leading to the formation and release of $^1O_2$, which subsequently drives phase transitions from layered to spinel and rock salt structures due to the loss of oxygen content[77]:

$$MO_2 \text{ (layered)} \rightarrow M_3O_4 \text{ (spinel)} \rightarrow MO \text{ (rock salt)}$$

Oxygen redox reactions occur both in bulk and on the surface of NCM particles; however, due to kinetic constraints, higher SoC levels are reached more readily at the surface. Consequently, oxygen involvement in charge compensation is more pronounced and irreversible at the cathode surface[85], [86]. This leads to greater oxygen loss from the active material and more extensive phase transformations near the particle surface[64], [87]. During the initial charge-discharge cycles, a growing oxygen-depleted surface layer forms, reducing the amount of oxygen released in subsequent cycles as the diffusion path for oxygen transport lengthens. This phenomenon has been experimentally confirmed by R. Jung et al.[64], who cycled NCM111 and NCM622 up to 4.8 V and NCM811 up to 4.4 V over four cycles, measuring gas evolution via OEMS. Their results showed that gas release was most significant in the first cycle and declined in subsequent cycles, supporting the hypothesis that oxygen diffusion from the bulk is restricted when the particle size is sufficient and operating temperatures are moderate. Other studies[88], [89], [90], [91] further corroborate this by demonstrating that phase transitions to spinel and rock salt phases in NCMs predominantly occur in surface regions. While this self-passivating behaviour is beneficial in limiting further oxygen evolution, the resulting spinel and rock salt surface layers impede lithium diffusion, increasing cell impedance and contributing to LAM.

Although no direct correlation has been observed between Ni content and gas evolution during charging up to 4.3 V, OEMS studies have reported significant O_2 and CO_2 release within the voltage range of 4.3-4.7 V vs. Li/Li^+, with a positive correlation between gas evolution and Ni content[92].

In summary, high SoC delithiation leads to oxygen oxidation and subsequent release, primarily from surface regions, which coincides with the structural transformation from a layered to a spinel and rock salt phase. The reactive $^1O_2$ evolved in this process accelerates electrolyte degradation, TM dissolution, and CEI growth[1]. Additionally, the interface between the bulk layered structure and the surface rock salt/spinel region can accumulate stress due to differences in lattice parameter changes, potentially leading to intragranular cracks that further deteriorate the rate capability and cycling performance of NCM cathodes.

Cation mixing is considerably less pronounced in low-Ni NCMs (e.g., NCM111)[93], [94] compared to high-Ni variants (e.g., NCM811)[95], [96]. This correlation arises due to the lower

Co content in NCM811, which otherwise mitigates cation migration[97], as well as the greater presence of Ni^{2+}, which readily diffuses into the Li layer due to its similar ionic radius to Li^{+}. Additionally, critical SoC is achieved at a lower voltage in high-Ni NCMs (e.g., 80 % SoC occurs at ~4.3 V in NCM811 vs. ~4.6-4.7 V in NCM111 and NCM622)[64], [67].

Transition metal dissolution

All TMs present in NCM cathodes are susceptible to dissolution under elevated voltage and temperature conditions[98]. Among these, Mn dissolution is reported to have the most detrimental impact on LIB performance, particularly due to its adverse effects on the anode side[99], [100]. Mn^{2+} can interact with carboxylate groups formed from electrolyte solvent degradation or react with HF, which arises from the interaction between the electrolyte and residual water. This reaction facilitates the migration of Mn^{2+} toward the anode, where it deposits on the surface[53], [101].

For NCM111, TM dissolution becomes more pronounced at voltages exceeding 4.3 V, as the delithiated state of NCM makes it more vulnerable to corrosion by electrolyte degradation products[102], [103]. Moreover, the dissolution of TMs from NCM is further accelerated by the presence of HF, with Mn^{2+} being the most abundant dissolved species within the electrolyte[99]. The extent of TM dissolution is also influenced by the choice of electrolyte salt, as different salts exhibit varying resistance to ambient moisture, which affects HF formation and, consequently, the extent of corrosion[99]. When HF reacts with Mn, MnF_2 forms which can either migrate toward the anode or remain embedded within the CEI. Typically, the concentration of dissolved metals in aged electrolytes is quantified using inductively coupled plasma optical emission spectroscopy (ICP-OES)[98], [99], [102]. Additionally, TM dissolution from the cathode can be indirectly detected by analysing the anode for trace TM deposits using techniques such as X-ray photoelectron spectroscopy (XPS) and X-ray absorption spectroscopy (XAS)[104], [105], [106], [107], [108].

In the highly lithiated state (low potentials), Mn dissolution follows a disproportionation reaction mechanism[109]:

$2Mn^{3+} \rightarrow Mn^{4+} + Mn^{2+}$

In NCMs, Mn is predominantly found in the Mn^{4+} oxidation state, which is electrochemically stable and largely inert[110]. However, Mn^{3+} can still be present due to lattice defects and oxygen vacancies[111]. Notably, oxygen vacancies appear more frequently in Ni-rich compositions like NCM811 compared to NCM111, particularly at lower potentials, suggesting that Mn dissolution may be more significant in Ni-rich NCM materials.

Once Mn^{2+} ions migrate to the SEI on the anode side, they can become incorporated into the SEI, obstructing lithium-ion transport pathways[112]. Additionally, Mn deposited on graphite anodes undergoes electrochemical reduction, followed by re-oxidation through reactions with the electrolyte solvent[105], [113]. This redox cycling contributes to the continuous loss of active lithium due to reactions with $MnCO_3$ species present in the SEI[113]:

$2Li^{+} + MnCO_3 + 2e^{-} \rightleftarrows Li_2CO_3 + Mn^{0}$

$Mn^0 + EC \rightleftarrows MnCO_3 + C_2H_4$

Growth of the cathode-electrolyte interphase

The formation of the CEI occurs as a result of various RLC reactions (see sub-chapter "Degradation during synthesis and storage"), as well as the direct involvement of RLC species themselves[114], [115]. Additionally, CEI development is influenced by chemical and electrochemical oxidation of the electrolyte, the decomposition of $LiPF_6$ salt, and its subsequent reactions with both the active material and RLC products[116].

The primary constituents of the CEI, illustrated in fig. 1.8, include TM fluorides (TMF_n), which result from TM dissolution and subsequent reaction with HF and the oxidized active material. Other major components are RLC species such as Li_2CO_3, LiO_2, and LiOH, along with various electrolyte decomposition byproducts, including organometallic compounds, polycarbonates, and lithium hexafluorophosphate oxidation derivatives[116]. Due to the numerous sources contributing to CEI formation, many of which are more dependent on the electrolyte composition than the cathode, it is challenging to define a universal mechanism governing its formation. Factors such as the rate of TM dissolution, electrolyte degradation, the concentration of RLC species, their reactivity with surrounding components, and additional side reactions (e.g., oxygen evolution) all play a role in CEI development.

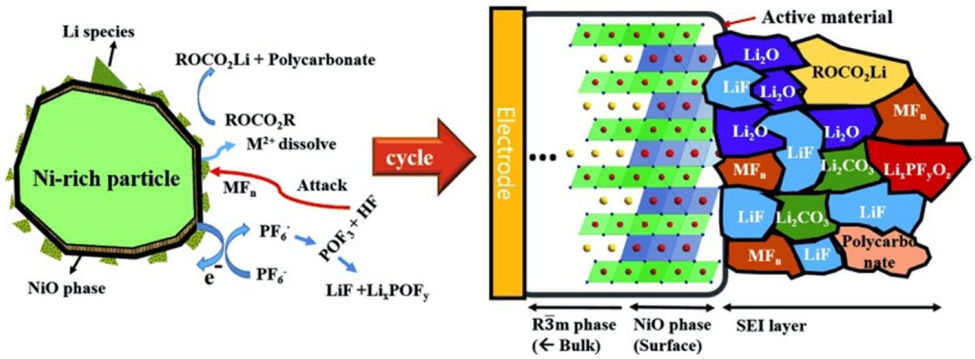

Fig. 1.8. Cathode-electrolyte interphase constituents[114].

Since lithium-containing compounds constitute a significant portion of the CEI, its growth directly contributes to LLI, negatively impacting battery capacity. Additionally, TM dissolution, associated with LAM, further promotes CEI growth as TM-based compounds (such as oxides and fluorides) integrate into the CEI structure[29]. The expansion of the CEI impedes lithium-ion transport, reducing electrode rate capability; however, this process is self-limiting[117]. As the CEI forms a uniform layer around the active material, it behaves similarly to a protective surface coating. Like other passivation layers, it can further restrict electrolyte-driven degradation, thereby mitigating LLI and LAM. Consequently, enhancing cycling stability requires the development of

a robust CEI that minimizes lithium inventory loss. To achieve this, CEI-forming and CEI-stabilizing additives, such as FEC and VC, are frequently introduced into the electrolyte. These additives help regulate CEI formation and prevent excessive re-dissolution, significantly improving capacity retention[118], [119]. However, it is important to note that while a stable CEI can prevent direct reactions with the electrolyte it does not mitigate structural changes or other degradation issues associated with LAM.

Degradation mechanism interplay

Identifying the most critical degradation mechanism in NCM cathodes would require a comprehensive investigation in which individual phenomena, such as cation mixing, oxygen evolution, lattice collapse, microcrack formation, TM dissolution, and CEI formation, are isolated and their respective impacts on capacity, rate capability, and cycling stability are assessed. However, conducting such a study is nearly impossible, as these degradation processes are highly interconnected; the initiation of one mechanism often triggers or accelerates another, leading to a cascade of degradation effects.

The primary instabilities in the NCM cathode, and thus the onset of degradation, stem from disruptions in the $LiNi_xMn_yCo_zO_2$ stoichiometry, which occur when lithium is deintercalated from the cathode and migrates toward the anode during charging. For instance, oxygen evolution begins at approximately 80 % SoC due to excessive charge compensation by lattice oxygen following lithium extraction. This oxygen release depletes the lattice of oxygen, inducing phase transitions on the particle surfaces, which, in turn, exacerbate mechanical stress within the primary particles. The resulting intragranular microcracks hinder lithium-ion diffusion, ultimately reducing capacity, rate capability, and cycling stability. In this degradation sequence, lithium extraction beyond 80 % SoC acts as the initial trigger, yet it cannot be avoided if high capacity is to be achieved. The direct consequence of lithium removal is charge compensation by Ni and oxygen. This effect can be altered through various doping strategies which increase the effective charge of oxygen, helping it remain within the lattice and thereby mitigating oxygen evolution[120], [121]. Thus, in this chain of degradation effects, preserving lattice oxygen is crucial to reducing overall material instability.

Another example of degradation interplay is CEI formation, which arises from RLC species, dissolved TMs, and electrolyte decomposition products. In this scenario, mitigation efforts focus on removing RLC residues from the cathode surface post-synthesis, preventing TM dissolution, and limiting both oxygen evolution and direct electrolyte interaction. These objectives are typically achieved through post-synthesis washing of the cathode, doping strategies, or surface coatings on the active material, as discussed under in later sections.

Ultimately, the most dominant degradation mechanism for a given cathode composition can be determined experimentally using in situ and post-mortem material characterization techniques combined with electrochemical measurements under specific cycling conditions. Alternatively, it can be inferred based on its potential to initiate multiple other degradation processes, which of the degradation mechanisms acts as the critical driver of material degradation.

Degradation in NCMs based on Ni content

In NCM cathodes with varying nickel content, the primary degradation mechanism is largely influenced by the extent of delithiation. As the nickel content increases, the critical SoC of 80 % is reached at lower voltages. Degradation in NCM cathodes is typically assessed based on the commonly applied upper voltage limit of 4.3 V vs. Li/Li+, which is selected considering the electrochemical stability window of both the electrolyte and cathode materials. When an NCM battery is charged up to 4.3 V, the dominant degradation mechanisms transition from being predominantly surface driven in NCM111 to bulk degradation playing a more significant role in NCM811, surpassing surface deterioration, as depicted in fig. 1.9.

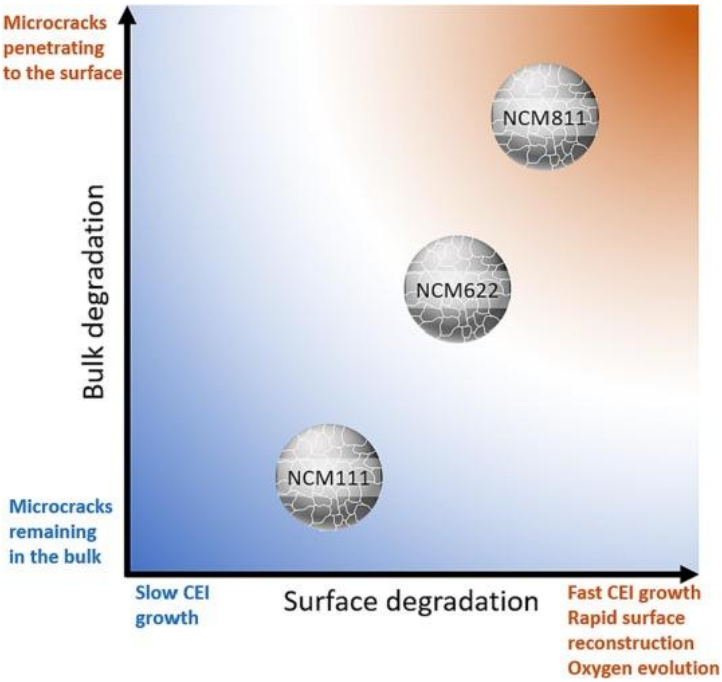

Fig. 1.9. Illustration of the main type of degradation occurring in the NCM111, NCM622, and NCM811 cathodes during battery operation[[11]*.

A comparison of the cycling stability of NCM111 and NCM811 reveals that the overall degradation of NCM811 occurs at a much faster rate than that of NCM111. However, with an increase in nickel content, a higher capacity can be achieved, which justifies the extensive efforts dedicated to enhancing the stability of high-nickel NCMs.

* Author's original publication.

1.4 Cathode degradation mitigation

The following sub-sections are based on the author's publication "A review of the degradation mechanisms of NCM cathodes and corresponding mitigation strategies"[11][*].

Cathode degradation mitigation strategies

Various mitigation strategies have been proposed to address the degradation mechanisms in NCM cathodes. Among the most effective approaches are surface coating of cathode particles, elemental doping, and control over particle microstructure during synthesis. In addition to extending the cycle life of cathode materials, the degree of improvement achieved through these strategies can also provide insights into the dominant degradation mechanisms. For instance, since doping enhances structural stability and suppresses phase transitions, while surface coatings prevent surface degradation and limit reactions with the electrolyte, the extent to which these modifications improve battery performance can indicate the severity of the respective degradation processes.

The primary objective of modifying cathode materials is to enhance their stability during electrode processing and battery cycling, ensuring that high-specific-energy materials such as NCM811, NCM Ni83, and Li-rich NCMs also exhibit satisfactory cycle life and service longevity. This is particularly crucial because many Ni-rich NCM materials inherently suffer from poor cyclability, often falling below 1000 cycles before reaching 80 % of their initial capacity, which hinders their commercialization. The strategies for improving cathode stability address different degradation aspects of the cathode particles, allowing targeted enhancements based on observed failure mechanisms to maximize cycle life. In the scope of this work, we mainly focus on enhancing the cathode stability by creating protective surface coatings on top of NCM active materials.

Surface coating

Surface modification of cathode particles can be achieved either by coating the particles or entire electrodes with a protective layer or by doping the surface region with foreign ions. Several coating techniques have been successfully applied to NCM particles, including atomic layer deposition (ALD)[122], [123], [124], chemical vapor deposition (CVD)[125], [126], magnetron sputtering[127], and wet-chemical synthesis[128], [129], [130], [131], among others. While ALD, sputtering, and CVD have been upscaled to some extent, wet-chemical synthesis remains the simplest and most cost-effective method for large-scale commercial applications. However, coatings produced by ALD and CVD generally exhibit better uniformity, whereas magnetron-sputtered and wet-chemically coated materials often suffer from non-uniform coverage.

The primary objective of surface coating is to create a chemically and thermodynamically stable layer on the cathode particles while minimizing any increase in internal resistance. This protective layer prevents undesirable side reactions with the electrolyte and surrounding

[*] Author's original publication.

environment, thereby inhibiting CEI formation. Additionally, surface coatings help mitigate degradation processes such as oxygen evolution, TM dissolution, and phase transitions, ultimately preserving the integrity of the cathode material.

Various cathode coating materials have been extensively studied, including electronically conductive carbon coatings[132], metal oxides such as Al_2O_3[122], [131], [133], [134], ZnO[135], [136], ZrO_2[131], [134], TiO_2[134], [137], MgO[123], [138], and rare-earth oxides[139], [140]. Additionally, lithium-containing ionically conductive coatings, including Li_3PO_4[128], LiF[141], Li_3VO_4[142], lithium borate glasses (Li_2O-$2B_2O_3$)[143], glassy phosphates[144], and organic polymer coatings[145], [146], have been explored. Many inorganic coatings can be applied in both amorphous and crystalline forms. The main coating applied in this study is Al_2O_3 coating by wet-chemical method.

Wet chemical surface coating

This sub-section is based on the author's publication "Wet-Chemical Synthesis of a Protective Coating on NCM111 Cathode: The Quantified Effects of Washing, Sintering and Coating"[147][*].

Wet chemical coating is a preferred synthesis method due to its relative simplicity and time and cost efficiency, typically involving the dispersion of the active material in a solvent, the addition of a coating precursor, and a final sintering step to achieve the desired product[131], [148], [149].

Interestingly, sintering under conditions like those used for protective coatings has been shown to enhance electrochemical performance by promoting surface reconstruction and removing RLCs[3]. If the active material has been exposed to ambient conditions during delivery or processing, improvements in cycle life resulting from re-sintering and RLC removal might be mistakenly attributed to the protective coating. In fact, many wet chemical coating studies compare only pristine and coated materials, often attributing all observed stability and capacity enhancements solely to the coating itself[131], [149], [150]. The extent to which washing and sintering influence the active material during this type of processing remains uncertain[151], [152].

Establishing a proper reference

There is an abundance of coating studies that explore different wet-chemical coatings on NCM materials, most of which show promising results with improved cycling stability and capacity[131], [153]. However, many of these studies use untreated commercial NCM materials as reference, and attribute all of the capacity and stability improvements to the coating effects[140], [150], [154], [155], when some improvement might be due to the coating procedure itself (washing and sintering the material).

To accurately assess the role of the inert protective coating, this study not only compares the electrochemical performance of coated and uncoated NCM but also systematically examines the individual and combined effects of washing and sintering on capacity retention. In addition to evaluating electrochemical behaviour, surface chemistry analysis and carbon quantification are

[*] Author's original publication.

conducted to identify compositional changes in the active material. This comprehensive approach ensures that improvements in cycle life are properly attributed to washing, sintering, and coating steps, rather than being misinterpreted as solely coating-induced.

Degradation mitigation in NCM cathodes

The following sub-sections are based on the author's publication "A review of the degradation mechanisms of NCM cathodes and corresponding mitigation strategies"[11][*].

An analysis of the available research literature reveals a vast collection of electrochemical data obtained under a wide range of experimental conditions. However, the significant variability in parameters, such as particle size and morphology, electrode composition, electrolyte type, voltage range and corresponding SoC, temperature, and applied specific current, makes direct comparisons between individual studies challenging. This variability complicates the ability to draw definitive conclusions unless a comprehensive, systematically controlled study is conducted.

Despite these limitations, when examined collectively, certain trends emerge that allow for broader analysis without requiring a direct focus on the specific conditions of individual studies. While data remains somewhat scarce, notable tendencies in the effectiveness of doping versus surface coating as a function of Ni content in NCM cathodes can be identified. Fig. 1.10 compiles findings from 45 studies, quantifying the extent to which doping or surface coating has enhanced the cycle life of pristine NCM111, NCM622, and NCM811. Given that many studies limit their cycle life assessments to only 50 or 100 cycles, two graphs illustrate capacity retention at these benchmarks (fig. 1.10). The improvement in capacity retention on the vertical axis is expressed in percentage points (*%CR*), calculated based on the additional capacity retained in the 50th or 100th cycle of the treated material ($CR_{\text{treated NCM}}$) compared to the reference material in each study ($CR_{\text{reference NCM}}$):

$$\%CR = \frac{CR_{\text{treated NCM}} - CR_{\text{reference NCM}}}{CR_{\text{reference NCM}}} \quad (1.2)$$

where $CR_{\text{treated NCM}}$ – improvement in capacity retention of the treated material, %;

$CR_{\text{reference NCM}}$ – improvement in capacity retention of the reference material, %.

[*] Author's original publication.

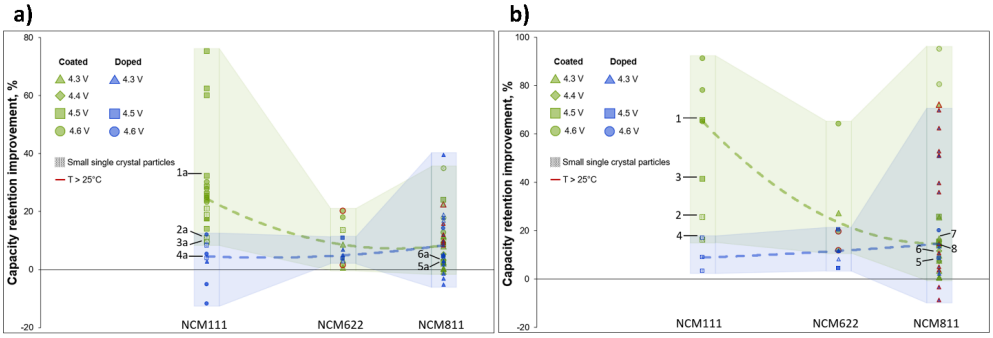

Fig. 1.10. Capacity retention improvement (calculated as shown in equation (1.2)) after a) 50 cycles and b) 100 cycles of coated and doped NCM cathodes compared to the reference untreated samples as reported in 45 literature sources (for reference data, see Appendix)[[11]*.

Since the absolute cycle life of reference (pristine) materials varies significantly, relative improvements are compared instead of absolute values. While the complexity of such a dataset remains, a detailed data table is available in the Appendix for those interested in drawing their own conclusions.

For NCM111, the trends are relatively clear – statistically, surface coating provides a more significant enhancement in cycle life compared to doping. Because the SoC (or degree of delithiation) remains relatively low within the same voltage range, and lattice parameter changes are minimal, NCM111 exhibits little to no microcracking. As a result, doping strategies aimed at mitigating lattice strain are less effective in extending cycle life. Instead, surface protection proves more beneficial in reducing degradation, as degradation in NCM111 occurs more prominently at the surface rather than within the bulk.

In the case of NCM622, the evolution of SoC with voltage closely resembles that of NCM111[64]; however, the critical SoC at which lattice parameter variations become significant is reached at a slightly lower voltage. Consequently, a combination of doping and surface coating is the most effective strategy for improving the cycle life of NCM622.

For NCM811, a higher SoC is reached at lower voltages, leading to more pronounced lattice parameter changes. In this case, doping plays a crucial role in mitigating bulk degradation. However, to achieve optimal cycle life improvements, surface coating should also be implemented to counteract surface degradation and electrolyte decomposition. A detailed discussion of mitigation strategies tailored to each NCM composition is provided in the following sections.

NCM111

The NCM111 cathode material exhibits structural stability at potentials up to 4.3 V vs. Li/Li^+ due to its high Mn content, which stabilizes the structure, and the relatively low SoC reached during

* Author's original publication.

cycling. As a result, it experiences minimal to no microcracking, as previously discussed. Owing to its inherent stability, NCM111 has been commercially utilized without requiring modifications and demonstrates reasonable capacity retention[48]. However, its cycling stability and rate capability could be further optimized by addressing RLCs left on the surface after synthesis, suppressing surface phase transitions, and preventing CEI growth.

Since the primary degradation of NCM111 occurs at the surface, improvements in cycling stability are best achieved through surface coating, which provides surface protection, rather than doping, which primarily stabilizes the bulk lattice. This is supported by the compiled data in fig. 1.10, which shows that across various voltage ranges and particle sizes, both at 50 and 100 cycles, surface coating consistently yields the highest improvement in capacity retention.

Surface coating is widely recognized as the most effective method for enhancing the surface stability of NCM111 cathodes[133], [153], [156], [157], [158], [159]. For instance, Qiu et al.[133] demonstrated that Al_2O_3-coated NCM111 exhibits significantly improved performance when cycled up to 4.5 V. In their study, 5 % Al_2O_3-coated NCM111 achieved a capacity retention of 97.5 % after 100 cycles, compared to only 58.8 % for the uncoated material, corresponding to a capacity retention improvement (*%CR*) of 65.8 % (point 1 in fig. 1.10b) or 32.3 % after 50 cycles (point 1a in fig. 1.10a). Similar enhancements were reported by Chen et al.[156] (*%CR* = 25.6 %, point 2 in fig. 1.10b; *%CR* = 10.8 %, point 2a in fig. 1.10a) and Liu et al.[157] (*%CR* = 41.5 %, point 3 in fig. 1.10b; *%CR* = 9.4 %, point 3a in fig. 1.10a), irrespective of the specific coating material used.

In contrast, doping has shown comparatively lower improvements in cycle life for NCM111. For example, C.X. Ding et al.[160] investigated the effects of Zr doping on NCM111 cycled up to 4.5 V for 100 cycles and reported an increase in capacity retention from 79.2 % for the pristine material to 92.7 % for the Zr-doped sample, corresponding to *%CR* = 17.1 % (point 4 in fig. 1.10b; point 4a in fig. 1.10a for 50 cycles). However, the study did not discuss the possible migration of Zr towards the surface during the high-temperature sintering step (950 °C, 15 h), which could result in the formation of a protective Zr-containing coating[161]. This suggests that at least part of the observed improvement could stem from surface protection effects rather than bulk doping alone.

When the compiled electrochemical data is analysed in terms of capacity retention improvement after 50 cycles, the same trend persists – doped samples consistently exhibit lower improvements than coated ones, further underlining the superiority of surface coating in enhancing the cycle life of NCM111.

Overall, the electrochemical results collected for both 50 and 100 cycles confirm that surface coating is the most effective strategy for mitigating degradation in NCM111 cathodes.

NCM622

NCM622 undergoes more significant lattice parameter changes during cycling compared to NCM111 (fig. 1.7c), which has been shown to contribute to microcracking when cycled up to 4.2 V[162]. Consequently, structural stabilization through doping is more advantageous for

NCM622 than for NCM111[48]. However, when compared to NCM811, NCM622 exhibits less pronounced lattice parameter changes and, therefore, experiences less severe microcracking[163]. Based on these factors, surface protection appears to be the most effective approach for mitigating degradation in NCM622. Nonetheless, incorporating doping could help counteract microcracking and bulk degradation effects in this material.

A review of the research on coated and doped NCM622 reveals a recurring limitation: as with NCM111, many studies do not analyse the migration of coating materials into the bulk or consider the diffusion of doped species toward the surface to form a protective layer. Despite this, electrochemical data indicate that surface coating still provides greater improvements in cycling stability compared to doping. However, the benefits of doping in NCM622 are not negligible – it has been shown to enhance the capacity retention of pristine NCM622 to levels comparable to some of the less effective coated samples.

Thus, the optimal strategy for improving the cycle life of NCM622 appears to be a combination of surface protection and bulk stabilization, with a primary emphasis on surface coating. A potentially promising approach could involve selecting a coating material that diffuses into the particle, thereby simultaneously stabilizing the structure through doping.

NCM811

A viable approach to enhancing the structural stability of NCM811 cathode material is to mitigate the contraction of the *c* lattice parameter, which has been shown to be a significant factor affecting its degradation. Numerous studies have demonstrated that doping can effectively enhance battery lifespan by addressing this issue[120], [164], [165], [166], [167], [168]. However, given that surface degradation is more pronounced in NCM811 compared to NCM622 and NCM111, surface coating should also be considered as a complementary strategy to minimize degradation.

Based on the compiled research data presented in fig. 1.10, both bulk and surface degradation contribute significantly to the overall deterioration of NCM811 cathodes. When examined individually, doping and coating appear to provide comparable improvements in cycle life. Consequently, statistical analysis suggests that an optimal mitigation strategy should integrate both bulk stabilization through doping and surface protection via coating.

A direct comparison of the effects of doping and coating on capacity retention in NCM811 was conducted using the studies by Hu et al.[150] and Jiang et al.[120], corresponding to points 5 and 6 in fig. 1.10b (and points 5a and 6a in fig. 1.10a). In these studies, NCM811 cathode materials were either coated with Al_2O_3 or doped with Ti^{4+} and cycled within a voltage range of 2.8-4.3 V at a specific current of 1 C (200 mA/g) for 200 cycles at room temperature. The capacity retention after 200 cycles was nearly identical for both modifications – 95.4 % for the Al_2O_3-coated cathode and 95.0 % for the Ti-doped cathode. At 100 cycles the capacity retention improvement (*%CR*) was 7.8 % and 10.8 %, respectively, while after 50 cycles the values were 2.1 % and 3.0 %. Assuming no diffusion of the coating material or dopant, both modifications are equally important for mitigating degradation in NCM811.

Similar findings were reported by Huang et al.[169], who demonstrated that MoO_3-coated NCM811 retained 94.8 % capacity after 100 cycles at 1 C to 4.3 V (*%CR* = 14.8 %), and Li et al.[167], who observed that Mg-doped NCM811 achieved 91.9 % capacity retention under the same conditions (*%CR* = 13.6 %), corresponding to points 7 and 8 in fig. 1.10b. Analysing the overall trend in fig. 1.10a-b, the average improvement in capacity retention compared to pristine NCM811 appears to be comparable for both coating and doping strategies. However, it is important to note that in some cases, commercially sourced "pristine" NCM811 materials may already be pre-doped or pre-coated by the manufacturer. If the initial material composition is not thoroughly analysed, this could lead to misleading conclusions regarding the effectiveness of additional modifications.

Doping has been shown to reduce the *c* lattice parameter change in NCM materials. For instance, Al doping decreases the *c* lattice contraction during charging from 3.2 % to 2.7 % but does not completely eliminate the lattice collapse observed at approximately 80 % SoC[170]. To fully address this issue, more advanced doping strategies or microstructural modifications are necessary to eliminate microcracking. A case in point is the material $LiNi_{0.8}Mn_{0.13}Ti_{0.02}Mg_{0.02}Nb_{0.01}Mo_{0.02}O_2$, developed by Zhang et al.[74], which demonstrates how efforts to minimize volume and lattice parameter changes may lead to compositions that deviate from the conventional NCM811 stoichiometry.

From fig. 1.10 it can be inferred that for Ni-rich NCMs the optimal strategy for mitigating degradation is a combination of coating and doping. Furthermore, structural control of the particles could bring additional improvements, however, a more extensive study would need to be conducted.

Degradation mitigation on cell level

In a battery cell, cathode degradation does not occur in isolation but instead influences the entire cell environment, just as changes in the anode or electrolyte can impact cathode stability (as briefly discussed previously). Consequently, reduced cathode degradation is often linked to improvements or modifications made to the anode or electrolyte.

One common approach to enhancing battery stability is the introduction of functional additives into the electrolyte. These additives help stabilize the formation of the CEI or SEI and can also remove reactive species such as HF and H_2O from the electrolyte[171]. For instance, Pham et al.[172] demonstrated that incorporating 1 % VC into a non-flammable $LiPF_6$/PC/FEMC/DFDEC electrolyte effectively stabilizes the CEI on NCM811, while also reducing crack formation, TM dissolution, and structural degradation, even when charging up to 4.5 V. As a result, the cycling stability improved with capacity retention increasing from 76 % to 82 % after 50 cycles. Similarly, Lee et al.[173] reported that adding FEC and 1,1,2,2-tetrafluoroethyl-2,2,3,3-tetrafluoropropyl ether (TTE) to the electrolyte not only stabilizes the CEI but also strengthens the SEI by forming a protective LiF coating. Furthermore, their study revealed that if the SEI on a lithium anode is damaged during cycling TTE can repair it by migrating to exposed lithium surfaces due to its

lithiophilic fluorine sites. As a result, the overall cycling stability of the cell was significantly enhanced.

On the anode side, degradation mitigation strategies primarily focus on suppressing lithium dendrite growth, stabilizing the SEI, and developing structurally stable lithium hosts[174], [175], [176]. SEI stabilization is often achieved through electrolyte additives, and their effects extend beyond the anode alone[174]. In such cases, reducing anode degradation can indirectly benefit the cathode by maintaining lithium inventory (avoiding LLI), ensuring that more lithium remains available for cell operation. While these improvements may not directly prevent cathode degradation, they contribute to overall cell capacity retention and improved cycling stability.

1.5 Summary of NCM cathode degradation and mitigation

The following section is based on the author's publication "A review of the degradation mechanisms of NCM cathodes and corresponding mitigation strategies"[11][*].

NCM materials are derived from layered oxide cathode materials and have progressively evolved toward higher nickel content. This shift has been driven by the need to enhance energy density and address some of the sustainability concerns associated with these materials. However, as the nickel content increases, various stability-related challenges emerge. These include reduced stability in ambient conditions, particle microcracking, undesirable phase transitions, oxygen evolution, CEI growth, TM dissolution, and degradation of the SEI. A comprehensive review of the literature indicates (fig. 1.10) that the dominant aging mechanisms vary depending on the Ni content, implying that the most effective mitigation strategies for NCM degradation should be tailored according to Ni stoichiometry.

An analysis of the effects of coating and doping on NCM degradation mitigation across different Ni compositions reveals distinct trends, summarized in table 1.1. With increasing Ni content and a corresponding reduction in the voltage at which a critical SoC is reached, the importance of stabilizing the crystal lattice and mitigating volume changes through doping becomes more pronounced. In NCM111, where degradation is primarily surface-related, coating proves significantly more effective in enhancing performance compared to doping. In NCM622, the emergence of microcracks as a key degradation factor necessitates doping to stabilize the cathode structure, making it comparatively more effective in degradation mitigation. For NCM811, where structural instabilities become more severe, doping and coating are equally important in ensuring long-term stability. When Ni content exceeds 80 %, both doping (to counteract the more significant lattice parameter changes occurring at lower lithium content) and coating (to prevent rapid surface degradation) should be strongly considered due to the accelerated degradation rate and the increased complexity of degradation pathways[177].

[*] Author's original publication.

Table 1.1

Summary of degradation mechanisms for various NCM materials and corresponding mitigation strategies[11]*

Composition	Degradation	Mitigation
NCM111	Cation mixing, surface reconstruction, oxygen release, RLCs, CEI formation	On average, coating strategy is superior to doping
NCM622	Cation mixing, surface reconstruction, oxygen release, RLCs, CEI formation, microcracking	Coating provides more significant improvement; doping strategies also notably improve performance
NCM811	Cation mixing, surface reconstruction, oxygen release, RLCs, CEI formation, significant microcracking	Coating and doping strategies provide comparable improvement to capacity retention

As the push for higher voltage and higher capacity battery cells continues, the methodologies used to analyse, classify, and address the stability challenges of cathode materials could be applicable to various other cathode chemistries. These include Li-rich NCM, high-voltage spinel, and even cathodes for Li–S batteries. Given the crucial role of layered oxide materials in next-generation battery technologies, particularly in post-lithium systems such as sodium-ion batteries, understanding the degradation mechanisms of layered TM oxides and implementing effective mitigation strategies could have significant implications beyond lithium-ion battery chemistry.

Surface doping is one of the main strategies of NCM cathode degradation mitigation, irrespective of the Ni content, thus, in this work we develop a sustainable, simple wet-chemical coating procedure to coat NCM111 and NCM811 cathode materials with $Al_2O_3/LiAlO_2$ coating. Often wet-chemical coating procedures use toxic and dangerous chemicals such as toluene as solvent and trimethylaluminium as precursor, therefore we aim to replace these harmful components by using ethanol as solvent and aluminium isopropoxide as precursor.

Additionally, a large drawback in many wet-chemical coating studies is the lack of a proper reference, thus, here we highlight the misinterpretations that can arise when evaluating the effectiveness of coatings for cycle life improvement and show the effect that the coating procedure itself (washing and sintering) can have on the stability of the material, even when no coating is synthesized.

2. EXPERIMENTAL

2.1 Materials

Cathode materials NCM111, NCM811

The NCM cathode active materials (CAMs) have a general formula $LiNi_xMn_yCo_zO_2$ ($x + y + z = 1$). The exact compositions used in this work were NCM111 and NCM811, where the numbers denote the stoichiometric ratio of the TMs in the materials (e.g. NCM111 means that the TM ratio is 1:1:1 and the molecular formula is $LiNi_{1/3}Mn_{1/3}Co_{1/3}O_2$). NCM111 and NCM811 was commercially sourced from *MTI Corp.*

Materials for coating syntheses

The aluminum source material for $LiAlO_2/Al_2O_3$ synthesis was aluminum isopropoxide $Al(OC_3H_7)_3$ or AIP. The AIP was obtained from *Sigma Aldrich* (≥ 98 %). The solvent for AIP was absolute ethanol (99.8 %). Purified water for hydrolysis of AIP was obtained from an in-house *Direct-Q R & Direct-Q UV-R* water purification system (ultrapure, type 1 water, > 18 MΩ/Cm).

Materials for cathode preparation

A cathode slurry usually consists of 3 main components: active material, conductive additive, and binder. In this study the active materials used were either NCM111 (coated, uncoated, or reference) or NCM811, conductive additive was carbon black (*Alfa Aesar*, 99.9+ %), and the binder was polyvinylidene fluoride (PVDF, powder, *Sigma Aldrich*, ≥ 99.5 %). The electrode slurry was mixed in N-methyl-2-pyrrolidone (NMP) solvent (*Sigma Aldrich*, anhydrous, 99.5 %). Al foil (*Sigma Aldrich*, 0.015 mm thickness) was used as the current collector.

Materials for battery assembly

For the anode a metallic Li foil (*Alfa Aesar*, 1.5 mm thickness, ≥ 99.9 %) was used, separators were *Whatman* GF/B, and electrolyte used was $LiPF_6$ solution in EC/DEC (1:1 volume ratio) with or without 5% fluoroethylene carbonate (FEC) additive, based on the application – the coin cells with NCM111 contained electrolyte without FEC additive, whereas the coin cells with NCM811 electrodes contained electrolyte with FEC additive. The coin cell casings used were CR2032 stainless steel grade 316L and were obtained from *Xiamen Tob New Energy Technology Co., Ltd.*

2.2 Methods

Coating synthesis

Al_2O_3 coating

The coatings were synthesized on the surface of the CAMs by a wet chemical method. For $LiAlO_2/Al_2O_3$ coating a certain amount of AIP was dissolved in ethanol within 20-30 minutes under

light heating (up to 50°C) after which the heating was removed and NCM powder added to the mixture. The weight of AIP was chosen so that the resulting Al_2O_3 coating would account for roughly 3 wt% of the coated NCM, and the volume of ethanol was chosen accordingly (e.g. to coat 3 g of CAM 0.3716 g of AIP were dissolved in 20 mL of ethanol). After 30 minutes of stirring and dispersing the CAM, a stoichiometric amount of H_2O was added to the mixture in the form of an ethanol-H_2O (95:5 volume ratio) solution. Thereafter, the solution was stirred for 2 more hours to allow coordination of the -OH groups of the formed $Al(OH)_3$ to the oxygen groups on the surface of NCM. The mixture was subsequently centrifugated at 2000 rpm and 6000 rpm for 7 minutes each using a *Hermle Z 306* tabletop centrifuge and washed with ethanol twice before transferring to a crucible to dry overnight at 80°C. The next day the dried powder was sintered at 500°C for 4 h in air using *Nabertherm L 9/13* high temperature furnace, after which it was potted and stored in a glove box in Ar atmosphere with H_2O and O_2 levels <0.5 ppm.

Reference samples

Since coating synthesis involves several steps which could also affect the material properties, a proper reference sample was synthesized by following all the steps of the coating procedure, but without the addition of AIP and H_2O (NCM was stirred for 2.5 h in ethanol, centrifugated and washed twice, dried at 80°C overnight, and sintered at 500°C for 4 hours in air).

Furthermore, two more samples were prepared to assess the effect of washing and sintering separately on the properties of the CAM. The sample assessing washing was prepared by stirring the CAM for 2.5 h in ethanol, centrifugating and washing it twice with ethanol, then drying under vacuum at 80°C overnight. The sample for the assessment of the effects of sintering was prepared by sintering the CAM at 500°C for 4 h in air.

Electrode preparation

Magnetic stirring and ultrasonication

For the coated samples and respective reference samples magnetic stirring and subsequent ultrasonication was used to create electrode slurries. In a 50 mL beaker 5 wt.% PVDF solution in NMP, CAM (coated, uncoated NCM111, or reference samples), and carbon black were weighed in a proportion CAM : carbon : PVDF = 75:15:10. The slurry was mixed by magnetic stirring for 2 h at 400 rpm, then treated in an ultrasound bath (*Elmasonic S 120 (H)*, 37 kHz) for 30 min, and stirred again for 30 min.

Ball milling

For the experiments on LIB ageing determination electrode slurries were prepared by ball milling. The electrode components were weighed into a ball mill stainless steel container in a proportion CAM : carbon : PVDF = 75 : 15 : 10, with PVDF in the form of a 5 % (by weight) solution in NMP. The CAM used in these experiments was NCM811. The slurries were ball milled (*Retsch MM200*) with a frequency of 15 Hz for 60 min.

Electrode coating and drying

The prepared slurries were coated onto an Al foil by a typical tape casting method. Al foil was attached to a glass plate (10 cm x 10 cm), then a pool of electrode slurry was deposited on one end of the glass plate in the middle. Using a *Dr. Blade* coating instrument (± 5 µm) the electrode slurry was evened out (starting at 500 µm down to 100 µm in increments of 100 µm) by dragging the instrument over the pool of slurry and the whole Al-covered glass plate until a broad line of electrode slurry with a wet thickness of 100 µm was obtained. The prepared electrode sheets were then properly marked and put into a vacuum oven (*Shanghai Yuanhuai Industrial Co.,Ltd., DZF-6020*) to dry at 80°C under vacuum overnight.

Electrode punching and weighing

Electrodes with a diameter of 10 mm were punched out from the dried electrode sheets using a manual electrode disc cutter (*TOB New Energy TOB-CP60*). The obtained electrode discs were subsequently weighed on an analytical-grade laboratory scale (*Kern, ABT 120-5DNM, ± 0.001 mg*). To calculate the weight of the active material in one electrode an Al foil disc of the same dimensions was cut out and its weight was subtracted from the weight of the whole electrode. Afterwards, 75 % of the remaining weight was calculated as the CAM mass.

Cell assembly

Coin cells

All electrochemical tests for the coating experiments (with NCM111) and LIB ageing experiments (with NCM811) were carried out in coin cells. The coin cells were assembled in an Ar-filled glove box (*M. Braun Inertgas-Systeme GmbH, EASYlab workstation*) with H_2O and O_2 levels < 0.5 ppm. A spring was inserted into the battery casing, then Li foil was thoroughly scraped to clean off any reacted lithium from both sides. Negative electrode (11.1 mm in diameter) was then punched from the cleaned lithium foil and pressed to a spacer, which was then stacked on top of the spring. Then, a *Whatman* glass fiber separator was punched (15.8 mm in diameter) and positioned on the Li electrode, after which 200 µL of electrolyte was added onto the separator using a micropipette. Once the electrolyte had thoroughly soaked the separator, the prepared cathode was positioned onto the separator using clean Teflon-coated plastic tweezers. The coin cell was closed with a lid and pressed together using a hydraulic coin cell press (*TOB Machine, TOB-MR-120*). All components of the coin cell stack were centered to avoid any short circuits or displacement of lithium foil against the cathode. The assembled coin cells were marked appropriately for further electrochemical testing.

Structural Characterization

X-ray diffraction (XRD)

Powder XRD measurements were carried out using *Rigaku Miniflex 600* (Cu $K\alpha_{1,2}$) for all samples within the coating study to determine the structural parameters of the coated and uncoated active materials. The samples were prepared by compacting the active material powder into a glass

cuvette. The diffraction patterns were recorded in the 2θ range from 10 ° to 90 °, with a scanning rate of 2 °/min, accuracy of ±0.02 °.

X-ray photoelectron spectroscopy (XPS)

X-ray photoelectron spectroscopy (XPS) measurements were carried out to characterize the surface chemistry of coated and uncoated materials, specifically to detect the level of impurities on the surface of NCM and to observe the presence of Al_2O_3 on the surface of the coated material. The XPS measurements were conducted using a *ThermoFisher ESCALAB Xi+* system equipped with a monochromatic Al Kα X-ray source. Calibration of the binding energy scale was done by analyzing sputter-cleaned reference samples of Au, Ag, and Cu, ensuring the Au 4f7/2, Ag 3d5/2, and Cu 2p3/2 peaks aligned at 83.96 eV, 368.21 eV, and 932.62 eV, respectively. The spectra were captured with an X-ray beam size of 650 × 100 µm, using a pass energy of 20 eV and a 0.1 eV step size. A charge neutralizer was applied. During sample preparation the active material powders were compacted into tablets (5 mm in diameter, 1-2 mm thick) and kept in an Ar-filled glovebox prior to the measurement. To prevent surface contamination, the samples were transferred to XPS in an argon-filled transfer vessel assembled in a glove-box, thus avoiding any exposure to air. Before recording spectra, sample surfaces were gently etched in-situ with Ar+ ions.

Scanning electron microscopy (SEM) and energy-dispersive X-ray spectroscopy (EDS)

Surface morphology of the active materials was examined using scanning electron microscopy (SEM) on a *Thermo Fisher Scientific Helios 5 UX* instrument, operated at an accelerating voltage of 10 kV. Elemental distribution was assessed through energy-dispersive X-ray spectroscopy (EDS) on the synthesized powders, with an accelerating voltage of 20 kV applied specifically for the EDS measurements. Post-processing of the SEM images was done using *ImageJ* software. Additionally, primary and secondary particle size distribution was analyzed using *ImageJ* software.

Transmission electron microscopy (TEM)

A transmission electron microscope (TEM, *Fei Tecnai* operating at 200 kV in STEM mode), equipped with an *EDAX* EDS detector, was utilized to verify the presence of an Al-containing coating and to estimate its thickness. For STEM analysis, a lamella was prepared from the coated NCM111 powder by positioning a particle on a silicon wafer. To protect the surface, a thick layer of platinum was deposited on top using focused ion beam (FIB). The lamella was further prepared using a standard method, where an ion beam with a 30 kV acceleration voltage thinned the sample to approximately 100 nm, followed by final polishing with 5 kV ions to minimize the thickness of amorphized surface layers. EDS measurements were carried out on the surface of the secondary particle to ascertain the presence of Al. In addition, a line EDS analysis was carried out to approximately establish the thickness of the Al-containing coating.

Inductively coupled plasma mass spectrometry (ICP-MS)

An *Agilent Technologies 8900 ICP-QQQ* mass spectrometer was employed to measure aluminum content in the coated sample. Impurity levels were quantified using a five-point calibration graph method by diluting a certified multi-element standard solution.

Isotope ratio mass spectrometry (IRMS)

To analyze carbon traces, predominantly present as surface impurities, isotope ratio mass spectrometry (IRMS, *Nu Horizon*) was utilized in conjunction with an Elemental Analyzer (*EuroVector Euro EA3000*). For carbon quantification, a five-point calibration curve was established using a laboratory reference material containing 2 % C in MnO_2.

Electrochemical characterization

All rate capability and cyclability measurements were carried out in half cells (containing metallic lithium anode) using a *Neware BTS-4000* series battery tester at a controlled 25.0 ± 0.1 °C temperature (*Neware MHW-25-S* constant temperature chamber).

Rate capability and cyclability for SoH estimation studies

For electrochemically testing the NCM811 active material during the SoH estimation studies, 17 cells were cycled in 2 different modes (2 series of cells) to observe if the cycling mode will influence the evolution of voltage hysteresis in relation to SoH.

1. The following steps were repeated on loop until SoH dropped to at least 80 %:
    - rate capability – 5 charge-discharge cycles at specific currents ranging from 0.1 C up to 10 C (0.1 C, 0.2 C, 0.5 C, 1 C, 2 C, 5 C, 10 C);
    - cycling – 100 charge-discharge cycles at a specific current of 1 C.
2. The following steps were carried out:
    - initial rate capability – 5 charge-discharge cycles at specific currents ranging from 0.1 C up to 10 C (0.1 C, 0.2 C, 0.5 C, 1 C, 2 C, 5 C, 10 C);
    - cycling – charge-discharge cycling at a specific current of 1 C until SoH drops to at least 80%;
    - final rate capability – 5 charge-discharge cycles at specific currents ranging from 0.1 C up to 10 C (0.1 C, 0.2 C, 0.5 C, 1 C, 2 C, 5 C, 10 C).

1 C (200 mA/g for NCM811) corresponds to the specific current required to charge or discharge the battery cell in one hour. The value depends on the theoretical specific capacity (200 mAh/g).

The cells were cycled using constant current, constant voltage (CCCV) charging and constant current (CC) discharging mode in the range from 2.7 V to 4.3 V vs. Li/Li^+. The cut-off current for the constant voltage step was 10 % of the CC charging current.

Rate capability and cyclability for coating studies

For the coating studies on NCM111 active material rate capability testing was carried out in separate cells from cycling stability measurements.

- Rate capability – 5 charge-discharge cycles at specific currents ranging from 0.1 C up to 20 C (0.1 C, 0.2 C, 0.5 C, 1 C, 2 C, 5 C, 10 C, 20 C).
- Cycling stability – 500 charge-discharge cycles at a specific current of 1 C.

1 C for NCM111 corresponds to 170 mA/g. The cells were cycled using CC charging and discharging in the voltage range 2.7 - 4.3 V vs. Li/Li^+.

For the coating studies on NCM811 material, the testing was done differently from coating studies on NCM111.

- Cycling stability – 3 formation cycles at a specific current of 0.1 C followed by 500 charge-discharge cycles at a specific current of 1 C.

The cells were cycled using CCCV charging and CC discharging modes in the range from 2.5 V to 4.3 V vs. Li/Li^+. The cut-off current for the constant voltage step was 10 % of the CC charging current.

Data processing

Charge-discharge measurements

During the charging and discharging of the cells, the battery tester records the set current, time and voltage at certain time increments. The current and time are then used to calculate the capacity of the cell during charging and discharging by the formula:

$$Q_0 = I * t \tag{2.1}$$

where I – current, mA;

t – time, h

Since the mass of the electrode is known, the mass of the active material can be calculated by the following equation:

$$m_{\mathrm{AM}} = (m_{\mathrm{el}} - m_{\mathrm{cc}}) * r \tag{2.2}$$

where m_{el} – mass of the whole electrode, g;

m_{cc} – mass of the current collector, g;

r – ratio of the active material in the electrode, between 0 and 1, dimensionless.

In the scope of this work r from equation (2.2) corresponds to 0.75 (other parts are composed of binder and conductive additive).

Using Q_0 and m_{AM} we can calculate the specific capacity or gravimetric capacity which is the capacity normalized by the active material mass:

$$Q = \frac{Q_0}{m_{\mathrm{AM}}} \tag{2.3}$$

The specific capacity was the main parameter used to characterize and compare the different cathode materials. The specific capacity and voltage are also used to construct the charge-discharge curves from battery cycling. An example of a typical charge-discharge curve can be seen in fig. 1.3.

The plateau-like (least slope) region of the charge-discharge curve signifies the operating voltage of the cell.

Another important measure of the performance of the battery cell is the Coulombic efficiency:

$$CE = \frac{Q_{\text{disch}}}{Q_{\text{ch}}} * 100\% \quad (2.4)$$

where Q_{disch} – discharge capacity, Ah;

Q_{ch} – charge capacity, Ah.

The Coulombic describes the loss of charge in each charge-discharge cycle, directly related to the loss of lithium.

State of health (SoH) and state of charge (SoC)

The state of health (SoH) is calculated at any point during the cell's lifetime using the following formula:

$$SoH = \frac{Q_{\text{n}}}{Q_{\text{i}}} \quad (2.5)$$

where Q_{n} – capacity at any given cycle, Ah;

Q_{i} – initial capacity, Ah.

Where Q_n is the specific capacity (or capacity) at any given charge-discharge cycle and Q_I is the initial specific capacity (or capacity) of the cell after the formation cycles. Usually the end of a cell's lifetime is considered when SoH has reached 80 %.

The state of charge (SoC) is calculated from the specific capacity (or capacity) in each cycle from the charge-discharge curve, with 0 % SoC corresponding to a completely discharged cell (fully lithiated cathode) and 100 % SoC corresponding to a completely charged cell (delithiated cathode).

$$SoC = \frac{Q_x}{Q_n} \quad (2.6)$$

where Q_x – capacity (or specific capacity) at any given point during charging or discharging the cell, Ah;

Q_n – full capacity (or specific capacity) of the cycle from which Q_x is obtained, Ah.

Determination of voltage hysteresis at certain SoC is described in more detail in the result section regarding SoH estimation studies.

3. RESULTS AND DISCUSSION

3.1 State of Health estimation from voltage hysteresis

This chapter is based on the author's publication "State of health as a function of voltage hysteresis in Li-ion battery half-cells"[178][*]

A part of this work is focused on the degradation of LIBs and the need for a simpler, quicker way to determine the SoH of any given battery cell. Our method for determining the SoH of a battery cell relies on the growth of internal resistance of the battery as it ages. The growth of internal resistances manifests as an increase in overpotentials during charging and discharging, and thus - an increase in voltage hysteresis.

Since LIB materials vary (as discussed in the theoretical background), the primary aging mechanisms and degradation modes can differ depending on factors such as the chemistry and structure of the active materials, their stability at different potentials, and their interactions with various electrolytes. However, a common trend across all materials is the progressive increase in voltage hysteresis during ageing. Although the rate of this increase varies among different materials, it may still correspond to similar SoH values. Therefore, evaluating multiple material combinations is essential to determine whether a universal SoH model can be developed.

In this study, we specifically investigate the relationship between SoH and voltage hysteresis in an NCM811-Li cell, analysing its behaviour down to 53 % SoH.

Voltage hysteresis determination and significance

Voltage hysteresis is the sum of overpotentials when charging and discharging a battery cell. As the battery ages during charge-discharge cycling, its internal resistances increase, which is indirectly depicted in the rise of voltage hysteresis. Additionally, voltage hysteresis increases with specific current, as stated by the Butler-Volmer equation (equation (1.1)), hence, the SoH evolution with ageing is different at each specific current. Here, we characterize the SoH dependency on voltage hysteresis at specific currents up to 5 C.

The employed measurement and data acquisition procedure (also described in the Experimental section) is depicted in fig. 3.1. Charge-discharge cycling at 1 C rate was combined with rate capability measurements every 100 cycles (fig. 3.1a). SoH was calculated based on the 1 C curve as most of the cycling was done at 1 C, thus ageing the cell at a rate corresponding to this charging rate. The 80 % SoH value corresponding to the EoL was reached already after 100 cycles, however, for more elaborate analysis the cells were cycled further until about 53 % SoH.

The voltage hysteresis value at 50 % SoC at each C rate was obtained as shown in fig. 3.1b. 50 % SoC was calculated based on the obtained capacity in each cycle. Fig. 3.1c shows the trend of the voltage hysteresis evolution over various C rates and SoHs, and clearly depicts the growth

[*] Author's original publication

of voltage hysteresis with increasing C rate in a manner similar to Butler-Volmer curve. These curves at certain SoHs are the main sources of information used for further analysis of the relationship between SoH and voltage hysteresis and developing ways to determine SoH based on the value of the voltage hysteresis.

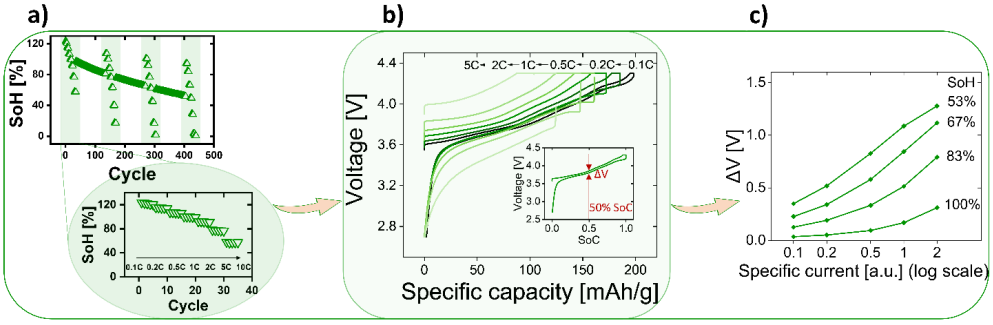

Fig. 3.1. Illustration of voltage hysteresis determination from charge-discharge curves (a-b) and voltage hysteresis growth with increasing applied specific current and decreasing SoH (c)[178]*.

SoH determination from voltage hysteresis

The positive correlation between voltage hysteresis and battery ageing is consistent among all 17 cells measured (fig. 3.2a), independently of the measuring regime used (see the 2 regimes described in the Experimental section), indicating that conducting rate capability measurements in between cycling does not influence the ageing behavior – ageing during rate capability measurements continues at a rate comparable to the ageing at 1 C rate. From the voltage hysteresis growth tendency in fig. 3.2a we can observe that at the same SoH the voltage hysteresis is larger for cells cycled at higher rates than those cycled at lower rates. This growth in hysteresis has a purely kinetic origin from the higher charge-discharge rate and not because the battery ageing is more advanced. As the rate capability measurements (from which the voltage hysteresis vs. SoH data was obtained) are carried out only every 100 cycles, there is a lack of data points between 100 % and 80 % SoH which was already reached after 100 cycles. However, the remaining measurements beyond 80 % SoH allow us to find functions that best describe this relationship (fig. 3.2 and table 3.1).

* Author's original publication.

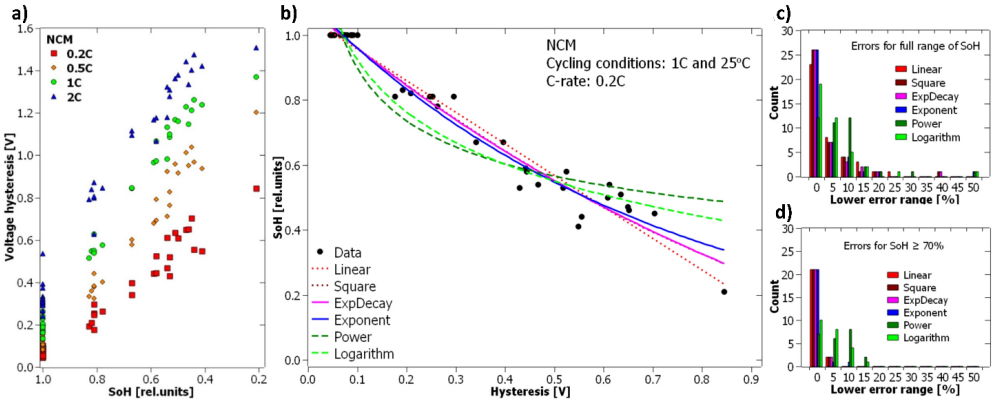

Fig. 3.2. Voltage hysteresis increase with SoH at different C rates (a), SoH as a function of voltage hysteresis at 0.2 C rate fitted by various basic functions (b), error distribution of the different fit functions for the whole SoH range (c) and for SoH ≥ 70 % (d)[178]*.

The increase in voltage hysteresis with diminishing SoH in fig. 3.2a can be flipped to allow reading the SoH from voltage hysteresis (fig. 3.2b, data obtained from 0.2 C rate measurements). This relationship (SoH = f(ΔV)) is what could enable us to create a way to determine the SoH of NCM-Li cells at any given point in battery life with a certain error, if a function describing this relationship can be determined. Here (fig. 3.2b), the data is fit by several basic functions for which the parameter errors and coefficients of determination R^2 are calculated (table 3.1) to evaluate the best fit. Already visually inspecting the fits some functions are more deviated from the data points than others, namely logarithm and power functions, substantiated by R^2 values of 0.992 and 0.988, respectively. Hence, these functions are discarded as possible fits.

Linear, exponential, square, and exponential decay approximations provide the best fit for the full range of SoH, achieving R^2 values above 0.996 and maintaining the highest error count below 5 % (fig. 3.2c). However, the parameter errors for the square and exponential decay functions are too large (up to 102 %, table 3.1), making them unsuitable for SoH determination. When evaluating the remaining linear and exponential functions at SoH levels above 70 %, only the exponential function exhibits errors exceeding 5 %, with a single instance reaching 10 % (fig. 3.2d). Consequently, linear and, to some extent, exponential functions serve as the most precise approximations for SoH determination from voltage hysteresis. The linear function fits well above 70 % SoH, whereas the exponential function more accurately represents the accelerated battery ageing below this threshold. Additionally, if the ΔV value is derived from a single charge–discharge measurement of an NCM811 half-cell and compared with the linear function down to 70 % SoH, SoH determination from this ΔV value could achieve 5 % accuracy.

* Author's original publication.

Table 3.1.

Basic approximation function coefficients with relative errors indicated in the parentheses, and coefficients of determination R^2 for half-cells containing NCM811 electrodes[178][*].

Function	Coefficient			R^2
	a0	a1	a2	
ExpDecay a0+a1*exp(-x/a2)	-0.459 +/- 0.469 (102 %)	1.544 +/- 0.458 (30 %)	1.182 +/- 0.345 (29 %)	0.997230
Square a0+a1*x+a2*x^2	1.081 +/- 0.0158 (1 %)	-1.240 +/- 0.115 (9 %)	0.372 +/- 0.154 (41 %)	0.997202
Exponent y=a0*exp(a1*x)	1.104 +/- 0.014 (1 %)	-1.403 +/- 0.050 (4 %)	-	0.997052
Linear a0+a1*x	1.054 +/- 0.012 (1 %)	-0.973 +/- 0.031 (3 %)	-	0.996761
Logarithm y=a0+ a1*ln(x)	0.389 +/- 0.022 (6 %)	-0.232 +/- 0.012 (5 %)	-	0.992461
Power y=a0*x^a1	0.464 +/- 0.021 (5 %)	-0.287 +/- 0.020 (7 %)	-	0.988315

In a battery cell with 2 electrodes, the BV equation (equation (1.1)) can be used to describe each electrode operation individually. Although lithium as a counter electrode has often been regarded as the perfect anode and used in half cells to study other LIB electrodes without considering the contributions from the Li metal electrode, it has been shown that it does contribute to the overpotential rise in full cells[179]. Nevertheless, by only considering the cathode contribution to the total overpotential in a battery cell and by assuming the anodic charge transfer coefficient α_a to be 0 during the charge and the cathodic charge transfer coefficient α_c to be 0 during the discharge of the cell (neglecting the counterpart of the net reaction at the cathode), we have been able to fit the correlation between the specific current and voltage hysteresis with a BV-like

[*] Author's original publication.

equation (equation (3.1)) at different states of health (SoH), discussed further in our publication[178]*.

$$y = a(e^{bx} - 1) \tag{3.1}$$

where a, b – fitted parameters, dimensionless

x – voltage hysteresis, V.

While introducing these simplifications holds no electrochemical meaning, it does provide a good approximation of the three-way relationship between voltage hysteresis, specific current and SoH and an additional method of determining the SoH of a cell based on the observed voltage hysteresis at different specific currents (fig. 3.3). Additionally, we were able to use the same equation to fit the specific current vs. voltage hysteresis at different SoHs for LFP half cells[178]*, thus suggesting that it can be used for multiple cathode chemistries.

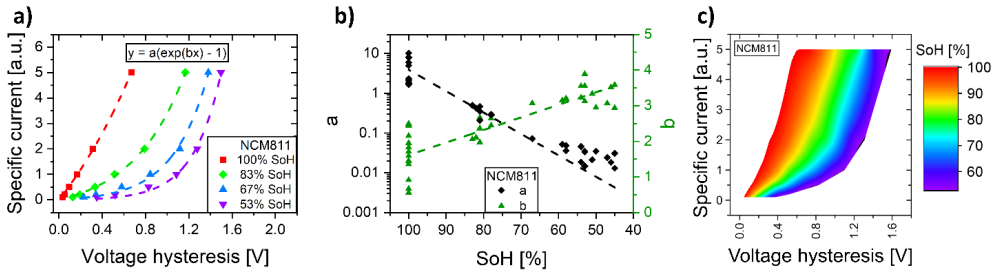

Fig. 3.3. Specific current as a function of voltage hysteresis approximated by a BV-derived equation (a), the respective a and b equation parameter dependency on the SoH of the NCM811 half cell (b). A visualization of SoH determination from the voltage hysteresis measurements at different specific currents (c), data obtained from 7 cells[178]*.

Although the simplified BV-derived fit in fig. 3.3a does not describe the electrochemistry of the cell, it very closely approximates ($R^2 \geq 0.99$) the relationship between specific current (or C rate) and voltage hysteresis, which does stem from the principles of the BV equation. While hysteresis at near-zero current is not always zero[180], [181], and charge–discharge reactions can display asymmetry[182] with lithiation and delithiation processes being inhomogeneous across the electrode[183], our method offers an initial, yet valuable insight.

The selected approximation function aligns well with the obtained data points and passes through the origin (0,0), satisfying the theoretical requirements of the BV function (fig. 3.3a). The fit parameters, a and b, of the BV-derived function (equation (3.1)) were estimated using simple exponential and linear functions, respectively (fig. 3.3b). Despite some dispersion, these parameters exhibit consistent trends as SoH declines – parameter a decreases exponentially, while

* Author's original publication.

b increases linearly. To ensure more comparable fit parameters, certain data points approaching the maximum possible voltage hysteresis based on the measurement voltage range (1.6 V) were excluded from the fit.

The fitted data from multiple half-cells, as shown in fig. 3.3a, can be combined to demonstrate how voltage hysteresis evolves with increasing C-rate and decreasing SoH (fig. 3.3c). In this representation, data from seven NCM811-containing half-cells were merged into a 3D plot, illustrating the general SoH regions associated with varying specific currents and corresponding voltage hysteresis. This visualization could serve as a reference for SoH estimation using a single rate capability measurement ranging from 0.1 to 5 C. By approximating the obtained C rate and voltage hysteresis data with a BV-like function, it can then be compared against the SoH visualization graph (fig. 3.3c). The described approach, however, requires somewhat advanced data analysis, thus, the direct SoH vs. voltage hysteresis comparison at a certain C rate (fig. 3.2) gives a quicker, easier and more direct way of estimating the SoH.

Summary: SoH determination limitations and outlook

Following the need for easier and more direct ways to determine the SoH of a given battery, we have demonstrated how the SoH can be estimated either from the voltage hystereses of one rate capability measurement and fitting a BV-derived equation (equation (3.1)) to the data or from the voltage hysteresis measurement of one charge-discharge cycle and reading the SoH value from a fitted graph. Admittedly, the proposed method is based on very specific parameters (cathode, anode chemistry, measurement setup), however, it could serve as a guide or a building block for a detection system which is able to determine the SoH of a given battery based on one charge-discharge measurement with a certain error, thus, allowing the batteries from scrap yards and recycling stations to be utilized further in second life applications, avoiding premature recycling.

The relationship between SoH and voltage hysteresis for NCM811 half cells at 0.2 C can best be fit by a linear approximation for SoH values above 70 %, however, below 70 %, the relationship is more accurately described by an exponential function. Combining these two fits at the appropriate SoH ranges, we have described the SoH and voltage hysteresis relationship down to around 20 % SoH. Below 20 % SoH one could argue that recycling the materials is justified.

We have also shown that the relationship between the C rate and voltage hysteresis can be rather accurately fit by a simplified BV-derived equation (equation (3.1)). This opens the possibility of exploring the SoH and voltage hysteresis relationship at different C rates, thus, providing another way to estimate the SoH of an unknown battery, using the voltage hysteresis measurements at different C rates, rather than one definite C rate (which is usually not known for batteries of unknown loading). Hence, if the voltage hysteresis data at different C rates is fit by the BV-derived function, it can be compared against the constructed graph and the SoH value can be found.

As mentioned before, the main limitations of the proposed methods include the demonstrated fits only being applicable to the chosen set of parameters (cathode, anode, electrolyte chemistry,

other measurement parameters, which influence voltage hysteresis, such as temperature). This means that a common method or device for SoH estimation of any unknown battery would require this kind of fitting to be done for each separate set of parameters. However, these findings present an intriguing avenue for future research.

Additionally, while we conduct full range charge–discharge cycling, it is important to note that a complete cycle may not always accurately reflect real-life applications or even be necessary. Instead, SoH estimation could rely on data from battery operation or targeted charging and discharging experiments within a narrower SoC range (e.g., 40-60 % SoC). As expected, our results exhibit significant dispersion for half-cells assembled in laboratory coin-cell cases[184]. However, the ability to determine SoH with approximately 5 % accuracy, even in lab-built cells, suggests that mass-produced battery cells could demonstrate an even stronger correlation between voltage hysteresis and SoH.

Finally, it is important to highlight that this study focuses solely on half-cells with NCM811 cathodes, where LAM is the primary aging mechanism. However, the degradation process in full LIB cells is more complex.

3.2 NCM ageing mitigation by wet-chemical coating synthesis

The following chapter is based on the author's publication "Wet-Chemical Synthesis of a Protective Coating on NCM111 Cathode: The Quantified Effects of Washing, Sintering and Coating"[147][*].

While aging in LIBs consists of multiple phenomena, often a key player in performance degradation is the cathode. Additionally, many of the cathode aging processes promote anode and electrolyte degradation, and vice versa. Thus, protecting the cathode from degradation will enhance the overall stability of the battery cell.

Based on the meta-analysis drawn from several coating studies on NCM materials with different Ni content (see Theoretical background), forming a protective coating on the active material to mitigate reactions with the electrolyte, transition metal dissolution, and oxygen evolution is a necessary step for improving the capacity retention of any Ni content NCM. However, for higher Ni content NCMs doping becomes an equally important if not more important strategy to prevent ageing of the material due to extensive microcracking that occurs as the material is delithiated beyond 80%, which occurs at lower voltages for the higher Ni content NCMs (4.3 V vs. Li/Li^+) than for lower Ni content NCMs (4.6 V vs. Li/Li^+).

Although doping strategies are important in degradation mitigation, in this work we focus on forming a protective coating on NCM material with 33 % and 80 % Ni content – NCM111 and NCM811, respectively. More specifically, we develop a wet-chemical Al_2O_3 coating synthesis on the surface of NCM materials. The coating synthesis is based on hydrogen bond formation between

[*] Author's original publication

the hydrolyzed aluminum precursor and oxygen groups on the NCM particle surface (fig. 3.4). After the initial $Al(OH)_3$ layer is formed, the material is sintered in air at 500 °C to form the final Al_2O_3 coating.

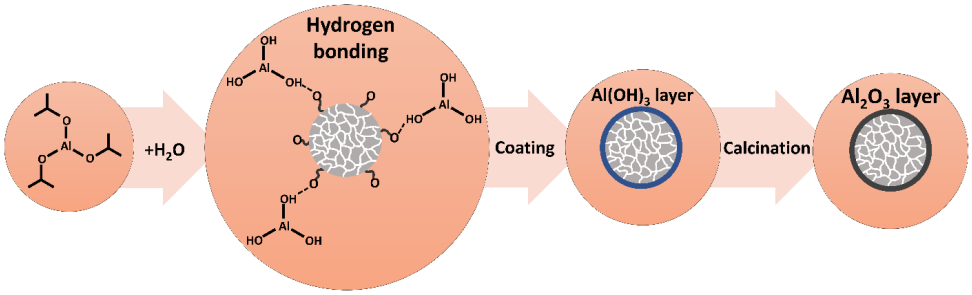

Fig. 3.4. Wet chemical Al_2O_3 coating process.

Wet-chemical coating on NCM111 material

Washing and sintering are essential steps in all wet-chemical coating synthesis processes for electrode materials. Typically, the coating precursor is mixed with the electrode active material in a suspension, followed by drying and sintering. The coated material is then compared to the uncoated material, with any improvements in electrochemical performance often attributed solely to the coating. However, while proper coating of cathode active materials can enhance electrochemical performance, significant improvements may also result from washing and sintering alone, as highlighted in the introduction. This is particularly true if the source material was improperly stored, leading to surface contamination, cation mixing, and a surface layered-to-spinel phase transition. To isolate the specific effects of the coating itself, this study eliminates the influence of washing and sintering by comparing the electrochemical performance of the coated material with that of a reference sample that has undergone the washing and sintering steps of the coating procedure.

Since washing, sintering, and coating alter the surface of the active material, the electrode preparation method must be carefully adjusted not to damage the surface coating or break apart the particles. Intensive mixing methods, such as wet ball milling or high shear processing, can fracture secondary active material particles, thereby revealing uncoated surfaces from within the particle bulk. This can obscure the stability improvements provided by surface coatings, as the newly exposed, uncoated surfaces may degrade. Additionally, while these methods enhance electrode homogeneity, ball milling has been shown to compromise particle integrity, negatively affecting electrochemical performance[185]. To preserve particle structure while ensuring electrode uniformity, we chose a gentler approach, using magnetic stirring followed by sonication at a frequency low enough (37 kHz) to preserve the secondary particles. This method allows for a direct comparison between pristine, coated, and reference materials – something that may not be feasible with more aggressive, energy-intensive mixing techniques.

Material characterization

Analyzing the XRD results (fig. 3.5) for pristine, reference, and coated NCM111, no new phases are detected in the modified samples, suggesting that the coating is either thin or amorphous. Similarly, no structural changes are observed in the samples that underwent only sintering or only washing. The *a* lattice parameter remains stable at approximately 2.8618 Å across all modifications, while the *c* lattice parameter (14.2373 Å) exhibits a minimal increase of less than 0.001 Å in reference and coated materials. These lattice parameters align well with previously reported values[70], [186].

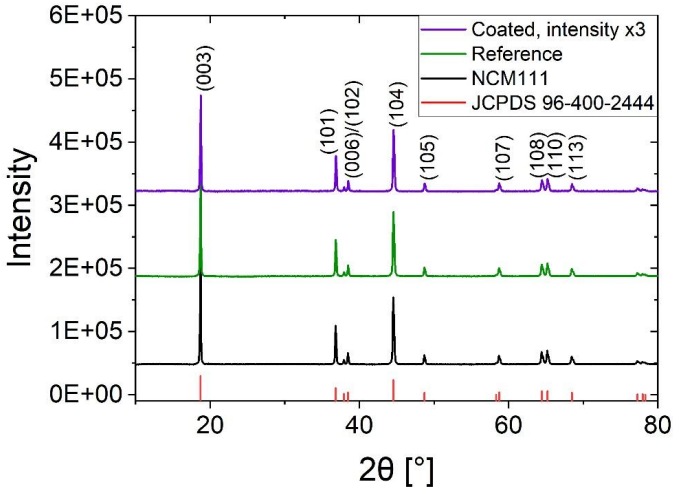

Fig. 3.5. XRD analysis of pristine, reference, and coated NCM111 material[147]*.

Rietveld refinement results and statistical errors are provided in fig. 3.6 and tables 3.2, 3.3. The slight increase in the *c/a* ratio (table 3.2) has been associated with an enhanced layered structure, which in turn improves Li^+ diffusivity in NCM cathode materials[187]. Furthermore, since Al^{3+} ions have a smaller radius than Ni^{2+} and Li^+ ions, any substitution or doping would result in a reduction of lattice parameters. The absence of such a decrease suggests that Al^{3+} doping does not occur in the bulk of the coated samples or is so minimal and surface-concentrated that it remains undetectable by XRD. This conclusion is further supported by several coating studies indicating that even at temperatures up to 800°C, significant Al^{3+} diffusion into the particle does not occur due to the prominent presence of Mn in the lattice[149], [188], [189], [190], which promotes Al segregation and exclusion from the NCM lattice. However, with decreasing Mn concentrations (NCM622 → NCM811) Al diffusion into the bulk at high annealing temperatures (800 °C) becomes more pronounced[188].

* Author's original publication.

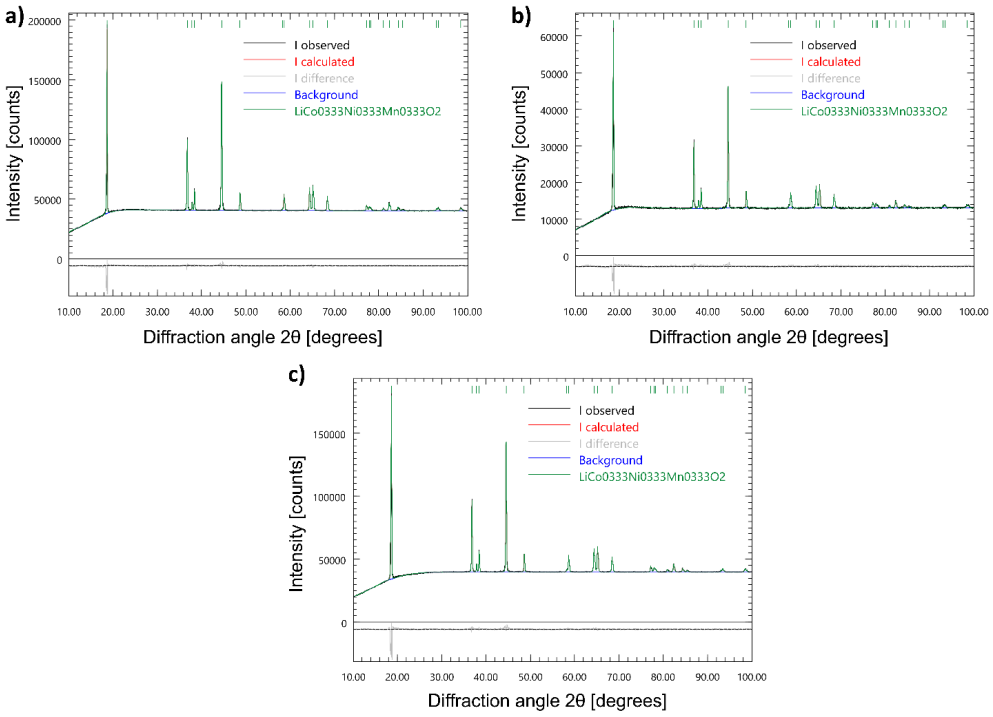

Fig. 3.6. Rietveld refinement graphs for pristine (a), reference (b), and coated (c) NCM111[147]*.

Table 3.2

Lattice parameters of pristine, reference and coated NCM111 material obtained from Rietveld refinement of XRD patterns[147]*.

Sample	**Pristine NCM111**	**Reference**	**Coated**
***a*, Å**	2.86188 ± 2.6E-05	2.86173 ± 2.50E-05	2.86149 ± 3.60E-05
***c*, Å**	14.23729 ± 2.40E-04	14.23893 ± 2.20E-04	14.23877 ± 3.50E-04
***c/a* ratio**	4.9748	4.9756	4.9760
Ni in Li sites, %	2.04 ± 0.21	2.23 ± 0.19	2.19 ± 0.31

* Author's original publication

Table 3.3

Rietveld refinement fit parameters of pristine, reference and coated NCM111 material[147][*].

Sample	Pristine NCM111	Reference	Coated
Rwp, %	0.71	0.64	1.04
Rexp, %	0.51	0.52	0.89
χ^2	1.94	1.51	1.37
GoF	1.39	1.23	1.17

XRD (003)/(104) peak intensity ratios are commonly used as a quick reference to assess the degree of cation mixing in cathode materials, with values exceeding 1.2 generally indicating minimal or no cation mixing. For the pristine, reference, and coated NCM111 samples, these ratios are 1.50, 1.47, and 1.55, respectively, suggesting that cation mixing is not a significant concern in this material. Complementing this, Rietveld refinement results (table 3.2) show cation mixing levels around 2% across all samples, with all values matching within the margin of error. The relatively low degree of cation disorder can be attributed to the presence of cobalt in the NCM composition, which is known to stabilize the lattice and suppress cation mixing[95], [97]. However, in NCM compositions with higher nickel content, the extent of cation mixing and its possible reduction through washing, sintering, or coating may become more pronounced[191].

SEM images (fig. 3.7) reveal that neither washing, sintering, or combining both has a noticeable impact on the particle size or surface morphology of the NCM111 active material. Additionally, the average sizes of both primary and secondary particles remain unchanged across the pristine, reference, and coated samples. The particle size distributions for all three sample types are shown in fig. 3.8. The absence of any visible thick coating on the surface of the coated NCM111 particles aligns with expectations, as the targeted coating thickness is in the nanometer range. This also implies that any surface impurities present on the NCM111, potentially removed in the reference sample, are not substantial enough to be detected at this resolution.

[*] Author's original publication

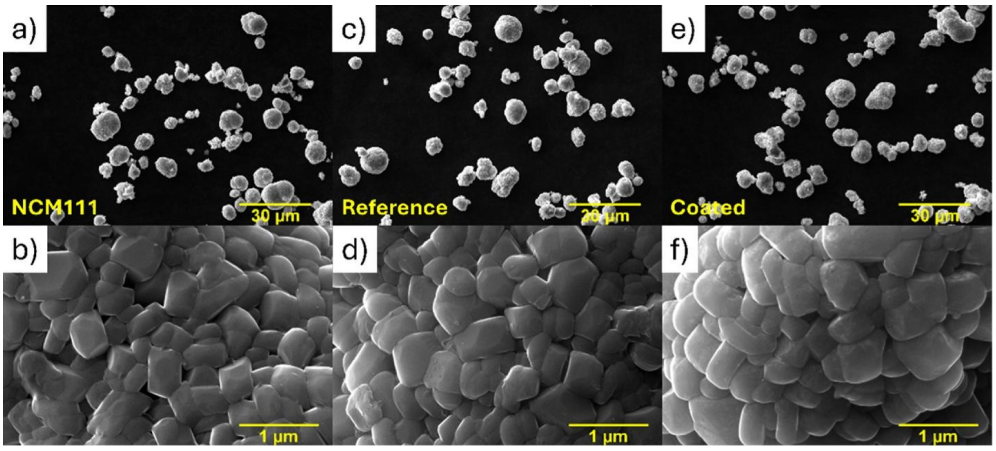

Fig. 3.7. SEM images of pristine (a,b), reference (c,d), and coated (e,f) NCM111 material[147]*.

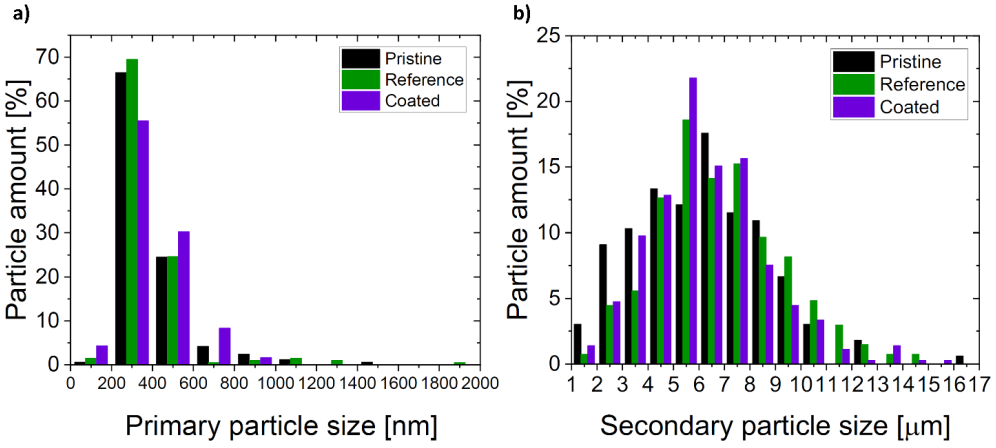

Fig. 3.8. Primary (a) and secondary (b) particle size distribution of pristine, reference, and coated NCM111[147]*.

The presence of a nanometer-scale coating is confirmed through STEM-EDS analysis (fig. 3.9). In the STEM bright field image (fig. 3.9a), the edge of a secondary particle is shown with a visible Al-containing coating approximately 10 nm thick. The red line in fig. 3.9a indicates the path along which the EDS line spectrum was collected spanning about 27 nm, with drift correction and approximately one spectrum captured per nanometer. As illustrated in the EDS line profile

* Author's original publication.

(fig. 3.9b), a clear decrease in Ni, Mn, and Co X-ray counts coincides with a rise in Al counts, demonstrating that the coating is localized on the particle's surface. The increase in Al signal within the 10–20 nm range of the profile further confirms the coating thickness. Additionally, fig. 3.9c presents the integrated line profile spectrum, where Al is distinctly visible, along with strong Ga and Pt signals originating from the protective layer deposited for analysis.

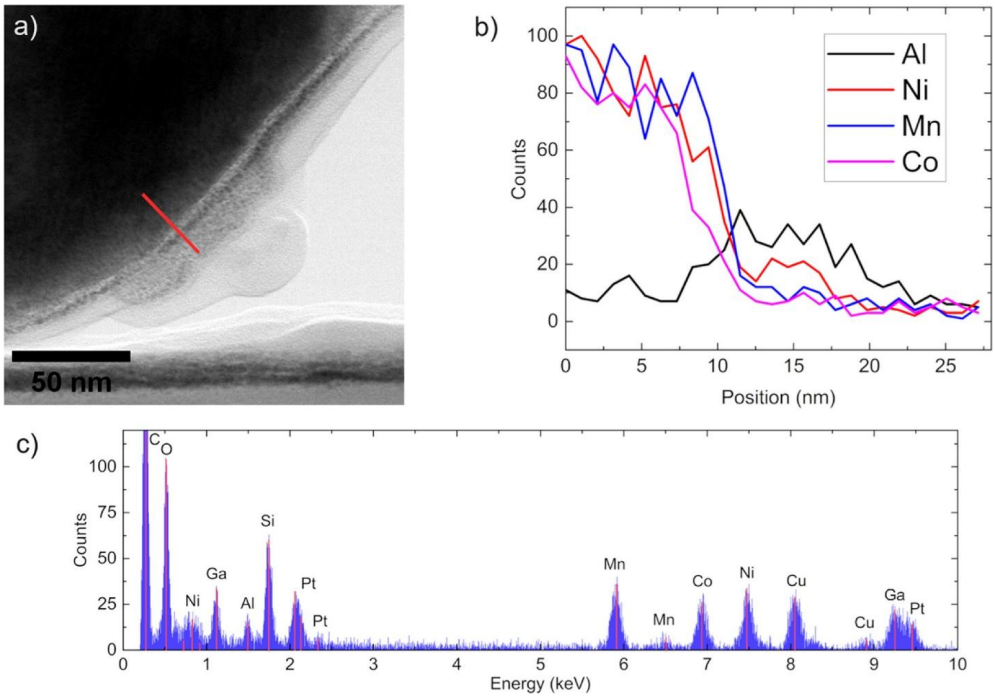

Fig. 3.9. TEM image showing the coated NCM111 sample (a); EDS line spectrum excerpt corresponding to the red line marked in image a (b); and cumulative EDS spectrum obtained along the red line in image a (c)[147]*.

As Li cannot be detected by EDS, the TEM-EDS analysis only confirms the presence of Al on the surface of the particle. However, based on Li diffusion at high temperatures into the Al_2O_3 layer[192], [193], it can be deduced that the coating on top of the particle is in fact $LiAlO_2$.

XPS analysis of the pristine, reference, washed, sintered, and coated samples (fig. 3.10) highlights the changes in surface chemistry as the sample is modified. In the XPS overview all samples exhibit the characteristic peaks of Ni, Co, and Mn associated with the NCM cathode material, as seen in fig. 3.10a. Notably, only the coated sample displays a distinct band near

* Author's original publication.

73.2 eV, corresponding to Al_2O_3 or $LiAlO_2$[192](fig. 3.10d), a feature absent in the reference and other samples. The intensity of the Al 2p peak diminishes with progressive etching, indicating that aluminum is predominantly concentrated on the surface, again confirming little to no Al diffusion into the bulk of the material. A surface-localized coating with the composition $LiAlO_2$ is consistent with expected chemical transformations during the sintering stage, where lithium from the NCM material can diffuse into the Al_2O_3 layer at elevated temperatures, forming $LiAlO_2$[194], [195].

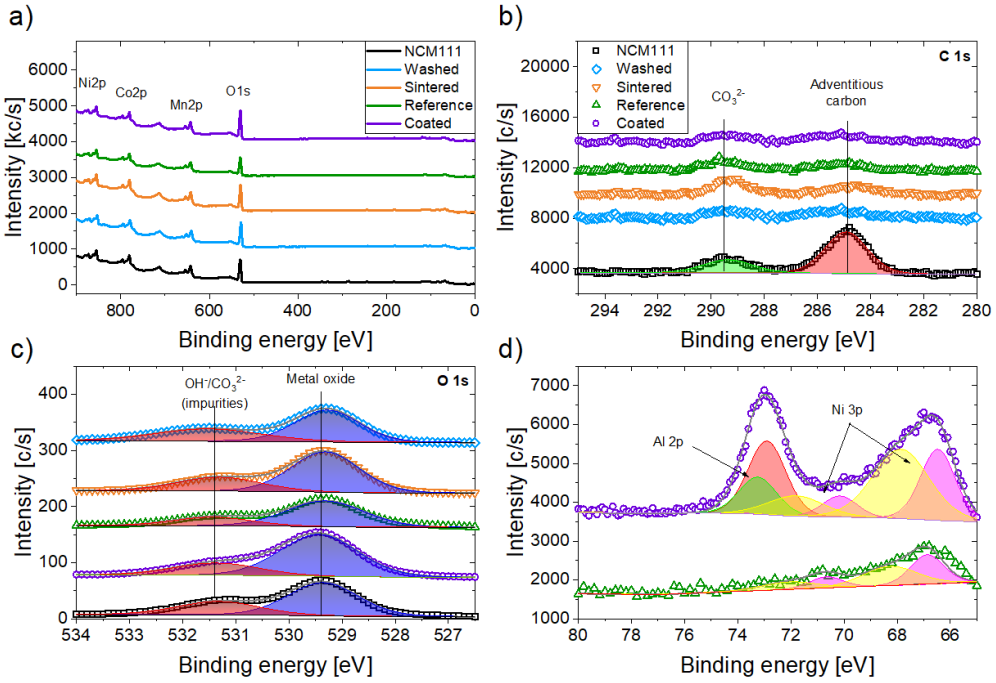

Fig. 3.10. XPS characterization of the synthesized materials. Survey spectra (a), C 1s spectra (b), and O 1s spectra (c) for pristine, reference, washed, sintered, and coated NCM111 samples. Al 2p spectra (d) is depicted for only reference and coated materials and shows that the coated NCM111 displays a clearly distinguishable Al 2p peak[147]*.

In the oxygen binding energy region of the XPS spectra (fig. 3.10c), two distinct peaks are observed at approximately 529.5 eV and 531.5 eV across all samples. These peaks correspond to lattice oxygen within the metal oxide framework of the NCM material and to surface impurities such as hydroxide (OH^-) and carbonate (CO_3^{2-}), respectively[196], [197]. In the coated sample, the

* Author's original publication.

metal oxide peak also includes contributions from the Al_2O_3 coating, making it slightly more prominent compared to the pristine and reference samples.

Carbonate impurities present on the surface of active material particles can negatively impact battery performance by contributing to CEI formation and accelerating electrolyte degradation. Therefore, analyzing the carbon content in different samples can provide useful insights into the ageing mechanisms. The carbon XPS spectra (fig. 3.10b) exhibits two distinct peaks: one at 284.8 eV corresponding to adventitious carbon (hydrocarbons adsorbed from air exposure) and another at 289.4 eV associated with surface carbonates. Among all the samples, the pristine NCM111 shows the highest intensity for the adventitious carbon peak, indicating a greater presence of surface-adsorbed hydrocarbons. Upon modification through washing, sintering, or both, this adventitious carbon signal significantly decreases, while the carbonate peak becomes more pronounced in comparison. Notably, the coated sample displays the weakest carbonate signal, likely due to surface coverage by $Al_2O_3/LiAlO_2$, which limits exposure. Conversely, the washed sample shows the most intense carbonate peak, even exceeding that of the adventitious carbon. This may be attributed to the ethanol washing step conducted in ambient air – since ethanol is hygroscopic, it could absorb moisture and atmospheric CO_2, promoting carbonate formation on the material's surface. Whereas the sintering step in all other modified samples removes the carbonates from the surface by burning them off. Overall, a marked reduction in carbon content is observed in the sintered, reference, and coated samples.

The isotope ratio mass spectrometry (IRMS) results (fig. 3.11), used to quantify the carbon content in each sample, are consistent with the trends observed in the XPS data. According to IRMS measurements, the pristine and washed samples contain the highest levels of carbon. In contrast, sintering leads to a substantial reduction in carbon content, cutting it by roughly half. Three parallel IRMS analysis measurements were conducted on each sample, and the error bars shown in fig. 3.11 reflect the standard deviation across these three measurements.

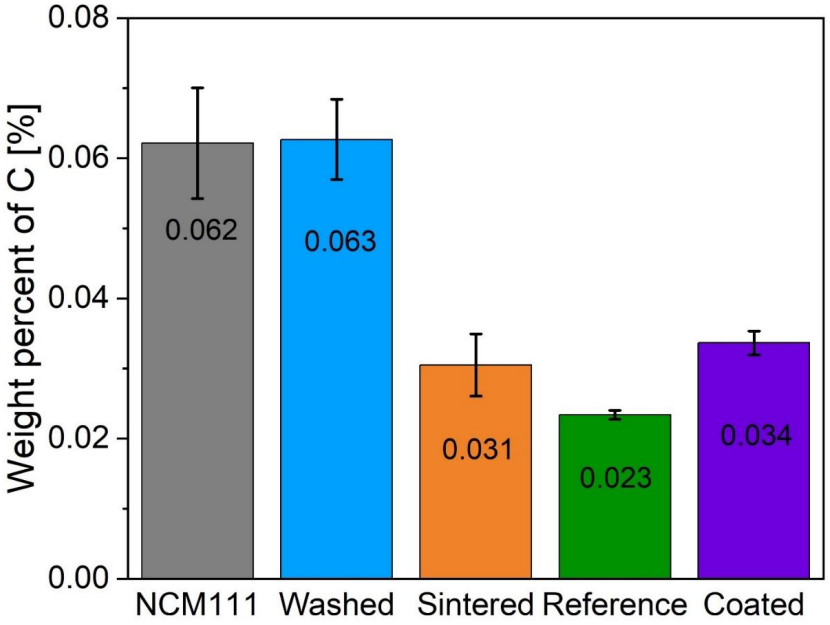

Fig. 3.11. Carbon content analysis of all samples determined by isotope ratio mass spectrometry[147]*.

To precisely determine the aluminum concentration in the samples, ICP-MS analysis was conducted (fig. 3.12). Results indicate an Al content of 0.2 wt.% or 0.8 mol.%, suggesting that roughly 10 % of the aluminum introduced via AIP is successfully converted into Al_2O_3 or $LiAlO_2$ during synthesis. Additionally, a minor deficiency in Mn was consistently observed across all NCM samples. Based on the measured quantities of Li, Ni, Co, and Mn, the resulting stoichiometry is calculated as $Li_{1.07}(Ni_{0.36}Co_{0.35}Mn_{0.29})_{0.93}O_2$.

* Author's original publication.

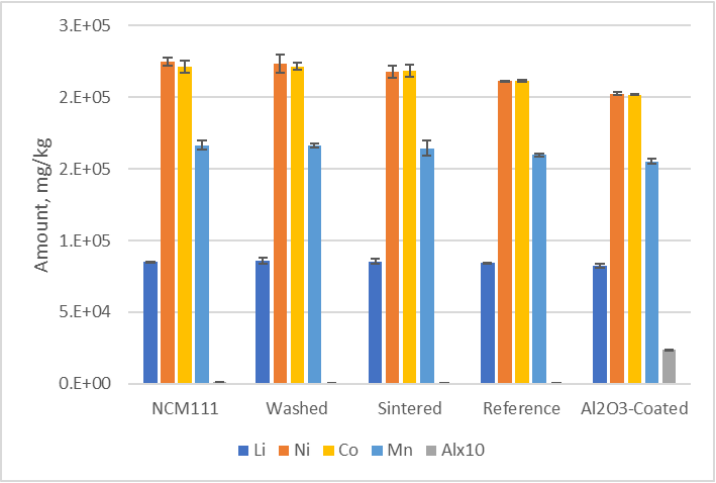

Fig. 3.12. Amount of Li, Ni, Co, Mn and Al in all samples as determined by ICP-MS analysis[147]*.

Electrochemical characterization

The charge–discharge voltage profiles of all samples at 0.1 C appear similar (fig. 3.13b), yet the rate performance data (fig. 3.13a) reveal subtle but meaningful variations in lithium-ion kinetics. Among the modifications, washing NCM111 results in a noticeable reduction in discharge capacity across the full C-rate range, with the most significant losses at higher rates (5 C, 10 C, and 20 C), indicating impaired electrode kinetics compared to the pristine sample. In contrast, sintering alone shows a minimal impact on rate capability at any C rate. Interestingly, when washing and sintering are combined (as in the reference sample), a slight synergistic improvement in capacity is observed at lower C rates (fig. 3.13a-b), although the overall rate capability remains inferior to that of the unmodified NCM111. The reduced lithium transport kinetics seen in the washed sample are also evident in the reference material. Considering the inherent variability associated with coin cell testing[184], the discharge capacities of the pristine, sintered, and coated samples may lie within experimental error margins across the entire C-rate spectrum. Notably, several other studies[129], [198], [199] have reported enhanced or preserved rate performance when applying $LiAlO_2/Al_2O_3$ coatings, despite Al_2O_3 being an electrical insulator. These improvements in kinetics have been largely attributed to reductions in internal resistance as observed in impedance spectroscopy.

* Author's original publication.

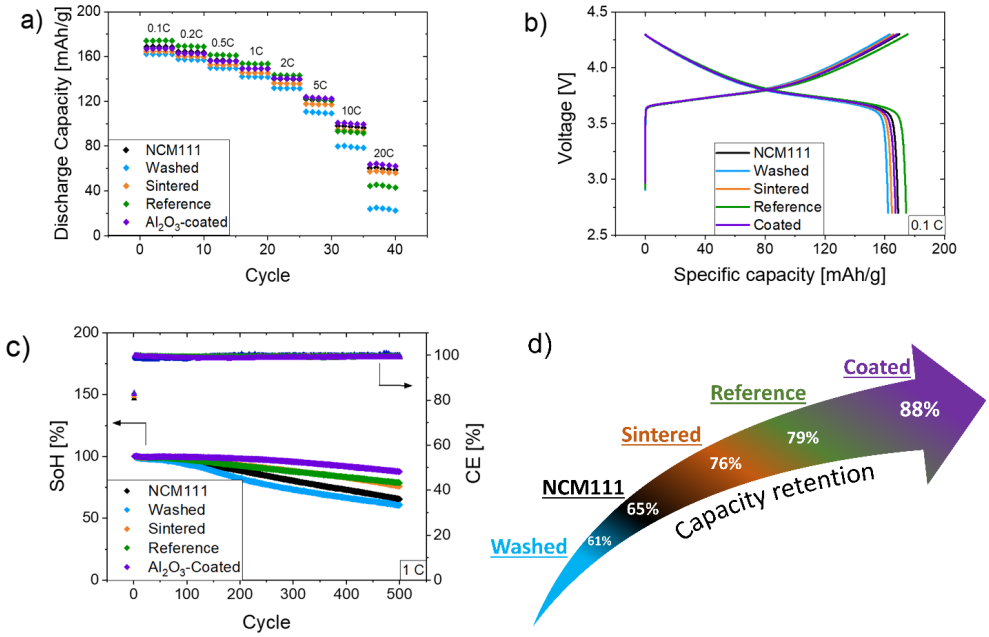

Fig. 3.13. Rate capability measurement (a), charge-discharge curves (b), cycling stability curves (c), and illustration of the capacity retention (d) of washed, pristine, sintered, reference, and coated material[147]*.

The normalized capacity fade curve (fig. 3.13c) reveals that pristine NCM111 retains only 80 % of its initial capacity within the first 300 cycles, and this drops further to approximately 65 % after 500 cycles. Such behavior is consistent with the known tendency of NCM materials to degrade rapidly during cycling. In the case of NCM111, this degradation is primarily surface-related, with capacity loss largely attributed to the formation of the CEI and other surface-level degradation processes, often intensified by surface contamination. This contrasts with higher-nickel NCM compositions like NCM811, where internal (bulk) degradation can become just as significant, if not more so, than surface deterioration[48], [163].

The impact of washing and sintering treatments on the long-term cycling performance of NCM111 was evaluated through capacity retention measurements over 500 charge-discharge cycles. When the NCM111 powder was washed with anhydrous ethanol and subsequently dried under vacuum at 80 °C overnight, a notable decline in performance was observed – capacity retention dropped to approximately 61 % after 500 cycles. Although ethanol washing has been

* Author's original publication.

reported to remove lithium residues such as LiOH from the surface[200], it does not effectively eliminate all surface contaminants. Transition metal carbonates in particular can remain on the surface and may even increase due to the material's exposure to ambient air during the washing process[56].

IRMS results indicated that the overall carbon content remained unchanged after washing, while XPS analysis (fig. 3.10b) suggested a possible increase in carbonate species. Since carbonates contribute to the formation of the CEI and promote electrolyte degradation, their presence accelerates capacity fading. Interestingly, ICP-MS analysis revealed no significant lithium loss in any of the samples, and the initial Coulombic efficiencies were comparable across all samples: 80.6 %, 83.2 %, 81.7 %, 83.0 %, and 82.7 % for the pristine, washed, sintered, reference, and coated samples, respectively. These findings align with prior studies, which report that ethanol washing removes negligible lithium[200], while sintering can reincorporate surface lithium back into the structure[3].

In contrast, sintering the NCM111 powder at 500 °C in air for four hours considerably improved capacity retention, with the sample maintaining about 76 % of its initial capacity after 500 cycles. This enhancement is likely due to the removal of surface impurities, as suggested by the reduced carbon content detected by IRMS. Moreover, high-temperature sintering may facilitate the transformation of any surface rock salt phases back into the layered structure, contributing further to the observed improvement[3].

When both treatments (washing and sintering) were combined in the reference sample, capacity retention increased slightly to 79 % after 500 cycles. The capacity fade trend of the reference sample closely mirrored that of the sintered-only sample, implying that sintering was the dominant factor improving performance. The marginal improvement in capacity retention observed in the reference sample might be explained by a slightly reduced carbon content, although experimental variability in coin cell assembly could also play a role.

After establishing an appropriate reference baseline, the performance of the coated NCM111 sample was evaluated. The coated material demonstrates a significant improvement in cycling stability, achieving 88 % state of health (SoH) after 500 full charge-discharge cycles. This clearly indicates that the protective coating offers additional benefits that cannot be replicated by washing and sintering alone. Compared to both the pristine and reference samples, the coated sample displays a slightly larger c/a lattice parameter ratio, suggesting an enhanced two-dimensional layered structure that may support improved lithium-ion mobility.

Material analysis further supports these electrochemical performance improvements. IRMS data reveal a lower carbon content in the coated sample than in the pristine NCM111, although a slightly higher level is detected compared to the reference. This may be due to the coating trapping carbon impurities on the particle surface during sintering, preventing their removal. However, since these impurities are encapsulated beneath the coating, they are not directly exposed to the electrolyte and thus do not contribute to electrolyte degradation. Moreover, the $Al_2O_3/LiAlO_2$

coating can function as a scavenger for hydrofluoric acid (HF), adding another layer of protection and contributing to enhanced long-term electrochemical performance.

When comparing the pristine and coated materials, the capacity retention rises from 65 % to 88 % SoH after 500 cycles. While this might initially be attributed solely to the inert coating layer, our findings highlight the importance of properly distinguishing the effects of each modification step. If not carefully examined, improvements arising from washing, drying, or sintering may be mistakenly credited to the coating. Our study demonstrates that sintering alone can raise the SoH from 65 % to 79 % after 500 cycles. The full coating process, however, delivers the most substantial benefit, with the $Al_2O_3/LiAlO_2$-coated samples achieving the highest capacity retention, emphasizing the importance of protective coatings in enhancing battery performance.

Summary: Wet-chemical coating on NCM111 material

This study presents a sustainable and non-toxic wet-chemical approach for applying an Al_2O_3-based coating to NCM111 cathode material. The developed method goes beyond replicating the effects of re-sintering, offering a measurable enhancement in electrochemical performance. Specifically, the $Al_2O_3/LiAlO_2$-coated NCM111 exhibits a significant increase in cycle life, retaining 88 % of its initial capacity after 500 charge-discharge cycles. This performance surpasses both the reference sample (79 % retention) and the untreated pristine material (66 % retention), highlighting the efficacy of the coating.

A detailed investigation into each modification step was carried out to understand their individual and combined effects on electrochemical behaviour. The analysis revealed that washing NCM111 with anhydrous ethanol leads to performance degradation, primarily due to the formation of additional carbonate impurities on the surface. However, subsequent sintering effectively counteracts these negative effects, restoring and even improving the capacity retention relative to the pristine sample. This emphasizes the critical importance of selecting a proper reference sample when assessing the benefits of surface coatings.

When benchmarked against the re-sintered material, the coated NCM111 clearly outperforms in terms of cycling stability. This enhancement is attributed to several factors, including preservation of the layered crystal structure, a reduction in carbonaceous surface impurities, and the presence of a protective $Al_2O_3/LiAlO_2$ layer. The coating not only acts as a barrier to electrolyte decomposition but also scavenges harmful HF species generated during battery operation, thereby mitigating surface degradation.

Taken together, the findings of this work offer a promising pathway for extending the cycle life of NCM cathode materials. The wet-chemical coating technique introduced here is especially relevant for future application in high-Ni NCM compositions, where surface instability is more pronounced. Combined with strategies such as elemental doping and microstructural optimization, this approach could significantly improve the durability and commercial viability of next-generation lithium-ion batteries.

Wet-chemical coating on NCM811

As the proposed coating method proved to bring about improvements to the cycle life of NCM111 material, some initial coating tests were carried out on state-of-art NCM material (Ni ≥ 80 % – NCM811) as well. Based on our previous findings about establishing a proper reference, NCM811 material was re-sintered. To check if the coating would increase the stability and prolong the cycle life of NCM811 material, long term electrochemical charge-discharge testing was carried out. As the coating method was not changed, in-depth structural, morphological, and chemical analysis was not performed. Additionally, cycling stability is the main indicator of the effectiveness of the coating.

Based on the previously performed meta-analysis, to most effectively protect NCM811 material from degradation both coating and doping strategies should be utilized, however, in this work we focus on coating synthesis for degradation mitigation.

The $Al_2O_3/LiAlO_2$ coating on NCM811 was deposited following the same wet-chemical synthesis procedure as for the NCM111 material. The cycling stability tests in fig. 3.14 reveal that although initial capacity remains unchanged (fig. 3.14a) some improvement can be achieved by coating the active material, increasing the SoH after 500 cycles from 44 % in the re-sintered material to 54 % in the coated material (fig. 3.14b). Although the improvement is minimal, it highlights that even though microcracking becomes a dominant degradation mechanism in NCM materials with Ni content over 80 %, surface protection is still useful. Additionally, the wet chemical coating method developed on NCM111, indeed proves to be effective, although to a lesser extent, on the NCM811 material ageing.

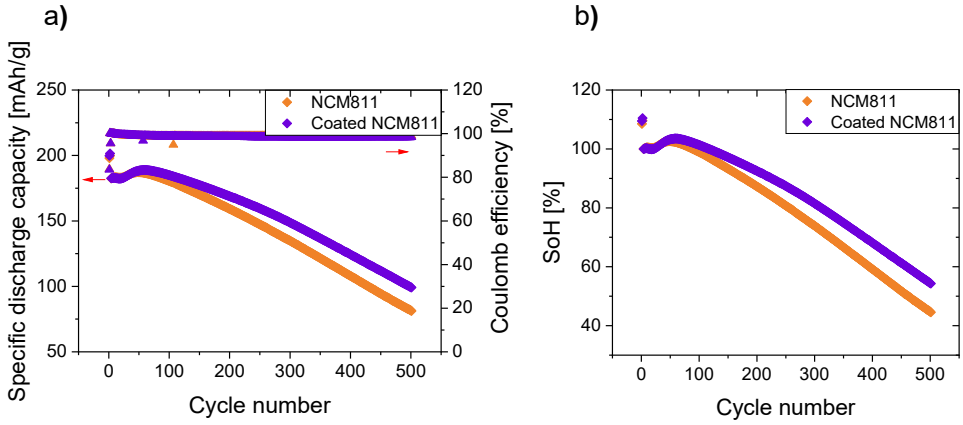

Fig. 3.14. Cycle performance of sintered and coated NCM811 material. Discharge capacity (a) and SoH (b) as a function of cycle number.

In some cases, coating synthesis can lead to surface or even bulk doping of the coated material. It was shown that for NCM111 Al diffusion into the bulk of the material during synthesis is

hindered by Mn presence in the material. In the case of NCM811 there is considerably less Mn in the lattice, and it was observed that Al diffusion is facilitated by the Ni-rich, Mn-poor environment[188], hence, some doping during sintering at high enough temperatures (800 °C) is possible in NCMs with low Mn content. In this case sintering is done at 500 °C, which may not be high enough to lead to Al doping, however, further in-depth XRD analysis of the lattice should be carried out to check if the lattice parameters are changed in accordance with Al doping.

Summary and outlook

Inert coatings on NCM materials are being developed both in research and industry. In fact, often commercial NCM materials with Ni content over 80 % are sold already coated, hence, in coating studies it is important to carry out ICP-MS or other analysis to check whether the initial material, if commercially sourced, is pure and uncoated, to get a proper reference. Besides pre-existing coating, the initial material may have degraded during storage and exposure to ambient air, thus, the wet chemical coating procedure may enhance the material performance because of the heat treatment carried out, and not because of the coating itself. This highlights another important aspect of establishing a proper reference. Only then can we certainly say that the effect on the cycle life is solely from the coating.

We developed an Al_2O_3 coating based on a sustainable, ethanol-based, wet-chemical coating procedure, which could be upscaled much easier than coatings deposited by ALD, CVD, PVD, or other techniques. Our coating demonstrated improvements to the cycle life for both NCM111 and NCM811 materials, suggesting that it could also be transferred to even higher Ni content NCMs or even other layered cathode chemistries beyond Li ion batteries.

4. CONCLUSIONS

1) Ageing in NCMs occurs both on the surface and bulk level, however, bulk degradation becomes more prominent as SoC over 80 % is reached. As for higher Ni content (≥ 80 %) NCMs 80 % SoC is reached at lower voltages (4.3 V) than for lower Ni content NCMs (~4.6 V), microcracking becomes a dominant degradation pathway for these NCMs.

2) Based on our meta-analysis, while benefits from surface protection outweigh the benefits of doping in NCM111, in NCM622 doping becomes increasingly more important in degradation mitigation, reaching equal level of importance with surface protection in NCM811. Hence, to most effectively prevent degradation in high Ni content NCMs both surface protection and doping strategies must be employed. This effect is consistent with the dominant ageing mechanisms, when charging to the same voltage (e.g. 4.3 V).

3) The voltage hysteresis of the battery cell increases as the battery cell ages as well as with increasing specific current. The SoH of the NCM811 battery half-cell can be determined from the voltage hysteresis of the charge-dicharge curve:
   a) Directly from the SoH = f(ΔV) relationship which approximates with a linear function above 70 % SoH ($R^2 = 0.9968$) and by an exponential function below 70 % SoH ($R^2 = 0.9971$).
   b) From one C rate measurement (0.1 C – 2 C), fitting the obtained data points by a BV-like function (equation (3.1)) and comparing the obtained curve against the graph in fig. 3.3c.

4) It is important to establish a proper reference in coating studies which considers the effects of the wet-chemical coating procedure (not the coating) on the material. Washing NCM with ethanol degrades performance due to carbonate impurity formation, but subsequent sintering mitigates these effects. Hence, accurate performance assessment of coatings requires careful selection of reference samples, especially when re-sintering is involved.
   a) Capacity retention of pristine (as-obtained) NCM111 material after 500 cycles at 1 C rate was 65 % whereas the material which underwent the coating procedure (without Al precursor) shows a capacity retention of 79 %.
   b) After washing the sample in ethanol (the first part of the coating procedure) capacity retention decreases to 61 %, whereas after only sintering the material at 500 °C in air the capacity retention increases to 76 % after 500 cycles at 1 C rate. This indicates that of the 2 steps involved in the coating procedure sintering brings about the most improvement to cycle life.

5) The developed wet-chemically produced $Al_2O_3/LiAlO_2$ coating brings improvements to the cycle life of NCM111 material. Capacity retention after 500 cycles at 1 C rate for the coated sample is 88 %, which is a notable improvement to the capacity retention of both the pristine (65 %) and reference (79 %) samples.

6) The same wet-chemical coating method can be used to improve the cycle life of NCM811 material. The capacity retention after 500 cycles at 1 C rate improved from 44 % in the re-sintered (reference) material to 54 % in the coated material.

7) Based on the conducted meta-analysis, in addition to the applied coating, further improvements to capacity retention in NCM811 material could be achieved by elemental doping.

REFERENCES

[1] M. Jiang, D. L. Danilov, R.-A. Eichel, and P. H. L. Notten, 'A Review of Degradation Mechanisms and Recent Achievements for Ni-Rich Cathode-Based Li-Ion Batteries', *Adv. Energy Mater.*, vol. 11, no. 48, p. 2103005, 2021, doi: 10.1002/aenm.202103005.

[2] W. Li, H. Y. Asl, Q. Xie, and A. Manthiram, 'Collapse of $LiNi_{1-x-y}Co_xMn_yO_2$ Lattice at Deep Charge Irrespective of Nickel Content in Lithium-Ion Batteries', *J. Am. Chem. Soc.*, vol. 141, no. 13, pp. 5097–5101, Apr. 2019, doi: 10.1021/jacs.8b13798.

[3] B. Huang, D. Liu, K. Qian, L. Zhang, K. Zhou, Y. Liu, F. Kang, B. Li, 'A Simple Method for the Complete Performance Recovery of Degraded Ni-rich $LiNi_{0.70}Co_{0.15}Mn_{0.15}O_2$ Cathode via Surface Reconstruction', *ACS Appl. Mater. Interfaces*, vol. 11, no. 15, pp. 14076–14084, Apr. 2019, doi: 10.1021/acsami.8b22529.

[4] P. Roy and S. K. Srivastava, 'Nanostructured anode materials for lithium ion batteries', *J. Mater. Chem. A*, vol. 3, no. 6, pp. 2454–2484, Jan. 2015, doi: 10.1039/C4TA04980B.

[5] M. S. Whittingham, 'Electrical Energy Storage and Intercalation Chemistry', *Science*, vol. 192, no. 4244, pp. 1126–1127, Jun. 1976, doi: 10.1126/science.192.4244.1126.

[6] K. Mizushima, P. C. Jones, P. J. Wiseman, and J. B. Goodenough, 'Li_xCoO_2 ($0<x<-1$): A new cathode material for batteries of high energy density', *Mater. Res. Bull.*, vol. 15, no. 6, pp. 783–789, Jun. 1980, doi: 10.1016/0025-5408(80)90012-4.

[7] A. Manthiram, 'A reflection on lithium-ion battery cathode chemistry', *Nat. Commun.*, vol. 11, no. 1, p. 1550, Mar. 2020, doi: 10.1038/s41467-020-15355-0.

[8] D. Morgan, A. Van Der Ven, and G. Ceder, 'Li Conductivity in Li_xMPO_4 (M = Mn, Fe, Co, Ni) Olivine Materials', *Electrochem. Solid-State Lett.*, vol. 7, no. 2, p. A30, 2004, doi: 10.1149/1.1633511.

[9] M. A. Kebede, N. Palaniyandy, and L. F. Koao, 'Layered, Spinel, Olivine, and Silicate as Cathode Materials for Lithium-Ion Battery', in *Electrochemical Devices for Energy Storage Applications*, CRC Press, 2019.

[10] C. Delmas, C. Fouassier, and P. Hagenmuller, 'Structural classification and properties of the layered oxides', *Phys. BC*, vol. 99, no. 1, pp. 81–85, Jan. 1980, doi: 10.1016/0378-4363(80)90214-4.

[11] L. Britala, M. Marinaro, and G. Kucinskis, 'A review of the degradation mechanisms of NCM cathodes and corresponding mitigation strategies', *J. Energy Storage*, vol. 73, p. 108875, Dec. 2023, doi: 10.1016/j.est.2023.108875.

[12] Z. Wu, C. Zhang, F. Yuan, M. Lyu, P. Yang, L. Zhang, M. Zhou, L. Wang, S. Zhang and L. Wang, 'Ni-rich cathode materials for stable high-energy lithium-ion batteries', *Nano Energy*, vol. 126, p. 109620, Jul. 2024, doi: 10.1016/j.nanoen.2024.109620.

[13] P. U. Nzereogu, A. D. Omah, F. I. Ezema, E. I. Iwuoha, and A. C. Nwanya, 'Anode materials for lithium-ion batteries: A review', *Appl. Surf. Sci. Adv.*, vol. 9, p. 100233, Jun. 2022, doi: 10.1016/j.apsadv.2022.100233.

[14] Z. Luo, Q. Xiao, G. Lei, Z. Li, and C. Tang, 'Si nanoparticles/graphene composite membrane for high performance silicon anode in lithium ion batteries', *Carbon*, vol. 98, pp. 373–380, Mar. 2016, doi: 10.1016/j.carbon.2015.11.031.

[15] S. Zhang, M. He, C.-C. Su, and Z. Zhang, 'Advanced electrolyte/additive for lithium-ion batteries with silicon anode', *Curr. Opin. Chem. Eng.*, vol. 13, pp. 24–35, Aug. 2016, doi: 10.1016/j.coche.2016.08.003.

[16] T. Yang, Y. Zhang, Y. Zhang, and R. Lin, 'Improving the conductivity of silicon anode and the stability of solid electrolyte interface by Si/Bi_2S_3 nanocomposite', *J. Energy Storage*, vol. 84, p. 110788, Apr. 2024, doi: 10.1016/j.est.2024.110788.

[17] J. Asenbauer, T. Eisenmann, M. Kuenzel, A. Kazzazi, Z. Chen, and D. Bresser, 'The success story of graphite as a lithium-ion anode material – fundamentals, remaining challenges, and recent developments including silicon (oxide) composites', *Sustain. Energy Fuels*, vol. 4, no. 11, pp. 5387–5416, 2020, doi: 10.1039/D0SE00175A.

[18] B. Rowden and N. Garcia-Araez, 'Estimating lithium-ion battery behavior from half-cell data', *Energy Rep.*, vol. 7, pp. 97–103, May 2021, doi: 10.1016/j.egyr.2021.02.048.

[19] G. A. Giffin, 'The role of concentration in electrolyte solutions for non-aqueous lithium-based batteries', *Nat. Commun.*, vol. 13, no. 1, p. 5250, Sep. 2022, doi: 10.1038/s41467-022-32794-z.

[20] Z. Fan, J. Zhang, L. Wu, H. Yu, J. Li, K. Li, and Q. Zhao, 'Solvation structure dependent ion transport and desolvation mechanism for fast-charging Li-ion batteries', *Chem. Sci.*, vol. 15, no. 41, pp. 17161–17172, 2024, doi: 10.1039/D4SC05464D.

[21] M. J. Boyer, L. Vilčiauskas, and G. S. Hwang, 'Structure and Li^+ ion transport in a mixed carbonate/$LiPF_6$ electrolyte near graphite electrode surfaces: a molecular dynamics study', *Phys. Chem. Chem. Phys.*, vol. 18, no. 40, pp. 27868–27876, Oct. 2016, doi: 10.1039/C6CP05140E.

[22] S. Lei, Z. Zeng, M. Liu, H. Zhang, S. Cheng, and J. Xie, 'Balanced solvation/de-solvation of electrolyte facilitates Li-ion intercalation for fast charging and low-temperature Li-ion batteries', *Nano Energy*, vol. 98, p. 107265, Jul. 2022, doi: 10.1016/j.nanoen.2022.107265.

[23] S. S. Zhang, 'A review on electrolyte additives for lithium-ion batteries', *J. Power Sources*, vol. 162, no. 2, pp. 1379–1394, Nov. 2006, doi: 10.1016/j.jpowsour.2006.07.074.

[24] M. Han, D. Zheng, P. Song, and Y. Ding, 'Theoretical study on fluoroethylene carbonate as an additive for the electrolyte of lithium ion batteries', *Chem. Phys. Lett.*, vol. 771, p. 138538, May 2021, doi: 10.1016/j.cplett.2021.138538.

[25] T. Sasaki, T. Abe, Y. Iriyama, M. Inaba, and Z. Ogumi, 'Suppression of an Alkyl Dicarbonate Formation in Li-Ion Cells', *J. Electrochem. Soc.*, vol. 152, no. 10, p. A2046, Aug. 2005, doi: 10.1149/1.2034517.

[26] C. J. Orendorff, 'The Role of Separators in Lithium-Ion Cell Safety', *Electrochem. Soc. Interface*, vol. 21, no. 2, p. 61, Jan. 2012, doi: 10.1149/2.F07122if.

[27] R. Stockhausen, L. Gehrlein, M. Müller, T. Bergfeldt, and A, Hofmann, 'Investigating the dominant decomposition mechanisms in lithium-ion battery cells responsible for capacity loss in different stages of electrochemical aging', *J. Power Sources*, vol. 543, p. 231842, Sep. 2022, doi: 10.1016/j.jpowsour.2022.231842.

[28] F. J. Méndez-Corbacho, D. Nieto-Castro, I. Moreno-Artabe, D. del Olmo, G. Baraldi, and E. Ayerbe, 'DEST: A Simplified Model and Automated Tool for Loss of Lithium Inventory and Loss of Active Material Estimation in Li-ion Batteries', *ChemElectroChem*, vol. 11, no. 5, p. e202300830, 2024, doi: 10.1002/celc.202300830.

[29] T. Kim, L. K. Ono, and Y. Qi, 'Understanding the active formation of a cathode–electrolyte interphase (CEI) layer with energy level band bending for lithium-ion batteries', *J. Mater. Chem. A*, vol. 11, no. 1, pp. 221–231, Dec. 2022, doi: 10.1039/D2TA07565B.

[30] A. J. Smith, Y. Fang, A. Mikheenkova, H. Ekström, and P. Svens, ‘Localized lithium plating under mild cycling conditions in high-energy lithium-ion batteries’, *J. Power Sources*, vol. 573, p. 233118, Jul. 2023, doi: 10.1016/j.jpowsour.2023.233118.

[31] D. Hu, L. Chen, J. Tian, Y. Su, N. Li, G. Chen, Y. Hu, Y. Dou, S. Chen, and F. Wu, ‘Research Progress of Lithium Plating on Graphite Anode in Lithium-Ion Batteries’, *Chin. J. Chem.*, vol. 39, no. 1, pp. 165–173, 2021, doi: 10.1002/cjoc.202000512.

[32] U. R. Koleti, A. Rajan, C. Tan, S. Moharana, T. Q. Dinh, and J. Marco, ‘A Study on the Influence of Lithium Plating on Battery Degradation’, *Energies*, vol. 13, no. 13, Art. no. 13, Jan. 2020, doi: 10.3390/en13133458.

[33] J. S. Edge, S. O'Kane, R. Prosser, N. D. Kirkaldy, A. N. Patel, A. Hales, A. Ghosh, W. Ai, J. Chen, J. Yang, S. Li, M.-C. Pang, L. B. Diaz, A. Tomaszewska, M. W. Marzook, K. N. Radhakrishnan, H. Wang, Y. Patel, B. Wu, and G. J. Offer, ‘Lithium ion battery degradation: what you need to know’, *Phys. Chem. Chem. Phys.*, vol. 23, no. 14, pp. 8200–8221, 2021, doi: 10.1039/D1CP00359C.

[34] V. Agubra and J. Fergus, ‘Lithium Ion Battery Anode Aging Mechanisms’, *Materials*, vol. 6, no. 4, pp. 1310–1325, Mar. 2013, doi: 10.3390/ma6041310.

[35] S.-H. Kim, K. Dong, H. Zhao, A. A. El-Zoka, X. Zhou, E. V. Woods, F. Giuliani, I. Manke, D. Raabe, and B. Gault, ‘Understanding the Degradation of a Model Si Anode in a Li-Ion Battery at the Atomic Scale’, *J. Phys. Chem. Lett.*, vol. 13, no. 36, pp. 8416–8421, Sep. 2022, doi: 10.1021/acs.jpclett.2c02236.

[36] J. Li, S. Wang, L. Chen, Y. Wang, H. Zhou, and J. M. Guerrero, ‘Adaptive Kalman filter and self-designed early stopping strategy optimized convolutional neural network for state of energy estimation of lithium-ion battery in complex temperature environment’, *J. Energy Storage*, vol. 83, p. 110750, Apr. 2024, doi: 10.1016/j.est.2024.110750.

[37] L. Vichard, A. Ravey, P. Venet, F. Harel, S. Pelissier, and D. Hissel, ‘A method to estimate battery SOH indicators based on vehicle operating data only’, *Energy*, vol. 225, p. 120235, Jun. 2021, doi: 10.1016/j.energy.2021.120235.

[38] S. Wang, Y. Fan, S. Jin, P. Takyi-Aninakwa, and C. Fernandez, ‘Improved anti-noise adaptive long short-term memory neural network modeling for the robust remaining useful life prediction of lithium-ion batteries’, *Reliab. Eng. Syst. Saf.*, vol. 230, p. 108920, Feb. 2023, doi: 10.1016/j.ress.2022.108920.

[39] L. Chen, S. Xie, A. M. Lopes, H. Li, X. Bao, C. Zhang, and P. Li, ‘A new SOH estimation method for Lithium-ion batteries based on model-data-fusion’, *Energy*, vol. 286, p. 129597, Jan. 2024, doi: 10.1016/j.energy.2023.129597.

[40] M.-F. Ng, J. Zhao, Q. Yan, G. J. Conduit, and Z. W. Seh, ‘Predicting the state of charge and health of batteries using data-driven machine learning’, *Nat. Mach. Intell.*, vol. 2, no. 3, Art. no. 3, Mar. 2020, doi: 10.1038/s42256-020-0156-7.

[41] B. Lu, Y. Song, Q. Zhang, J. Pan, Y.-T. Cheng, and J. Zhang, ‘Voltage hysteresis of lithium ion batteries caused by mechanical stress’, *Phys. Chem. Chem. Phys.*, vol. 18, no. 6, pp. 4721–4727, Feb. 2016, doi: 10.1039/C5CP06179B.

[42] V. J. Ovejas and A. Cuadras, ‘Effects of cycling on lithium-ion battery hysteresis and overvoltage’, *Sci. Rep.*, vol. 9, no. 1, p. 14875, Oct. 2019, doi: 10.1038/s41598-019-51474-5.

[43] V. J. Ovejas and A. Cuadras, ‘State of charge dependency of the overvoltage generated in commercial Li-ion cells’, *J. Power Sources*, vol. 418, pp. 176–185, Apr. 2019, doi: 10.1016/j.jpowsour.2019.02.046.

[44] J. Newman and N. P. Balsara, ‘Electrochemical Systems’, John Wiley & Sons, Jan. 2021.

[45] S. Ernst, T. P. Heins, N. Schlüter, and U. Schröder, ‘Capturing the Current-Overpotential Nonlinearity of Lithium-Ion Batteries by Nonlinear Electrochemical Impedance Spectroscopy (NLEIS) in Charge and Discharge Direction’, *Front. Energy Res.*, vol. 7, Dec. 2019, doi: 10.3389/fenrg.2019.00151.

[46] ‘Butler–Volmer equation’, *Wikipedia*. Jul. 20, 2024. Accessed: Feb. 02, 2025. [Online]. Available: https://en.wikipedia.org/w/index.php?title=Butler%E2%80%93Volmer_equation&oldid=1235622157

[47] T. Ohzuku and Y. Makimura, ‘Layered Lithium Insertion Material of $LiCo_{1/3}Ni_{1/3}Mn_{1/3}O_2$ for Lithium-Ion Batteries’, *Chem. Lett.*, vol. 30, no. 7, pp. 642–643, Jul. 2001, doi: 10.1246/cl.2001.642.

[48] H.-J. Noh, S. Youn, C. S. Yoon, and Y.-K. Sun, ‘Comparison of the structural and electrochemical properties of layered $Li[Ni_xCo_yMn_z]O_2$ (x = 1/3, 0.5, 0.6, 0.7, 0.8 and 0.85) cathode material for lithium-ion batteries’, *J. Power Sources*, vol. 233, pp. 121–130, Jul. 2013, doi: 10.1016/j.jpowsour.2013.01.063.

[49] L. Zhu, C. Bao, L. Xie, X. Yang, and X. Cao, ‘Review of synthesis and structural optimization of $LiNi_{1/3}Co_{1/3}Mn_{1/3}O_2$ cathode materials for lithium-ion batteries applications’, *J. Alloys Compd.*, vol. 831, p. 154864, Aug. 2020, doi: 10.1016/j.jallcom.2020.154864.

[50] M. Malik, K. H. Chan, and G. Azimi, ‘Review on the synthesis of $LiNi_xMn_yCo_{1-x-y}O_2$ (NMC) cathodes for lithium-ion batteries’, *Mater. Today Energy*, vol. 28, p. 101066, Aug. 2022, doi: 10.1016/j.mtener.2022.101066.

[51] H. Arai, S. Okada, H. Ohtsuka, M. Ichimura, and J. Yamaki, ‘Characterization and cathode performance of $Li_{1-x}Ni_{1+x}O_2$ prepared with the excess lithium method’, *Solid State Ion.*, vol. 80, no. 3, pp. 261–269, Sep. 1995, doi: 10.1016/0167-2738(95)00144-U.

[52] K. Park, J.-H. Park, S.-G. Hong, B. Choi, S. Heo, S.-W. Seo, K. Min, and J.-H. Park, ‘Re-construction layer effect of $LiNi_{0.8}Co_{0.15}Mn_{0.05}O_2$ with solvent evaporation process’, *Sci. Rep.*, vol. 7, no. 1, p. 44557, Mar. 2017, doi: 10.1038/srep44557.

[53] P. Teichert, G. G. Eshetu, H. Jahnke, and E. Figgemeier, ‘Degradation and Aging Routes of Ni-Rich Cathode Based Li-Ion Batteries’, *Batteries*, vol. 6, no. 1, Art. no. 1, Mar. 2020, doi: 10.3390/batteries6010008.

[54] J. K. Mayer, F. Huttner, C. A. Heck, D. Steckermeier, M.-W. von Horstig, and A. Kwade, ‘Investigation of Moisture Content, Structural and Electrochemical Properties of Nickel-Rich NCM Based Cathodes Processed at Ambient Atmosphere’, *J. Electrochem. Soc.*, vol. 169, no. 6, p. 060512, Jun. 2022, doi: 10.1149/1945-7111/ac7358.

[55] X. Wu, D. Ruan, S. Tan, M. Feng, B. Li, and G. Hu, ‘Effect of stirring environment humidity on electrochemical performance of nickel-rich cathode materials as lithium ion batteries’, *Ionics*, vol. 26, no. 11, pp. 5427–5434, Nov. 2020, doi: 10.1007/s11581-020-03708-0.

[56] J. Sicklinger, M. Metzger, H. Beyer, D. Pritzl, and H. A. Gasteiger, ‘Ambient Storage Derived Surface Contamination of NCM811 and NCM111: Performance Implications and Mitigation Strategies’, *J. Electrochem. Soc.*, vol. 166, no. 12, p. A2322, Jul. 2019, doi: 10.1149/2.0011912jes.

[57] L. Hartmann, D. Pritzl, H. Beyer, and H. A. Gasteiger, ‘Evidence for Li^+/H^+ Exchange during Ambient Storage of Ni-Rich Cathode Active Materials’, *J. Electrochem. Soc.*, vol. 168, no. 7, p. 070507, Jul. 2021, doi: 10.1149/1945-7111/ac0d3a.

[58] N. Mahne, S. E. Renfrew, B. D. McCloskey, and S. A. Freunberger, 'Electrochemical Oxidation of Lithium Carbonate Generates Singlet Oxygen', *Angew. Chem. Int. Ed.*, vol. 57, no. 19, pp. 5529–5533, 2018, doi: 10.1002/anie.201802277.

[59] S.-T. Myung, F. Maglia, K.-J. Park, C. S. Yoon, P. Lamp, S.-J. Kim, and Y.-K. Sun, 'Nickel-Rich Layered Cathode Materials for Automotive Lithium-Ion Batteries: Achievements and Perspectives', *ACS Energy Lett.*, vol. 2, no. 1, pp. 196–223, Jan. 2017, doi: 10.1021/acsenergylett.6b00594.

[60] L. Guo, D. B. Thornton, M. A. Koronfel, I. E. L. Stephens, and M. P. Ryan, 'Degradation in lithium ion battery current collectors', *J. Phys. Energy*, vol. 3, no. 3, p. 032015, Jul. 2021, doi: 10.1088/2515-7655/ac0c04.

[61] A. Gabryelczyk, S. Ivanov, A. Bund, and G. Lota, 'Corrosion of aluminium current collector in lithium-ion batteries: A review', *J. Energy Storage*, vol. 43, p. 103226, Nov. 2021, doi: 10.1016/j.est.2021.103226.

[62] S. L. Dreyer, A. Kondrakov, J. Janek, and T. Brezesinski, 'In situ analysis of gas evolution in liquid- and solid-electrolyte-based batteries with current and next-generation cathode materials', *J. Mater. Res.*, vol. 37, no. 19, pp. 3146–3168, Oct. 2022, doi: 10.1557/s43578-022-00586-2.

[63] K. Kleiner, C. A. Murray, C. Grosu, B. Ying, M. Winter, P. Nagel, S. Schuppler, and M. Merz, 'On the Origin of Reversible and Irreversible Reactions in $LiNi_xCo_{(1-x)/2}Mn_{(1-x)/2}O_2$', *J. Electrochem. Soc.*, vol. 168, no. 12, p. 120533, Dec. 2021, doi: 10.1149/1945-7111/ac3c21.

[64] R. Jung, M. Metzger, F. Maglia, C. Stinner, and H. A. Gasteiger, 'Oxygen Release and Its Effect on the Cycling Stability of $LiNi_xMn_yCo_zO_2$ (NMC) Cathode Materials for Li-Ion Batteries', *J. Electrochem. Soc.*, vol. 164, no. 7, p. A1361, May 2017, doi: 10.1149/2.0021707jes.

[65] A. O. Kondrakov, H. Geßwein, K. Galdina, L. de Biasi, V. Meded, E. O. Filatova, G. Schumacher, W. Wenzel, P. Hartmann, T. Brezesinski, and J. Janek, 'Charge-Transfer-Induced Lattice Collapse in Ni-Rich NCM Cathode Materials during Delithiation', *J. Phys. Chem. C*, vol. 121, no. 44, pp. 24381–24388, Nov. 2017, doi: 10.1021/acs.jpcc.7b06598.

[66] P. Yan, J. Zheng, M. Gu, J. Xiao, J.-G. Zhang, and C.-M. Wang, 'Intragranular cracking as a critical barrier for high-voltage usage of layer-structured cathode for lithium-ion batteries', *Nat. Commun.*, vol. 8, no. 1, p. 14101, Jan. 2017, doi: 10.1038/ncomms14101.

[67] K. Märker, P. J. Reeves, C. Xu, K. J. Griffith, and C. P. Grey, 'Evolution of Structure and Lithium Dynamics in $LiNi_{0.8}Mn_{0.1}Co_{0.1}O_2$ (NMC811) Cathodes during Electrochemical Cycling', *Chem. Mater.*, vol. 31, no. 7, pp. 2545–2554, Apr. 2019, doi: 10.1021/acs.chemmater.9b00140.

[68] L. You, J. Tang, Q. Wu, C. Zhang, D. Liu, T. Huang, and A. Yu, '$LiFePO_4$-coated $LiNi_{0.6}Co_{0.2}Mn_{0.2}O_2$ for lithium-ion batteries with enhanced cycling performance at elevated temperatures and high voltages', *RSC Adv.*, vol. 10, no. 62, pp. 37916–37922, Oct. 2020, doi: 10.1039/D0RA07764J.

[69] S. Yin, W. Deng, J. Chen, X. Gao, G. Zou, H. Hou, and X. Ji, 'Fundamental and solutions of microcrack in Ni-rich layered oxide cathode materials of lithium-ion batteries', *Nano Energy*, vol. 83, p. 105854, May 2021, doi: 10.1016/j.nanoen.2021.105854.

[70] A. O. Kondrakov, A. Schmidt, J. Xu, H. Geßwein, R. Mönig, P. Hartmann, H. Sommer, T. Brezesinski, and J. Janek, 'Anisotropic Lattice Strain and Mechanical Degradation of

High- and Low-Nickel NCM Cathode Materials for Li-Ion Batteries', *J. Phys. Chem. C*, vol. 121, no. 6, pp. 3286–3294, Feb. 2017, doi: 10.1021/acs.jpcc.6b12885.

[71] A. Jetybayeva, N. Schön, J. Oh, J. Kim, H. Kim, G. Park, Y.-G. Lee, R.-A. Eichel, K. Kleiner, F. Hausen, and S. Hong, 'Unraveling the State of Charge-Dependent Electronic and Ionic Structure–Property Relationships in NCM622 Cells by Multiscale Characterization', *ACS Appl. Energy Mater.*, vol. 5, no. 2, pp. 1731–1742, Feb. 2022, doi: 10.1021/acsaem.1c03173.

[72] E. Trevisanello, R. Ruess, G. Conforto, F. H. Richter, and J. Janek, 'Polycrystalline and Single Crystalline NCM Cathode Materials—Quantifying Particle Cracking, Active Surface Area, and Lithium Diffusion', *Adv. Energy Mater.*, vol. 11, no. 18, p. 2003400, 2021, doi: 10.1002/aenm.202003400.

[73] X. Zhao and G. Ceder, 'Zero-strain cathode materials for Li-ion batteries', *Joule*, vol. 6, no. 12, pp. 2683–2685, Dec. 2022, doi: 10.1016/j.joule.2022.11.012.

[74] R. Zhang, C. Wang, P. Zou, R. Lin, L. Ma, L. Yin, T. Li, W. Xu, H. Jia, Q. Li, S. Sainio, K. Kisslinger, S. E. Trask, S. N. Ehrlich, Y. Yang, A. M. Kiss, M. Ge, B. J. Polzin, S. J. Lee, W. Xu, Y. Ren, and H. L. Xin, 'Compositionally complex doping for zero-strain zero-cobalt layered cathodes', *Nature*, vol. 610, no. 7930, pp. 67–73, Oct. 2022, doi: 10.1038/s41586-022-05115-z.

[75] G.-H. Lee, J. Wu, D. Kim, K. Cho, M. Cho, W. Yang, and Y.-M. Kang, 'Reversible Anionic Redox Activities in Conventional $LiNi_{1/3}Co_{1/3}Mn_{1/3}O_2$ Cathodes', *Angew. Chem. Int. Ed.*, vol. 59, no. 22, pp. 8681–8688, 2020, doi: 10.1002/anie.202001349.

[76] A. Guéguen, D. Streich, M. He, M. Mendez, F. F. Chesneau, P. Novák, and E. J. Berg, 'Decomposition of $LiPF_6$ in High Energy Lithium-Ion Batteries Studied with Online Electrochemical Mass Spectrometry', *J. Electrochem. Soc.*, vol. 163, no. 6, p. A1095, Mar. 2016, doi: 10.1149/2.0981606jes.

[77] J. Wandt, A. T. S. Freiberg, A. Ogrodnik, and H. A. Gasteiger, 'Singlet oxygen evolution from layered transition metal oxide cathode materials and its implications for lithium-ion batteries', *Mater. Today*, vol. 21, no. 8, pp. 825–833, Oct. 2018, doi: 10.1016/j.mattod.2018.03.037.

[78] S.-K. Jung, H. Gwon, J. Hong, K.-Y. Park, D.-H. Seo, H. Kim, J. Hyun, W. Yang, and K. Kang, 'Understanding the Degradation Mechanisms of $LiNi_{0.5}Co_{0.2}Mn_{0.3}O_2$ Cathode Material in Lithium Ion Batteries', *Adv. Energy Mater.*, vol. 4, no. 1, p. 1300787, 2014, doi: 10.1002/aenm.201300787.

[79] W.-S. Yoon, M. Balasubramanian, K. Y. Chung, X.-Q. Yang, J. McBreen, C. P. Grey, and D. A. Fischer, 'Investigation of the Charge Compensation Mechanism on the Electrochemically Li-Ion Deintercalated $Li_{1-x}Co_{1/3}Ni_{1/3}Mn_{1/3}O_2$ Electrode System by Combination of Soft and Hard X-ray Absorption Spectroscopy', *J. Am. Chem. Soc.*, vol. 127, no. 49, pp. 17479–17487, Dec. 2005, doi: 10.1021/ja0530568.

[80] X.-H. Shi, Y.-P. Wang, X. Cao, S. Wu, Z. Hou, and Z. Zhu, 'Charge Compensation Mechanisms and Oxygen Vacancy Formations in $LiNi_{1/3}Co_{1/3}Mn_{1/3}O_2$: First-Principles Calculations', *ACS Omega*, vol. 7, no. 17, pp. 14875–14886, May 2022, doi: 10.1021/acsomega.2c00375.

[81] J. M. Tarascon, G. Vaughan, Y. Chabre, L. Seguin, M. Anne, P. Strobel, and G. Amatucci, '*In Situ* Structural and Electrochemical Study of $Ni_{1-x}Co_xO_2$ Metastable Oxides Prepared by Soft Chemistry', *J. Solid State Chem.*, vol. 147, no. 1, pp. 410–420, Oct. 1999, doi: 10.1006/jssc.1999.8465.

[82] B. J. Hwang, Y. W. Tsai, D. Carlier, and G. Ceder, 'A Combined Computational/Experimental Study on $LiNi_{1/3}Co_{1/3}Mn_{1/3}O_2$', *Chem. Mater.*, vol. 15, no. 19, pp. 3676–3682, Sep. 2003, doi: 10.1021/cm030299v.

[83] Y. Koyama, I. Tanaka, H. Adachi, Y. Makimura, and T. Ohzuku, 'Crystal and electronic structures of superstructural Li_{1-x} $[Co_{1/3}Ni_{1/3}Mn_{1/3}]O_2$ ($0 \leq x \leq 1$)', *J. Power Sources*, vol. 119–121, pp. 644–648, Jun. 2003, doi: 10.1016/S0378-7753(03)00194-0.

[84] A. Deb, U. Bergmann, S. P. Cramer, and E. J. Cairns, 'In situ x-ray absorption spectroscopic study of the Li $[Ni_{1/3}Co_{1/3}Mn_{1/3}]O_2$ cathode material', *J. Appl. Phys.*, vol. 97, no. 11, p. 113523, Jun. 2005, doi: 10.1063/1.1921328.

[85] C. Tian, D. Nordlund, H. L. Xin, Y. Xu, Y. Liu, D. Sokaras, F. Lin, and M. M. Doeff, 'Depth-Dependent Redox Behavior of $LiNi_{0.6}Mn_{0.2}Co_{0.2}O_2$', *J. Electrochem. Soc.*, vol. 165, no. 3, p. A696, Mar. 2018, doi: 10.1149/2.1021803jes.

[86] E. Flores, P. Novák, U. Aschauer, and E. J. Berg, 'Cation Ordering and Redox Chemistry of Layered Ni-Rich $Li_xNi_{1-2y}Co_yMn_yO_2$: An Operando Raman Spectroscopy Study', *Chem. Mater.*, vol. 32, no. 1, pp. 186–194, Jan. 2020, doi: 10.1021/acs.chemmater.9b03202.

[87] W. E. Gent, K. Lim, Y. Liang, Q. Li, T. Barnes, S.-J. Ahn, K. H. Stone, M. McIntire, J. Hong, J. H. Song, Y. Li, A. Mehta, S. Ermon, T. Tyliszczak, D. Kilcoyne, D. Vine, J.-H. Park, S.-K. Doo, M. F. Toney, W. Yang, D. Prendergast, and W. C. Chueh, 'Coupling between oxygen redox and cation migration explains unusual electrochemistry in lithium-rich layered oxides', *Nat. Commun.*, vol. 8, no. 1, p. 2091, Dec. 2017, doi: 10.1038/s41467-017-02041-x.

[88] J. Kim, H. Ma, H. Cha, H. Lee, J. Sung, M. Seo, P. Oh, M. Park, and J. Cho, 'A highly stabilized nickel-rich cathode material by nanoscale epitaxy control for high-energy lithium-ion batteries', *Energy Environ. Sci.*, vol. 11, no. 6, pp. 1449–1459, Jun. 2018, doi: 10.1039/C8EE00155C.

[89] A. Boulineau, L. Simonin, J.-F. Colin, C. Bourbon, and S. Patoux, 'First Evidence of Manganese–Nickel Segregation and Densification upon Cycling in Li-Rich Layered Oxides for Lithium Batteries', *Nano Lett.*, vol. 13, no. 8, pp. 3857–3863, Aug. 2013, doi: 10.1021/nl4019275.

[90] F. Zhang, S. Lou, Z. Yu, Q. Liu, A. Dai, C. Cao, M. F. Toney, M. Ge, X Xiao, W.-K. Lee, Y. Yao, J. Deng, T. Liu, Y. Tang, G. Yin, J. Lu, D. Su, and J. Wang, 'Surface regulation enables high stability of single-crystal lithium-ion cathodes at high voltage', *Nat. Commun.*, vol. 11, no. 1, p. 3050, Jun. 2020, doi: 10.1038/s41467-020-16824-2.

[91] C. Xu, K. Märker, J. Lee, A. Mahadevegowda, P. J. Reeves, S. J. Day, M. F. Groh, S. P. Emge, C. Ducati, B. Layla Mehdi, C. C. Tang, and C. P. Grey, 'Bulk fatigue induced by surface reconstruction in layered Ni-rich cathodes for Li-ion batteries', *Nat. Mater.*, vol. 20, no. 1, pp. 84–92, Jan. 2021, doi: 10.1038/s41563-020-0767-8.

[92] D. Streich, C. Erk, A. Guéguen, P. Müller, F.-F. Chesneau, and E. J. Berg, 'Operando Monitoring of Early Ni-mediated Surface Reconstruction in Layered Lithiated Ni–Co–Mn Oxides', *J. Phys. Chem. C*, vol. 121, no. 25, pp. 13481–13486, Jun. 2017, doi: 10.1021/acs.jpcc.7b02303.

[93] X. Zhang, W. J. Jiang, A. Mauger, Qilu, F. Gendron, and C. M. Julien, 'Minimization of the cation mixing in $Li_{1+x}(NMC)_{1-x}O_2$ as cathode material', *J. Power Sources*, vol. 195, no. 5, pp. 1292–1301, Mar. 2010, doi: 10.1016/j.jpowsour.2009.09.029.

[94] Z. Chen, J. Wang, D. Chao, T. Baikie, L. Bai, S. Chen, Y. Zhao, T. Z. Sum, J. Lin, and Z. Shen, 'Hierarchical Porous $LiNi_{1/3}Co_{1/3}Mn_{1/3}O_2$ Nano-/Micro Spherical Cathode

Material: Minimized Cation Mixing and Improved Li^+ Mobility for Enhanced Electrochemical Performance', *Sci. Rep.*, vol. 6, no. 1, p. 25771, May 2016, doi: 10.1038/srep25771.

[95] H. Zhang and J. Zhang, 'An overview of modification strategies to improve $LiNi_{0.8}Co_{0.1}Mn_{0.1}O_2$ (NCM811) cathode performance for automotive lithium-ion batteries', *eTransportation*, vol. 7, p. 100105, Feb. 2021, doi: 10.1016/j.etran.2021.100105.

[96] J. Cui, X. Ding, D. Luo, H. Xie, Z. Zhang, B. Zhang, F. Tan, C. Liu, and Z. Lin, 'Effect of Cationic Uniformity in Precursors on Li/Ni Mixing of Ni-Rich Layered Cathodes', *Energy Fuels*, vol. 35, no. 2, pp. 1842–1850, Jan. 2021, doi: 10.1021/acs.energyfuels.0c03967.

[97] L. Noerochim, S. Suwarno, N. H. Idris, and H. K. Dipojono, 'Recent Development of Nickel-Rich and Cobalt-Free Cathode Materials for Lithium-Ion Batteries', *Batteries*, vol. 7, no. 4, Art. no. 4, Dec. 2021, doi: 10.3390/batteries7040084.

[98] Z. Ruff, C. Xu, and C. P. Grey, 'Transition Metal Dissolution and Degradation in NMC811-Graphite Electrochemical Cells', *J. Electrochem. Soc.*, vol. 168, no. 6, p. 060518, Jun. 2021, doi: 10.1149/1945-7111/ac0359.

[99] D. R. Gallus, R. Schmitz, R. Wagner, B. Hoffmann, S. Nowak, I. Cekic-Laskovic, R. W. Schmitz, and M. Winter, 'The influence of different conducting salts on the metal dissolution and capacity fading of NCM cathode material', *Electrochimica Acta*, vol. 134, pp. 393–398, Jul. 2014, doi: 10.1016/j.electacta.2014.04.091.

[100] R. Jung, F. Linsenmann, R. Thomas, J. Wandt, S. Solchenbach, F. Maglia, C. Stinner, M. Tromp, and H. A. Gasteiger, 'Nickel, Manganese, and Cobalt Dissolution from Ni-Rich NMC and Their Effects on NMC622-Graphite Cells', *J. Electrochem. Soc.*, vol. 166, no. 2, p. A378, Feb. 2019, doi: 10.1149/2.1151902jes.

[101] Y.-K. Han, K. Lee, S. Kang, Y. S. Huh, and H. Lee, 'Desolvation and decomposition of metal (Mn, Co and Ni)–ethylene carbonate complexes: Relevance to battery performance', *Comput. Mater. Sci.*, vol. 81, pp. 548–550, Jan. 2014, doi: 10.1016/j.commatsci.2013.09.017.

[102] H. Zheng, Q. Sun, G. Liu, X. Song, and V. S. Battaglia, 'Correlation between dissolution behavior and electrochemical cycling performance for $LiNi_{1/3}Co_{1/3}Mn_{1/3}O_2$-based cells', *J. Power Sources*, vol. 207, pp. 134–140, Jun. 2012, doi: 10.1016/j.jpowsour.2012.01.122.

[103] H. R. Morin, D. G. Graczyk, Y. Tsai, S. Lopykinski, H. Iddir, J. C. Garcia, N. Dietz Rago, S. Trask, L. Flores, S.-B. Son, Z. Zhang, N. M. Johnson, and I. Bloom, 'Transition-Metal Dissolution from NMC-Family Oxides: A Case Study', *ACS Appl. Energy Mater.*, vol. 3, no. 3, pp. 2565–2575, Mar. 2020, doi: 10.1021/acsaem.9b02277.

[104] Y. Ahn, Y. N. Jo, W. Cho, J.-S. Yu, and K. J. Kim, 'Mechanism of Capacity Fading in the $LiNi_{0.8}Co_{0.1}Mn_{0.1}O_2$ Cathode Material for Lithium-Ion Batteries', *Energies*, vol. 12, no. 9, Art. no. 9, Jan. 2019, doi: 10.3390/en12091638.

[105] J. Wandt, A. Freiberg, R. Thomas, Y. Gorlin, A. Siebel, R. Jung, H. A. Gasteiger, and M. Tromp, 'Transition metal dissolution and deposition in Li-ion batteries investigated by operando X-ray absorption spectroscopy', *J. Mater. Chem. A*, vol. 4, no. 47, pp. 18300–18305, Nov. 2016, doi: 10.1039/C6TA08865A.

[106] L. Yang, M. Takahashi, and B. Wang, 'A study on capacity fading of lithium-ion battery with manganese spinel positive electrode during cycling', *Electrochimica Acta*, vol. 51, no. 16, pp. 3228–3234, Apr. 2006, doi: 10.1016/j.electacta.2005.09.014.

[107] C. Zhan, J. Lu, A. Jeremy Kropf, T. Wu, A. N. Jansen, Y.-K. Sun, X. Qiu, and K. Amine, 'Mn(II) deposition on anodes and its effects on capacity fade in spinel lithium manganate–carbon systems', *Nat. Commun.*, vol. 4, no. 1, p. 2437, Sep. 2013, doi: 10.1038/ncomms3437.

[108] S. Komaba, T. Itabashi, T. Ohtsuka, H. Groult, N. Kumagai, B. Kaplan, and H. Yashiro, 'Impact of 2-Vinylpyridine as Electrolyte Additive on Surface and Electrochemistry of Graphite for C/$LiMn_2O_4$ Li-Ion Cells', *J. Electrochem. Soc.*, vol. 152, no. 5, p. A937, Mar. 2005, doi: 10.1149/1.1885385.

[109] D. H. Jang, Y. J. Shin, and S. M. Oh, 'Dissolution of Spinel Oxides and Capacity Losses in 4 V Li / $Li_xMn_2O_4$ Cells', *J. Electrochem. Soc.*, vol. 143, no. 7, p. 2204, Jul. 1996, doi: 10.1149/1.1836981.

[110] M. Evertz, F. Horsthemke, J. Kasnatscheew, M. Börner, M. Winter, and S. Nowak, 'Unraveling transition metal dissolution of $Li_{1.04}Ni_{1/3}Co_{1/3}Mn_{1/3}O_2$ (NCM 111) in lithium ion full cells by using the total reflection X-ray fluorescence technique', *J. Power Sources*, vol. 329, pp. 364–371, Oct. 2016, doi: 10.1016/j.jpowsour.2016.08.099.

[111] P. M. Csernica, S. S. Kalirai, W. E. Gent, K. Lim, Y.-S. Yu, Y. Liu, S.-J. Ahn, E. Kaeli, X. Xu, K. H. Stone, A. F. Marshall, R. Sinclair, D. A. Shapiro, M. F. Toney, and W. C. Chueh, 'Persistent and partially mobile oxygen vacancies in Li-rich layered oxides', *Nat. Energy*, vol. 6, no. 6, pp. 642–652, Jun. 2021, doi: 10.1038/s41560-021-00832-7.

[112] J. L. Esbenshade and A. A. Gewirth, 'Effect of Mn and Cu Addition on Lithiation and SEI Formation on Model Anode Electrodes', *J. Electrochem. Soc.*, vol. 161, no. 4, p. A513, Jan. 2014, doi: 10.1149/2.009404jes.

[113] C. Delacourt, A. Kwong, X. Liu, R. Qiao, W. L. Yang, P. Lu, S. J. Harris, and V. Srinivasan, 'Effect of Manganese Contamination on the Solid-Electrolyte-Interphase Properties in Li-Ion Batteries', *J. Electrochem. Soc.*, vol. 160, no. 8, p. A1099, May 2013, doi: 10.1149/2.035308jes.

[114] W. Liu, P. Oh, X. Liu, M.-J. Lee, W. Cho, S. Chae, Y. Kim, and J. Cho, 'Nickel-Rich Layered Lithium Transition-Metal Oxide for High-Energy Lithium-Ion Batteries', *Angew. Chem. Int. Ed.*, vol. 54, no. 15, pp. 4440–4457, 2015, doi: 10.1002/anie.201409262.

[115] Q. Li, Y. Wang, X. Wang, X. Sun, J.-N. Zhang, X. Yu, and H. Li, 'Investigations on the Fundamental Process of Cathode Electrolyte Interphase Formation and Evolution of High-Voltage Cathodes', *ACS Appl. Mater. Interfaces*, vol. 12, no. 2, pp. 2319–2326, Jan. 2020, doi: 10.1021/acsami.9b16727.

[116] I. Takahashi, H. Kiuchi, A. Ohma, T. Fukunaga, and E. Matsubara, 'Cathode Electrolyte Interphase Formation and Electrolyte Oxidation Mechanism for Ni-Rich Cathode Materials', *J. Phys. Chem. C*, vol. 124, no. 17, pp. 9243–9248, Apr. 2020, doi: 10.1021/acs.jpcc.0c02198.

[117] Sungjemmenla, V. S. K., C. B. Soni, V. Kumar, and Z. W. Seh, 'Understanding the Cathode–Electrolyte Interphase in Lithium-Ion Batteries', *Energy Technol.*, vol. 10, no. 9, p. 2200421, 2022, doi: 10.1002/ente.202200421.

[118] J. Xing, S. Bliznakov, L. Bonville, M. Oljaca, and R. Maric, 'A Review of Nonaqueous Electrolytes, Binders, and Separators for Lithium-Ion Batteries', *Electrochem. Energy Rev.*, vol. 5, no. 4, p. 14, Sep. 2022, doi: 10.1007/s41918-022-00131-z.

[119] D. Das, S. Manna, and S. Puravankara, ‘Electrolytes, Additives and Binders for NMC Cathodes in Li-Ion Batteries—A Review’, *Batteries*, vol. 9, no. 4, Art. no. 4, Apr. 2023, doi: 10.3390/batteries9040193.

[120] Y. Jiang, Y. Bi, M. Liu, Z. Peng, L. Huai, P. Don, J. Duan, Z. Chen, X. Li, D. Wang, and Y. Zhang, ‘Improved stability of Ni-rich cathode by the substitutive cations with stronger bonds’, *Electrochimica Acta*, vol. 268, pp. 41–48, Apr. 2018, doi: 10.1016/j.electacta.2018.01.119.

[121] M. Dixit, B. Markovsky, D. Aurbach, and D. T. Major, ‘Unraveling the Effects of Al Doping on the Electrochemical Properties of $LiNi_{0.5}Co_{0.2}Mn_{0.3}O_2$ Using First Principles’, *J. Electrochem. Soc.*, vol. 164, no. 1, p. A6359, Jan. 2017, doi: 10.1149/2.0561701jes.

[122] W. Zhu, X. Huang, T. Liu, Z. Xie, Y. Wang, K. Tian, L. Bu, H. Wang, L. Gao, and J. Zhao, ‘Ultrathin Al_2O_3 Coating on $LiNi_{0.8}Co_{0.1}Mn_{0.1}O_2$ Cathode Material for Enhanced Cycleability at Extended Voltage Ranges’, *Coatings*, vol. 9, no. 2, Art. no. 2, Feb. 2019, doi: 10.3390/coatings9020092.

[123] M. R. Laskar, D. H. K. Jackson, S. Xu, R. J. Hamers, D. Morgan, and T. F. Kuech, ‘Atomic Layer Deposited MgO: A Lower Overpotential Coating for $Li[Ni_{0.5}Mn_{0.3}Co_{0.2}]O_2$ Cathode’, *ACS Appl. Mater. Interfaces*, vol. 9, no. 12, pp. 11231–11239, Mar. 2017, doi: 10.1021/acsami.6b16562.

[124] X. Li, J. Liu, M. N. Banis, A. Lushington, R. Li, M. Cai, and X. Sun, ‘Atomic layer deposition of solid-state electrolyte coated cathode materials with superior high-voltage cycling behavior for lithium ion battery application’, *Energy Environ. Sci.*, vol. 7, no. 2, pp. 768–778, Jan. 2014, doi: 10.1039/C3EE42704H.

[125] R. Tian, H. Liu, Y. Jiang, J. Chen, X. Tan, G. Liu, L. Zhang, X. Gu, Y. Guo, H. Wang, L. Sun, and W. Chu, ‘Drastically Enhanced High-Rate Performance of Carbon-Coated $LiFePO_4$ Nanorods Using a Green Chemical Vapor Deposition (CVD) Method for Lithium Ion Battery: A Selective Carbon Coating Process’, *ACS Appl. Mater. Interfaces*, vol. 7, no. 21, pp. 11377–11386, Jun. 2015, doi: 10.1021/acsami.5b01891.

[126] Y. Xu, T. Pan, F. Liu, P. Zhao, X. Jiang, and C. Xiong, ‘Surface coating and doping of single-crystal $LiNi_{0.5}Co_{0.2}Mn_{0.3}O_2$ for enhanced high-voltage electrochemical performances via Chemical Vapor Deposition’, *J. Electroanal. Chem.*, vol. 914, p. 116286, Jun. 2022, doi: 10.1016/j.jelechem.2022.116286.

[127] B. Qiu, J. Wang, Y. Xia, Z. Wei, S. Han, and Z. Liu, ‘Enhanced Electrochemical Performance with Surface Coating by Reactive Magnetron Sputtering on Lithium-Rich Layered Oxide Electrodes’, *ACS Appl. Mater. Interfaces*, vol. 6, no. 12, pp. 9185–9193, Jun. 2014, doi: 10.1021/am501293y.

[128] J. Zhu, Y. Li, L. Xue, Y. Chen, T. Lei, S. Deng, and G. Cao, ‘Enhanced electrochemical performance of Li_3PO_4 modified $Li[Ni_{0.8}Co_{0.1}Mn_{0.1}]O_2$ cathode material via lithium-reactive coating’, *J. Alloys Compd.*, vol. 773, pp. 112–120, Jan. 2019, doi: 10.1016/j.jallcom.2018.09.237.

[129] R. S. Negi, S. P. Culver, A. Mazilkin, T. Brezesinski, and M. T. Elm, ‘Enhancing the Electrochemical Performance of $LiNi_{0.70}Co_{0.15}Mn_{0.15}O_2$ Cathodes Using a Practical Solution-Based Al_2O_3 Coating’, *ACS Appl. Mater. Interfaces*, vol. 12, no. 28, pp. 31392–31400, Jul. 2020, doi: 10.1021/acsami.0c06484.

[130] M. Xu, Z. Chen, L. Li, H. Zhu, Q. Zhao, L. Xu, N. Peng, and Li Gong, ‘Highly crystalline alumina surface coating from hydrolysis of aluminum isopropoxide on lithium-rich

layered oxide', *J. Power Sources*, vol. 281, pp. 444–454, May 2015, doi: 10.1016/j.jpowsour.2015.02.019.

[131] H. Zhang, J. Xu, and J. Zhang, 'Surface-Coated $LiNi_{0.8}Co_{0.1}Mn_{0.1}O_2$ (NCM811) Cathode Materials by Al_2O_3, ZrO_2, and Li_2O-$2B_2O_3$ Thin-Layers for Improving the Performance of Lithium Ion Batteries', *Front. Mater.*, vol. 6, Nov. 2019, doi: 10.3389/fmats.2019.00309.

[132] M. Park, X. Zhang, M. Chung, G. B. Less, and A. M. Sastry, 'A review of conduction phenomena in Li-ion batteries', *J. Power Sources*, vol. 195, no. 24, pp. 7904–7929, Dec. 2010, doi: 10.1016/j.jpowsour.2010.06.060.

[133] Q. Qiu, X. Huang, Y. Chen, Y. Tan, and W. Lv, 'Al_2O_3 coated $LiNi_{1/3}Co_{1/3}Mn_{1/3}O_2$ cathode material by sol–gel method: Preparation and characterization', *Ceram. Int.*, vol. 40, no. 7, Part B, pp. 10511–10516, Aug. 2014, doi: 10.1016/j.ceramint.2014.03.023.

[134] D. Li, Y. Kato, K. Kobayakawa, H. Noguchi, and Y. Sato, 'Preparation and electrochemical characteristics of $LiNi_{1/3}Mn_{1/3}Co_{1/3}O_2$ coated with metal oxides coating', *J. Power Sources*, vol. 160, no. 2, pp. 1342–1348, Oct. 2006, doi: 10.1016/j.jpowsour.2006.02.080.

[135] J.-Z. Kong, C. Ren, G.-A. Tai, X. Zhang, A.-D. Li, D. Wu, H. Li, and F. Zhou, 'Ultrathin ZnO coating for improved electrochemical performance of $LiNi_{0.5}Co_{0.2}Mn_{0.3}O_2$ cathode material', *J. Power Sources*, vol. 266, pp. 433–439, Nov. 2014, doi: 10.1016/j.jpowsour.2014.05.027.

[136] Y. Yang, R. Dang, K. Wu, Q. Li, N. Li, X. Xiao, and Z. Hu, 'Semiconductor Material ZnO-Coated P2-Type $Na_{2/3}Ni_{1/3}Mn_{2/3}O_2$ Cathode Materials for Sodium-Ion Batteries with Superior Electrochemical Performance', *J. Phys. Chem. C*, vol. 124, no. 3, pp. 1780–1787, Jan. 2020, doi: 10.1021/acs.jpcc.9b08220.

[137] C. Qin, J.-L. Cao, J. Chen, G.-L. Dai, T.-F. Wu, Y. Chen, Y.-F. Tang, A.-D. Li, and Y. Chen, 'Improvement of electrochemical performance of nickel rich $LiNi_{0.6}Co_{0.2}Mn_{0.2}O_2$ cathode active material by ultrathin TiO_2 coating', *Dalton Trans.*, vol. 45, no. 23, pp. 9669–9675, Jun. 2016, doi: 10.1039/C6DT01764A.

[138] E. Han, Y. Li, L. Zhu, and L. Zhao, 'The effect of MgO coating on $Li_{1.17}Mn_{0.48}Ni_{0.23}Co_{0.12}O_2$ cathode material for lithium ion batteries', *Solid State Ion.*, vol. 255, pp. 113–119, Feb. 2014, doi: 10.1016/j.ssi.2013.12.018.

[139] T. Sattar, S.-J. Sim, B.-S. Jin, and H.-S. Kim, 'Improving the cycle stability and rate performance of $LiNi_{0.91}Co_{0.06}Mn_{0.03}O_2$ Ni-rich cathode material by La_2O_3 coating for Lithium-ion batteries', *Curr. Appl. Phys.*, vol. 36, pp. 176–182, Apr. 2022, doi: 10.1016/j.cap.2022.01.004.

[140] H. K. Kim, H. S. Kang, P. Santhoshkumar, J. W. Park, C. W. Ho, G. S. Sim, and C. W. Lee, 'Surface modification of Ni-rich $LiNi_{0.8}Co_{0.1}Mn_{0.1}O_2$ with perovskite $LaFeO_3$ for high voltage cathode materials', *RSC Adv.*, vol. 11, no. 35, pp. 21685–21694, Jun. 2021, doi: 10.1039/D1RA00857A.

[141] X. Xiong, Z. Wang, X. Yin, H. Guo, and X. Li, 'A modified LiF coating process to enhance the electrochemical performance characteristics of $LiNi_{0.8}Co_{0.1}Mn_{0.1}O_2$ cathode materials', *Mater. Lett.*, vol. 110, pp. 4–9, Nov. 2013, doi: 10.1016/j.matlet.2013.07.098.

[142] Y. Huang, F.-M. Jin, F.-J. Chen, and L. Chen, 'Improved cycle stability and high-rate capability of Li_3VO_4-coated $Li[Ni_{0.5}Co_{0.2}Mn_{0.3}]O_2$ cathode material under different voltages', *J. Power Sources*, vol. 256, pp. 1–7, Jun. 2014, doi: 10.1016/j.jpowsour.2014.01.003.

[143] H. Zhang, H. Zhao, J. Xu, and J. Zhang, 'Optimizing Li_2O-$2B_2O_3$ coating layer on $LiNi_{0.8}Co_{0.1}Mn_{0.1}O_2$ (NCM811) cathode material for high-performance lithium-ion batteries', *Int. J. Green Energy*, May 2020, Accessed: Feb. 02, 2025. [Online]. Available: https://www.tandfonline.com/doi/abs/10.1080/15435075.2020.1763362

[144] G. Tan, F. Wu, L. Li, R. Chen, and S. Chen, 'Coralline Glassy Lithium Phosphate-Coated $LiFePO_4$ Cathodes with Improved Power Capability for Lithium Ion Batteries', *J. Phys. Chem. C*, vol. 117, no. 12, pp. 6013–6021, Mar. 2013, doi: 10.1021/jp309724q.

[145] G.-L. Xu, Q. Liu, K. K. S. Lau, Y. Liu, X. Liu, H. Gao, X. Zhou, M. Zhuang, Y. Ren, J. Li, M. Shao, M. Ouyang, F. Pan, Z. Chen, K. Amine, and G. Chen, 'Building ultraconformal protective layers on both secondary and primary particles of layered lithium transition metal oxide cathodes', *Nat. Energy*, vol. 4, no. 6, pp. 484–494, Jun. 2019, doi: 10.1038/s41560-019-0387-1.

[146] B. Li, G. Li, D. Zhang, J. Fan, D. Chen, Y. Ge, F. Lin, C. Zheng, and L. Li, 'Unveiling the Impact of the Polypyrrole Coating Layer Thickness on the Electrochemical Performances of $LiNi_{0.5}Co_{0.2}Mn_{0.3}O_2$ in Li–Ion Battery', *ChemistrySelect*, vol. 4, no. 20, pp. 6354–6360, 2019, doi: 10.1002/slct.201901112.

[147] L. Maskova, R. Ignatans, A. Viksna, A. Sarakovskis, M. Knite, and G. Kucinskis, 'Wet-Chemical Synthesis of a Protective Coating on NCM111 Cathode: The Quantified Effects of Washing, Sintering and Coating', *J. Electrochem. Soc.*, vol. 171, no. 10, p. 100520, Oct. 2024, doi: 10.1149/1945-7111/ad8483.

[148] G. Kaur and B. D. Gates, 'Review—Surface Coatings for Cathodes in Lithium Ion Batteries: From Crystal Structures to Electrochemical Performance', *J. Electrochem. Soc.*, vol. 169, no. 4, p. 043504, Apr. 2022, doi: 10.1149/1945-7111/ac60f3.

[149] B. Han, T. Pulauskas, B. Key, C. Peebles, J. S. Park, R. F. Klie, J. T. Vaughey, and F. Dogan, 'Understanding the Role of Temperature and Cathode Composition on Interface and Bulk: Optimizing Aluminum Oxide Coatings for Li-Ion Cathodes', *ACS Appl. Mater. Interfaces*, vol. 9, no. 17, pp. 14769–14778, May 2017, doi: 10.1021/acsami.7b00595.

[150] D. Hu, F. Du, H. Cao, Q. Zhou, P. Sun, T. Xu, C. Mei, Q. Hao, Z. Fan, and J. Zheng, 'An effective strategy to control thickness of Al_2O_3 coating layer on nickel-rich cathode materials', *J. Electroanal. Chem.*, vol. 880, p. 114910, Jan. 2021, doi: 10.1016/j.jelechem.2020.114910.

[151] X. Xiong, Z. Wang, P. Yue, H. Guo, F. Wu, J. Wang, and X. Li, 'Washing effects on electrochemical performance and storage characteristics of $LiNi_{0.8}Co_{0.1}Mn_{0.1}O_2$ as cathode material for lithium-ion batteries', *J. Power Sources*, vol. 222, pp. 318–325, Jan. 2013, doi: 10.1016/j.jpowsour.2012.08.029.

[152] Y. Su, G. Chen, L. Chen, L. Li, C. Li, R. Ding, J. Liu, Z. Lu, Y. Lu, L. Bao, G. Tan, S. Chen, and F. Wu, 'Clean the Ni-Rich Cathode Material Surface With Boric Acid to Improve Its Storage Performance', *Front. Chem.*, vol. 8, Jul. 2020, doi: 10.3389/fchem.2020.00573.

[153] S. J. Shi, J. P. Tu, Y. J. Mai, Y. Q. Zhang, Y. Y. Tang, and X. L. Wang, 'Structure and electrochemical performance of CaF_2 coated $LiMn_{1/3}Ni_{1/3}Co_{1/3}O_2$ cathode material for Li-ion batteries', *Electrochimica Acta*, vol. 83, pp. 105–112, Nov. 2012, doi: 10.1016/j.electacta.2012.08.029.

[154] S. She, Y. Zhou, Z. Hong, Y. Huang, and Y. Wu, 'Surface Coating of NCM-811 Cathode Materials with g-C_3N_4 for Enhanced Electrochemical Performance', *ACS Omega*, vol. 7, no. 28, pp. 24851–24857, Jul. 2022, doi: 10.1021/acsomega.2c03074.

[155] W. Cho, S.-M. Kim, K.-W. Lee, J. H. Song, Y. N. Jo, T. Yim, H. Kim, J.-S. Kim, and Y.-J. Kim, 'Investigation of new manganese orthophosphate $Mn_3(PO_4)_2$ coating for nickel-rich $LiNi_{0.6}Co_{0.2}Mn_{0.2}O_2$ cathode and improvement of its thermal properties', *Electrochimica Acta*, vol. 198, pp. 77–83, Apr. 2016, doi: 10.1016/j.electacta.2016.03.079.

[156] L. Chen, Y. Yang, Z. Wang, Z. Lin, J. Zhang, Q. Su, Y. Chen, W. Chen, Y. Lin, and Z. Huang, 'Enhanced electrochemical performances and thermal stability of $LiNi_{1/3}Co_{1/3}Mn_{1/3}O_2$ by surface modification with YF_3', *J. Alloys Compd.*, vol. 711, pp. 462–472, Jul. 2017, doi: 10.1016/j.jallcom.2017.03.130.

[157] X. Liu, H. Li, E. Yoo, M. Ishida, and H. Zhou, 'Fabrication of $FePO_4$ layer coated $LiNi_{1/3}Co_{1/3}Mn_{1/3}O_2$: Towards high-performance cathode materials for lithium ion batteries', *Electrochimica Acta*, vol. 83, pp. 253–258, Nov. 2012, doi: 10.1016/j.electacta.2012.07.111.

[158] L. A. Riley, S. Van Atta, A. S. Cavanagh, Y. Yan, S. M. George, P. Liu, A. C. Dillon, and S.-H. Lee, 'Electrochemical effects of ALD surface modification on combustion synthesized $LiNi_{1/3}Mn_{1/3}Co_{1/3}O_2$ as a layered-cathode material', *J. Power Sources*, vol. 196, no. 6, pp. 3317–3324, Mar. 2011, doi: 10.1016/j.jpowsour.2010.11.124.

[159] Y. Kim, H. S. Kim, and S. W. Martin, 'Synthesis and electrochemical characteristics of Al_2O_3-coated $LiNi_{1/3}Co_{1/3}Mn_{1/3}O_2$ cathode materials for lithium ion batteries', *Electrochimica Acta*, vol. 52, no. 3, pp. 1316–1322, Nov. 2006, doi: 10.1016/j.electacta.2006.07.033.

[160] C. X. Ding, Y. C. Bai, X. Y. Feng, and C. H. Chen, 'Improvement of electrochemical properties of layered $LiNi_{1/3}Co_{1/3}Mn_{1/3}O_2$ positive electrode material by zirconium doping', *Solid State Ion.*, vol. 189, no. 1, pp. 69–73, May 2011, doi: 10.1016/j.ssi.2011.02.015.

[161] F. Reissig, M. A. Lange, L. Haneke, T. Placke, W. G. Zeier, M. Winter, R. Schmuch, and A. Gomez-Martin, 'Synergistic Effects of Surface Coating and Bulk Doping in Ni-Rich Lithium Nickel Cobalt Manganese Oxide Cathode Materials for High-Energy Lithium Ion Batteries', *ChemSusChem*, vol. 15, no. 4, p. e202102220, 2022, doi: 10.1002/cssc.202102220.

[162] S. Oswald, D. Pritzl, M. Wetjen, and H. A. Gasteiger, 'Novel Method for Monitoring the Electrochemical Capacitance by In Situ Impedance Spectroscopy as Indicator for Particle Cracking of Nickel-Rich NCMs: Part I. Theory and Validation', *J. Electrochem. Soc.*, vol. 167, no. 10, p. 100511, Jun. 2020, doi: 10.1149/1945-7111/ab9187.

[163] H.-H. Ryu, K.-J. Park, C. S. Yoon, and Y.-K. Sun, 'Capacity Fading of Ni-Rich $Li[Ni_xCo_yMn_{1-x-y}]O_2$ ($0.6 \leq x \leq 0.95$) Cathodes for High-Energy-Density Lithium-Ion Batteries: Bulk or Surface Degradation?', *Chem. Mater.*, vol. 30, no. 3, pp. 1155–1163, Feb. 2018, doi: 10.1021/acs.chemmater.7b05269.

[164] M. Chen, E. Zhao, D. Chen, M. Wu, S. Han, Q. Huang, L. Yang, X. Xiao, and Z. Hu, 'Decreasing Li/Ni Disorder and Improving the Electrochemical Performances of Ni-Rich $LiNi_{0.8}Co_{0.1}Mn_{0.1}O_2$ by Ca Doping', *Inorg. Chem.*, vol. 56, no. 14, pp. 8355–8362, Jul. 2017, doi: 10.1021/acs.inorgchem.7b01035.

[165] T. Weigel, F. Schipper, E. M. Erickson, F. A. Susai, B. Markovsky, and D. Aurbach, 'Structural and Electrochemical Aspects of $LiNi_{0.8}Co_{0.1}Mn_{0.1}O_2$ Cathode Materials Doped by Various Cations', *ACS Energy Lett.*, vol. 4, no. 2, pp. 508–516, Feb. 2019, doi: 10.1021/acsenergylett.8b02302.

[166] D. Zhang, Y. Liu, L. Wu, L. Feng, S. Jin, R. Zhang, and M. Jin, 'Effect of Ti ion doping on electrochemical performance of Ni-rich $LiNi_{0.8}Co_{0.1}Mn_{0.1}O_2$ cathode material', *Electrochimica Acta*, vol. 328, p. 135086, Dec. 2019, doi: 10.1016/j.electacta.2019.135086.

[167] J. Li, Y. Li, W. Yi, and P. Ma, 'Improved electrochemical performance of cathode material $LiNi_{0.8}Co_{0.1}Mn_{0.1}O_2$ by doping magnesium via co-precipitation method', *J. Mater. Sci. Mater. Electron.*, vol. 30, no. 8, pp. 7490–7496, Apr. 2019, doi: 10.1007/s10854-019-01062-0.

[168] N. Wang, Y. Zhu, J. Yao, M. Zhao, and Y. Xu, 'Improved cycling stability of Ni-rich $LiNi_{0.8}Co_{0.1}Mn_{0.1}O_2$ cathode materials by optimizing Ti doping', *Funct. Mater. Lett.*, vol. 14, no. 01, p. 2150002, Jan. 2021, doi: 10.1142/S1793604721500028.

[169] J. Huang, X. Fang, Y. Wu, L. Zhou, Y. Wang, Y. Jin, W. Dang, L. Wu, Z. Rong, X. Chen, and X. Tang, 'Enhanced electrochemical performance of $LiNi_{0.8}Co_{0.1}Mn_{0.1}O_2$ by surface modification with lithium-active MoO_3', *J. Electroanal. Chem.*, vol. 823, pp. 359–367, Aug. 2018, doi: 10.1016/j.jelechem.2018.06.035.

[170] M. Jeong, H. Kim, W. Lee, S.-J. Ahn, E. Lee, and W.-S. Yoon, 'Stabilizing effects of Al-doping on Ni-rich $LiNi_{0.80}Co_{0.15}Mn_{0.05}O_2$ cathode for Li rechargeable batteries', *J. Power Sources*, vol. 474, p. 228592, Oct. 2020, doi: 10.1016/j.jpowsour.2020.228592.

[171] L. Li, D. Wang, G. Xu, Q. Zhou, J. Ma, J. Zhang, A. Du, Z. Cui, X. Zhou, and G. Cui, 'Recent progress on electrolyte functional additives for protection of nickel-rich layered oxide cathode materials', *J. Energy Chem.*, vol. 65, pp. 280–292, Feb. 2022, doi: 10.1016/j.jechem.2021.05.049.

[172] H. Q. Pham, Y. H. Thi Tran, J. Han, and S.-W. Song, 'Roles of Nonflammable Organic Liquid Electrolyte in Stabilizing the Interface of the $LiNi_{0.8}Co_{0.1}Mn_{0.1}O_2$ Cathode at 4.5 V and Improving the Battery Performance', *J. Phys. Chem. C*, vol. 124, no. 1, pp. 175–185, Jan. 2020, doi: 10.1021/acs.jpcc.9b09960.

[173] Y. Lee, T. K. Lee, S. Kim, J. Lee, Y. Ahn, K. Kim, H. Ma, G. Park, S.-M. Lee, S. K. Kwak, and N.-S. Choi, 'Fluorine-incorporated interface enhances cycling stability of lithium metal batteries with Ni-rich NCM cathodes', *Nano Energy*, vol. 67, p. 104309, Jan. 2020, doi: 10.1016/j.nanoen.2019.104309.

[174] F. Li, J. He, J. Liu, M. Wu, Y. Hou, H. Wang, S. Qi, Q. Liu, J. Hu, and J. Ma, 'Gradient Solid Electrolyte Interphase and Lithium-Ion Solvation Regulated by Bisfluoroacetamide for Stable Lithium Metal Batteries', *Angew. Chem. Int. Ed.*, vol. 60, no. 12, pp. 6600–6608, 2021, doi: 10.1002/anie.202013993.

[175] M. Wang, Z. Peng, W. Luo, F. Ren, Z. Li, Q. Zhang, H. He, C. Ouyang, and D. Wang, 'Tailoring Lithium Deposition via an SEI-Functionalized Membrane Derived from LiF Decorated Layered Carbon Structure', *Adv. Energy Mater.*, vol. 9, no. 12, p. 1802912, 2019, doi: 10.1002/aenm.201802912.

[176] S. Chang, J. Fang, K. Liu, Z. Shen, L. Zhu, X. Jin, X. Zhang, C. Hu, H. Zhang, and A.-D. Li, 'Molecular-Layer-Deposited Zincone Films Induce the Formation of LiF-Rich Interphase for Lithium Metal Anodes', *Adv. Energy Mater.*, vol. 13, no. 12, p. 2204002, 2023, doi: 10.1002/aenm.202204002.

[177] W. Xiao, Y. Nie, C. Miao, J. Wang, Y. Tan, and M. Wen, 'Structural design of high-performance Ni-rich $LiNi_{0.83}Co_{0.11}Mn_{0.06}O_2$ cathode materials enhanced by Mg^{2+} doping and Li_3PO_4 coating for lithium ion battery', *J. Colloid Interface Sci.*, vol. 607, pp. 1071–1082, Feb. 2022, doi: 10.1016/j.jcis.2021.09.067.

[178] J. Hodakovska, L. Britala, A. Mezulis, L. Grinberga, G. Bajars, and G. Kucinskis, 'State of health as a function of voltage hysteresis in Li-ion battery half-cells', *J. Solid State Electrochem.*, Jun. 2024, doi: 10.1007/s10008-024-05944-0.

[179] J. Seok, C. N. Gannett, S.-H. Yu, and H. D. Abruña, 'Understanding the Impacts of Li Stripping Overpotentials at the Counter Electrode by Three-Electrode Coin Cell Measurements', *Anal. Chem.*, vol. 93, no. 46, pp. 15459–15467, Nov. 2021, doi: 10.1021/acs.analchem.1c03422.

[180] W. Dreyer, J. Jamnik, C. Guhlke, R. Huth, J. Moškon, and M. Gaberšček, 'The thermodynamic origin of hysteresis in insertion batteries', *Nat. Mater.*, vol. 9, no. 5, Art. no. 5, May 2010, doi: 10.1038/nmat2730.

[181] T. Katrašnik, J. Moškon, K. Zelič, I. Mele, F. Ruiz-Zepeda, and M. Gaberšček, 'Entering Voltage Hysteresis in Phase-Separating Materials: Revealing the Electrochemical Signature of the Intraparticle Phase-Separated State', *Adv. Mater.*, vol. 35, no. 31, p. 2210937, 2023, doi: 10.1002/adma.202210937.

[182] J. Lim, Y. Li, D. H. Alsem, H. So, S. C. Lee, P. Bai, D. A. Cogswell, X. Liu, N. Jin, Y.-S. Yu, N. J. Salmon, D. A. Shapiro, M. Z. Bazant, T. Tyliszczak, and W. C. Chueh, 'Origin and hysteresis of lithium compositional spatiodynamics within battery primary particles', *Science*, vol. 353, no. 6299, pp. 566–571, Aug. 2016, doi: 10.1126/science.aaf4914.

[183] Y. Li, S. Meyer, J. Lim, S. C. Lee, W. E. Gent, S. Marchesini, H. Krishnan, T. Tyliszczak, D. Shapiro, A. L. D. Kilcoyne, and W. C. Chueh, 'Effects of Particle Size, Electronic Connectivity, and Incoherent Nanoscale Domains on the Sequence of Lithiation in $LiFePO_4$ Porous Electrodes', *Adv. Mater.*, vol. 27, no. 42, pp. 6591–6597, 2015, doi: 10.1002/adma.201502276.

[184] A. Smith, P. Stüble, L. Leuthner, A. Hofmann, F. Jeschull, and L. Mereacre, 'Potential and Limitations of Research Battery Cell Types for Electrochemical Data Acquisition', *Batter. Supercaps*, vol. 6, no. 6, p. e202300080, 2023, doi: 10.1002/batt.202300080.

[185] A. Ponrouch and M. R. Palacín, 'On the impact of the slurry mixing procedure in the electrochemical performance of composite electrodes for Li-ion batteries: A case study for mesocarbon microbeads (MCMB) graphite and Co_3O_4', *J. Power Sources*, vol. 196, no. 22, pp. 9682–9688, Nov. 2011, doi: 10.1016/j.jpowsour.2011.07.045.

[186] W. Hua, B. Schwarz, M. Knapp, A. Senyshyn, A. Missiul, X. Mu, S. Wang, C. Kübel, J. R. Binder, S. Indris, and H. Ehrenberg, '(De)Lithiation Mechanism of Hierarchically Layered $LiNi_{1/3}Co_{1/3}Mn_{1/3}O_2$ Cathodes during High-Voltage Cycling', *J. Electrochem. Soc.*, vol. 166, no. 3, p. A5025, Nov. 2018, doi: 10.1149/2.0051903jes.

[187] Y. Bentaleb, I. Saadoune, K. Maher, L. Saadi, K. Fujimoto, and S. Ito, 'On the $LiNi_{0.2}Mn_{0.2}Co_{0.6}O_2$ positive electrode material', *J. Power Sources*, vol. 195, no. 5, pp. 1510–1515, Mar. 2010, doi: 10.1016/j.jpowsour.2009.09.026.

[188] B. Han, B. Key, S. H. Lapidus, J. C. Garcia, H. Iddir, J. T. Vaughey, and F. Dogan, 'From Coating to Dopant: How the Transition Metal Composition Affects Alumina Coatings on Ni-Rich Cathodes', *ACS Appl. Mater. Interfaces*, vol. 9, no. 47, pp. 41291–41302, Nov. 2017, doi: 10.1021/acsami.7b13597.

[189] S. Buta, D. Morgan, A. V. der Ven, M. K. Aydinol, and G. Ceder, 'Phase Separation Tendencies of Aluminum-Doped Transition-Metal Oxides ($LiAl_{1-x}M_xO_2$) in the α-$NaFeO_2$ Crystal Structure', *J. Electrochem. Soc.*, vol. 146, no. 12, p. 4335, Dec. 1999, doi: 10.1149/1.1392639.

[190] F. Dogan, J. T. Vaughey, H. Iddir, and B. Key, 'Direct Observation of Lattice Aluminum Environments in Li Ion Cathodes $LiNi_{1-y-z}Co_yAl_zO_2$ and Al-Doped $LiNi_xMn_yCo_zO_2$ via ^{27}Al MAS NMR Spectroscopy', *ACS Appl. Mater. Interfaces*, vol. 8, no. 26, pp. 16708–16717, Jul. 2016, doi: 10.1021/acsami.6b04516.

[191] S. Zago, L. C. Scarpetta-Pizo, J. H. Zagal, and S. Specchia, 'PGM-Free Biomass-Derived Electrocatalysts for Oxygen Reduction in Energy Conversion Devices: Promising Materials', *Electrochem. Energy Rev.*, vol. 7, no. 1, p. 1, Jan. 2024, doi: 10.1007/s41918-023-00197-3.

[192] R. S. Negi, Y. Yusim, R. Pan, S. Ahmed, K. Volz, R. Takata, F. Schmidt, A. Henss, and M. T. Elm, 'A Dry-Processed $Al_2O_3/LiAlO_2$ Coating for Stabilizing the Cathode/Electrolyte Interface in High-Ni NCM-Based All-Solid-State Batteries', *Adv. Mater. Interfaces*, vol. 9, no. 8, p. 2101428, 2022, doi: 10.1002/admi.202101428.

[193] R. S. Negi, E. Celik, R. Pan, R. Stäglich, J. Senker, and M. T. Elm, 'Insights into the Positive Effect of Post-Annealing on the Electrochemical Performance of Al_2O_3-Coated Ni-Rich NCM Cathodes for Lithium-Ion Batteries', *ACS Appl. Energy Mater.*, vol. 4, no. 4, pp. 3369–3380, Apr. 2021, doi: 10.1021/acsaem.0c03135.

[194] O. Touag, G. Coquil, M Charbonneau, G. Foran, A. Ghosh, D. Mankovsky, and M. Dollé, 'One-pot synthesis of $LiAlO_2$-coated $LiNi_{0.6}Mn_{0.2}Co_{0.2}O_2$ cathode material', *Energy Adv.*, vol. 2, no. 5, pp. 701–711, May 2023, doi: 10.1039/D3YA00061C.

[195] J. L. White, F. S. Gittleson, M. Homer, and F. El Gabaly, 'Nickel and Cobalt Oxidation State Evolution at Ni-Rich NMC Cathode Surfaces during Treatment', *J. Phys. Chem. C*, vol. 124, no. 30, pp. 16508–16514, Jul. 2020, doi: 10.1021/acs.jpcc.0c04794.

[196] R. Li, Y. Ming, W. Xiang, C. Xu, G. Feng, Y. Li, Y. Chen, Z. Wu, B. Zhong, and X. Guo, 'Structure and electrochemical performance modulation of a $LiNi_{0.8}Co_{0.1}Mn_{0.1}O_2$ cathode material by anion and cation co-doping for lithium ion batteries', *RSC Adv.*, vol. 9, no. 63, pp. 36849–36857, Nov. 2019, doi: 10.1039/C9RA07873H.

[197] X. Ren, J. Du, Z. Pu, R. Wang, L. Gan, and Z. Wu, 'Facile synthesis of Li_2MoO_4 coated $LiNi_{1/3}Co_{1/3}Mn_{1/3}O_2$ composite as a novel cathode for high-temperature lithium batteries', *Ionics*, vol. 26, no. 4, pp. 1617–1627, Apr. 2020, doi: 10.1007/s11581-020-03474-z.

[198] A. Zhou, Q. Liu, Y. Wang, W. Wang, X. Yao, W. Hu, L. Zhang, X. Yu, J. Li, and H. Li, 'Al_2O_3 surface coating on $LiCoO_2$ through a facile and scalable wet-chemical method towards high-energy cathode materials withstanding high cutoff voltages', *J. Mater. Chem. A*, vol. 5, no. 46, pp. 24361–24370, Nov. 2017, doi: 10.1039/C7TA07312G.

[199] J. Cho, Y. J. Kim, and B. Park, 'Novel $LiCoO_2$ Cathode Material with Al_2O_3 Coating for a Li Ion Cell', *Chem. Mater.*, vol. 12, no. 12, pp. 3788–3791, Dec. 2000, doi: 10.1021/cm000511k.

[200] Y. Zhou, Z. Hu, Y. Huang, Y. Wu, and Z. Hong, 'Effect of solution wash on the electrochemical performance of $LiNi_{0.8}Co_{0.1}Mn_{0.1}O_2$ cathode materials', *J. Alloys Compd.*, vol. 888, p. 161584, Dec. 2021, doi: 10.1016/j.jallcom.2021.161584.

APPROBATION

Research projects:

1. Latvian Council of Science project “Cycle life prediction of lithium-ion battery electrodes and cells, utilizing current-voltage response measurements”, project No. LZP-2020/1–0425
2. M-Era.net project "Inert Coatings for Prevention of Ageing of NMC Cathode for Lithium-Ion Batteries" (InCoatBat), Project Reference Number 10341
3. Grant from the project No 5.2.1.1.i.0/2/24/I/CFLA/003 "Implementation of consolidation and management changes at Riga Technical University, Liepaja University, Rezekne Academy of Technology, Latvian Maritime Academy and Liepaja Maritime College for the progress towards excellence in higher education, science and innovation" funded by the EU Recovery and Resilience Facility

Publications:

1. **L. Maskova**, R. Ignatans, A. Viksna, A. Sarakovskis, M. Knite, G. Kucinskis, Wet-Chemical Synthesis of a Protective Coating on NCM111 Cathode: The Quantified Effects of Washing, Sintering and Coating. J. Electrochem. Soc. 171, 100520 (2024) https://doi.org/10.1149/1945-7111/ad8483
    - Author’s contribution: L. Maskova was responsible for conceptualization including development of synthesis procedure and measurement methodology, all data curation, electrochemical measurement, SEM image and XRD data acquisition and analysis, visualization and writing of original draft, producing images except TEM result image, reviewing and editing together with co-authors to produce the finished paper.
2. J. Hodakovska, **L. Britala**, A. Mezulis, L. Grinberga, G. Bajars, G. Kucinskis, State of health as a function of voltage hysteresis in Li-ion battery half-cells. *Journal of Solid State Electrochemistry* (2024) https://doi.org/10.1007/s10008-024-05944-0
    - Author’s contribution: J. Hodakovska and L. Britala contributed equally. L. Britala was responsible for conceptualization, all data curation and analysis, methodology, visualization, producing all images, writing of original draft, review and editing of the part concerning NCM 811 cathode material.
3. **L. Britala**, M. Marinaro, G. Kucinskis, A review of the degradation mechanisms of NCM cathodes and corresponding mitigation strategies, *Journal of Energy Storage* 73 (2023) 108875. https://doi.org/10.1016/j.est.2023.108875
    - Author’s contribution: L. Britala was responsible for conceptualization including defining the subject of review, all data curation for the meta-analysis, conducting the meta-analysis, visualization and writing of original draft, producing all images, reviewing and editing together with co-authors to produce the finished paper.

Participation in conferences:

1. Britala, L., Knite, M., Kucinskis, G. Inert Coatings for Cycle Life Extension of Cathodes for Li-Ion Batteries. In: *38th Scientific Conference of ISSP UL 2022 book of abstracts*, Riga, Latvia, February 22-24, 2022. Oral presentation.
2. Britala, L., Knite, M., Kucinskis, G. Inert Coatings for Cycle Life Extension of Cathodes for Li-Ion Batteries. In: *FM&NT – NIBS 2022 book of abstracts*, Riga, Latvia, July 4-6, 2022, online: p 239. Poster presentation.
3. Britala, L., Knite, M., Kucinskis, G. Inert Coatings for Cycle Life Extension of Cathodes for Li-Ion Batteries. In: *Materials science and applied chemistry 2022 Book of abstracts*, Riga, Latvia, October 21, 2022. Oral presentation.
4. Britala, L., Knite, M., Kucinskis, G. Inert Coatings for Cycle Life Extension of Cathodes for Li-Ion Batteries. In: *73rd Annual Meeting of the International Society of Electrochemistry book of abstracts*, Xiamen, Fujian, China (online), October 23-28, 2022. Poster presentation.
5. Britala, L., Knite, M., Kucinskis, G. Fast Determination of the Stage of Ageing of Lithium-Ion Batteries Based on Simple Electrochemical Measurements. In: *39th Scientific Conference of ISSP UL 2023 book of abstracts*, Riga, Latvia, February 28 - March 2, 2023. Oral presentation.
6. Britala, L., Knite, M. & Kucinskis, G. A Facile Synthesis of Al_2O_3-Coated $LiNi_{1/3}Co_{1/3}Mn_{1/3}O_2$ with Improved Cycle Life Prepared by a Wet-Chemical Method. In: *ECS Meeting Abstracts MA2023-02, 3049*, Gothenburg, Sweden, October 8-12, 2023. Poster presentation.
7. Britala, L., Knite, M., Kucinskis, G. Ageing prevention of Li-ion batteries by Al_2O_3 coating. In: *40th Scientific Conference of ISSP UL 2024 book of abstracts*, Riga, Latvia, March 5-7, 2024. Oral presentation.
8. Britala, L., Knite, M., Kucinskis, G. Development of a wet-chemical Al_2O_3 coating synthesis on $LiNi_{0.33}Co_{0.33}Mn_{0.33}O_2$ (NCM111) electrode material for cycle life extension of Li-ion batteries. In: 8*th Baltic Electrochemistry Conference: Finding New Inspiration 2 2024 book of abstracts*, Tartu, Estonia, April 14-17, 2024. Oral presentation.
9. Britala, L., Knite, M., Kucinskis, G. Wet-Chemical Al_2O_3 Coating Synthesis for Cycle Life Extension of NCM Cathodes in Li-Ion Batteries. In: *Battery 2030+ Annual Conference 2024 book of abstracts*, Grenoble, France, May 28-29, 2024. Poster presentation.

List of sources and extracted data for the meta-analysis on coating vs. doping capacity retention improvement.

NCM111

Reference	Reference material	Modifier		Secondary particle size, µm		Electrochemical cycling parameters					Capacity retention of reference material, %		Capacity retention of treated material, %		Capacity retention improvement, %	
DOI	x in $LiNi_xCo_yMn_zO_2$	Coating material	Dopant	Pristine	Modified	T, °C	C-rate, C	I, mA/g	Lower voltage, V	Upper voltage, V	50 cycles	100 cycles	50 cycles	100 cycles	50 cycles	100 cycles
10.1016/j.jallcom.2017.03.130	0.33	YF_3	-	0.2-0.3 (SC)	0.2-0.3 (SC)	25	5	1000	3.00	4.50	86.78	74.00	96.18	93.00	10.84	25.68
10.1016/j.electacta.2012.08.029	0.33	CaF_2	-	17	25	25	0.1	28	2.50	4.50	83.20	N/A	98.10	N/A	17.91	N/A
10.1016/j.electacta.2012.08.029	0.33	CaF_2	-	17	25	25	1	280	2.50	4.50	71.80	N/A	92.40	N/A	28.69	N/A
10.1016/j.electacta.2012.08.029	0.33	CaF_2	-	17	25	25	2	560	2.50	4.50	68.90	N/A	86.90	N/A	26.12	N/A
10.1016/j.electacta.2012.08.029	0.33	CaF_2	-	17	25	25	5	1400	2.50	4.50	18.00	N/A	86.50	N/A	380.56	N/A
10.1016/j.ceramint.2014.03.023	0.33	Al2O3	-	N/A	N/A	25	1	150	3.00	4.50	74.71	58.80	98.84	97.50	32.30	65.82
10.1016/j.electacta.2012.07.111	0.33	$FePO_4$	-	N/A	N/A	N/A	N/A	150	2.80	4.50	83.11	62.00	90.91	87.70	9.38	41.45
10.1016/j.electacta.2006.07.033	0.33	Al2O3	-	10	10	N/A	1	N/A	2.80	4.50	82.30	N/A	93.90	N/A	14.09	N/A
10.1016/j.electacta.2006.07.033	0.33	$LiAlO_2$	-	10	10	N/A	1	N/A	2.80	4.50	82.30	N/A	96.70	N/A	17.50	N/A
10.1016/j.jpowsour.2012.10.065	0.33	LiF	-	5-20	5-20	RT	0.1	28	2.50	4.50	88.60	N/A	97.00	N/A	9.48	N/A
10.1016/j.jpowsour.2012.10.065	0.33	LiF	-	5-20	5-20	RT	1	280	2.50	4.50	72.60	N/A	91.10	N/A	25.48	N/A
10.1016/j.jpowsour.2012.10.065	0.33	LiF	-	5-20	5-20	RT	2	560	2.50	4.50	58.00	N/A	92.80	N/A	60.00	N/A

10.1016/j.jpowsour.2012.10.065	0.33	LiF	-	5-20	5-20	RT	5	1400	2.50	4.50	52.90	N/A	85.90	N/A	62.38	N/A
10.1016/j.jpowsour.2012.10.065	0.33	LiF	-	5-20	5-20	RT	10	2800	2.50	4.50	44.90	N/A	78.70	N/A	75.28	N/A
10.1149/1.2422890	0.33	AlF_3	-	N/A	N/A	25	0.5	80	3.00	4.50	75.00	N/A	93.00	N/A	24.00	N/A
10.1016/j.jallcom.2020.155150	0.33	B_2O_3	-	0.1-0.3 (SC)	0.1-0.3 (SC)	N/A	1	180	3.00	4.50	76.00	N/A	92.00	N/A	21.05	N/A
10.1016/j.jallcom.2020.155150	0.33	B_2O_3	-	0.1-0.3 (SC)	0.1-0.3 (SC)	N/A	2	360	3.00	4.50	74.04	74.00	87.96	86.00	18.81	16.22
10.1016/j.jpowsour.2008.08.011	0.33	SrF_2	-	1 (SC)	1 (SC)	N/A	N/A	N/A	2.50	4.60	79.30	N/A	86.90	N/A	9.58	N/A
10.1016/j.jpowsour.2006.02.080	0.33	ZrO_2	-	N/A	N/A	N/A	0.5	110	3.00	4.60	71.25	46.00	92.76	88.00	30.19	91.30
10.1016/j.jpowsour.2006.02.080	0.33	TiO_2	-	N/A	N/A	N/A	0.5	110	3.00	4.60	71.25	46.00	87.84	82.00	23.28	78.26
10.1016/j.jpowsour.2006.02.080	0.33	Al_2O_3	-	N/A	N/A	N/A	0.5	110	3.00	4.60	71.25	46.00	88.96	76.00	24.86	65.22
10.1149/1.2422890	0.33	AlF_3	-	N/A	N/A	25	0.5	80	3.00	4.60	72.00	N/A	92.00	N/A	27.78	N/A
10.1149/1945-7111/ac653d	0.33	-	W	N/A	N/A	N/A	1	160	2.75	4.30	91.55	N/A	94.04	N/A	2.72	N/A
10.1016/j.ssi.2011.02.015	0.33	-	Zr	0.7 (SC)	0.7 (SC)	25	0.5	N/A	2.80	4.50	92.30	79.20	95.87	92.70	3.87	17.05
10.1007/s11664-018-6284-8	0.33	-	Cu	0.2-0.4 (SC)	0.2-0.4 (SC)	N/A	0.2	N/A	2.50	4.50	N/A	N/A	90.30	N/A	N/A	N/A
10.1007/s11664-018-6284-8	0.33	-	Cu	0.2-0.4 (SC)	0.2-0.4 (SC)	N/A	0.5	N/A	2.50	4.50	N/A	N/A	89.90	N/A	N/A	N/A
10.1007/s11664-018-6284-8	0.33	-	Cu	0.2-0.4 (SC)	0.2-0.4 (SC)	N/A	2	N/A	2.50	4.50	N/A	N/A	75.50	N/A	N/A	N/A

10.1016/j.electacta.2018.03.029	0.33	-	Al	0.25 (SC)	0.25 (SC)	RT	0.2	40	2.80	4.50	83.16	78.95	90.27	86.00	8.55	8.93
10.1016/j.electacta.2018.03.029	0.33	-	Nb	0.25 (SC)	0.25 (SC)	RT	0.2	40	2.80	4.50	83.16	78.95	90.00	81.50	8.23	3.23
10.1016/j.jallcom.2015.04.166	0.33	-	Nb	8	8	25	1	N/A	3.00	4.60	89.40	N/A	94.10	N/A	5.26	N/A
10.1007/s10008-008-0695-z	0.33	-	Mg	5	3	N/A	0.2	32	2.80	4.60	86.60	N/A	82.10	N/A	-5.20	N/A
10.1007/s10008-008-0695-z	0.33	-	Cr	5	10	N/A	0.2	32	2.80	4.60	86.60	N/A	97.00	N/A	12.01	N/A
10.1007/s10008-008-0695-z	0.33	-	Al	5	3	N/A	0.2	32	2.80	4.60	86.60	N/A	76.40	N/A	-11.78	N/A

NCM622

Reference	Reference material	Modifier		Secondary particle size, µm		Electrochemical cycling parameters					Capacity retention of reference material, %		Capacity retention of treated material, %		Capacity retention improvement, %	
DOI	x in $LiNi_xCo_yMn_zO_2$	Coating material	Dopant	Pristine	Modified	T, °C	C-rate, C	I, mA/g	Lower voltage, V	Upper voltage, V	50 cycles	100 cycles	50 cycles	100 cycles	50 cycles	100 cycles
10.1016/j.jpowsour.2014.12.128	0.6	SiO_2	-	10	10	RT	0.5	N/A	3.00	4.30	94.00	N/A	97.00	N/A	3.19	N/A
10.1039/C6DT01764A	0.6	TiO_2	-	5	5	25	1	N/A	2.50	4.30	86.06	67.50	93.49	85.90	8.63	27.26
10.1016/j.electacta.2016.03.079	0.6	$Mn_3(PO_4)_2$	-	10	12	RT	0.5	N/A	3.00	4.30	92.60	N/A	93.30	N/A	0.76	N/A
10.1016/j.jpowsour.2014.01.061	0.6	TiO_2	-	1.3 (SC)	0.9 (SC)	RT	1	140	3.00	4.50	78.10	N/A	88.70	N/A	13.57	N/A
10.1016/j.electacta.2016.05.060	0.6	Co_3O_4	-	18	18	N/A	1	180	2.80	4.60	65.95	36.70	77.78	60.30	17.93	64.31
10.1016/j.electacta.2016.11.041	0.6	Li_2SiO_3	-	8	8	30	0.2	36	2.80	4.60	90.45	76.40	91.84	85.50	1.53	11.91

10.1016/j.electacta.2016.11.041	0.6	Li_2SiO_3	-	8	8	30	1	180	2.80	4.60	72.45	61.53	87.12	73.61	20.25	19.63
10.1016/j.electacta.2016.01.139	0.6	-	Na	15	11	RT	1	160	2.80	4.30	92.92	83.72	97.53	93.51	4.96	11.69
10.1016/j.jallcom.2016.02.119	0.6	-	Mg	3 (SC)	3 (SC)	N/A	1	160	2.80	4.30	92.54	83.90	95.30	90.80	2.99	8.22
10.1039/C5RA16633K	0.6	-	Mg	N/A	N/A	N/A	1	160	2.80	4.30	88.89	81.34	95.03	91.04	6.91	11.93
10.1039/C5RA16633K	0.6	-	Mg	N/A	N/A	N/A	1	160	2.80	4.50	83.78	73.37	92.93	88.41	10.92	20.50
10.1021/acssuschemeng.9b05560	0.6	-	Ta	10	11	25	1	180	3.00	4.50	88.83	80.10	92.13	83.60	3.72	4.37

NCM811

Reference	Reference material	Modifier		Secondary particle size, um		Electrochemical cycling parameters					Capacity retention of reference material, %			Capacity retention of treated material, %							Capacity retention improvement, %	
DOI	x in $LiNi_xCo_yMn_zO_2$	Coating material	Dopant	Pristine	Modified	T, °C	C-rate, C	I, mA/g	Lower voltage, V	Upper voltage, V	Original cycles	50 cycles	100 cycles	50 cycles	80 cycles	100 cycles	150 cycles	200 cycles	300 cycles	500 cycles	50 cycles	100 cycles
10.1016/j.jelechem.2020.114910	0.8	Al_2O_3	-	10	10	RT	1	200	2.80	4.30	82.73	97.40	92.27	99.44		99.43		95.42			2.09	7.76
10.1039/D0TA00924E	0.8	Li_2MnO_3	-	20	15	RT	0.1	20	2.70	4.30	74.00	86.93	74.00	97.01		93.00					11.60	25.68
10.1016/j.jelechem.2018.06.035	0.8	MoO3	-	12	12	25	1	200	2.80	4.30	82.60	88.82	82.60	98.79		94.80					11.23	14.77
10.1021/acsami.9b12578	0.8	CNT-Li_3PO_4	-	10	10	RT	0.5	100	3.00	4.30	50.30	95.37	85.45	94.77		93.78				84.80	-0.63	9.75
10.1021/acsami.9b12578	0.8	Li_3PO_4	-	10	10	RT	0.5	100	3.00	4.30	50.30	95.37	85.45	103.07		99.89				76.40	8.07	16.91

10.3389/fmats.2019.00309	0.8	Al_2O_3	-	3-16	3-16	25	1	180	2.80	4.30	98.89	99.50	98.89	99.77		99.61			0.27	0.73
10.3389/fmats.2019.00309	0.8	ZrO_2	-	3-16	3-16	25	1	180	2.80	4.30	98.89	99.50	98.89	99.85		99.66			0.35	0.78
10.3389/fmats.2019.00309	0.8	Li_2O-$2B_2O_3$	-	3-16	3-16	25	1	180	2.80	4.30	98.89	99.50	98.89	99.91		99.78			0.41	0.90
10.1039/C2TA00678B	0.8	V_2O_5	-	9	11	60	2	N/A	2.80	4.30	44.50	71.84	44.50	88.00		76.60			22.50	72.13
10.1039/C2TA00678B	0.8	V_2O_5	-	9	11	RT	2	N/A	2.80	4.30	58.20	91.76	85.29	94.15		88.30		77.78	2.60	3.53
10.1016/j.jallcom.2018.09.237	0.8	Li_3PO_4	-	5-10	5-10	25	1	180	3.00	4.40	86.10	93.38	86.10	96.49		92.60			3.33	7.55
10.1016/j.jallcom.2018.09.237	0.8	Li_3PO_4	-	5-10	5-10	25	8	1440	3.00	4.40	83.50	89.74	83.50	94.48		93.20			5.28	11.62
10.1007/s10008-014-2519-7	0.8	Ppy	-	9	10	25	2	360	2.80	4.50	58.00	65.88	58.00	81.67		66.00			23.96	13.79
10.1021/acsami.9b12578	0.8	Li_3PO_4	-	10	10	RT	0.5	100	3.00	4.50	35.10	94.66	77.18	97.16		89.10		57.10	2.64	15.44
10.1021/acsami.9b12578	0.8	CNT-Li_3PO_4	-	10	10	RT	0.5	100	3.00	4.50	35.10	94.66	77.18	102.88		97.12		68.60	8.69	25.82
10.1039/D1RA00857A	0.8	$LaFeO_3$	-	3	3	N/A	0.2	N/A	3.00	4.60	51.00	60.33	51.00	68.00	64.60				12.71	N/A
10.3390/coatings9020092	0.8	Al_2O_3	-	8	10	N/A	0.1	20	2.70	4.60	64.30	76.19	64.30	83.18		73.90			9.18	14.93
10.1016/j.jpowsour.2017.01.066	0.8	Li_2SiO_3	-	0.5-1 (SC)	0.5-1 (SC)	N/A	N/A	100	3.00	4.60	57.60	57.60	32.56	77.70		58.82			34.90	80.67

10.1016/j.jpowsour.2017.01.066	0.8	Li_2SiO_3	-	0.5-1 (SC)	0.5-1 (SC)	N/A	N/A	200	3.00	4.60	21.00	49.53	21.00	58.39	41.00			17.89	95.24
10.1016/j.jpowsour.2017.01.066	0.8	Li_2SiO_3	-	0.5-1 (SC)	0.5-1 (SC)	N/A	N/A	300	3.00	4.60	6.00	23.16	6.00	55.46	32.00			139.50	433.33
10.1021/acs.inorgchem.7b01035	0.8	-	Ca	N/A	N/A	RT	N/A	32	3.00	4.30	68.72	68.72	N/A	81.10				18.02	N/A
10.1021/acsenergylett.8b02302	0.8	-	Al	N/A	N/A	45	0.33	60	2.80	4.30	53.00	85.93	53.00	93.94	72.00			9.32	35.85
10.1021/acsenergylett.8b02302	0.8	-	Ti	N/A	N/A	45	0.33	60	2.80	4.30	53.00	85.93	53.00	93.12	74.00			8.37	39.62
10.1021/acsenergylett.8b02302	0.8	-	Mg	N/A	N/A	45	0.33	60	2.80	4.30	53.00	85.93	53.00	93.85	80.00			9.21	50.94
10.1021/acsenergylett.8b02302	0.8	-	Si	N/A	N/A	45	0.33	60	2.80	4.30	53.00	85.93	53.00	94.41	81.00			9.87	52.83
10.1021/acsenergylett.8b02302	0.8	-	Zr	N/A	N/A	45	0.33	60	2.80	4.30	53.00	85.93	53.00	96.26	86.00			12.02	62.26
10.1021/acsenergylett.8b02302	0.8	-	Ta	N/A	N/A	45	0.33	60	2.80	4.30	53.00	85.93	53.00	99.51	90.00			15.80	69.81
10.1142/S1793604721500028	0.8	-	Ti	9	9	N/A	0.10	N/A	3.00	4.30	64.10	68.21	64.10	95.19	96.90			39.56	51.17
10.1016/j.electacta.2018.01.119	0.8	-	Ti	10	10	25	1	200	2.80	4.30	82.07	95.98	90.80	98.82	100.59	95.03		2.96	10.78
10.1016/j.electacta.2018.01.119	0.8	-	Al	10	10	25	1	200	2.80	4.30	82.07	95.98	90.80	98.84	95.38	91.95		2.99	5.03

10.1016/j.electacta.2018.01.119	0.8	-	Mg	10	10	25	1	200	2.80	4.30	82.07	95.98	90.80	97.69	94.22	85.32		1.78	3.76
10.1016/j.electacta.2018.01.119	0.8	-	Zn	10	10	25	1	200	2.80	4.30	82.07	95.98	90.80	94.67	82.84	64.23		-1.36	-8.77
10.1016/j.electacta.2019.135086	0.8	-	Ti	1-15	1-15	N/A	0.1	18	2.80	4.30	89.54	99.31	89.54	96.32	91.62			-3.01	2.32
10.1016/j.electacta.2019.135086	0.8	-	Ti	1-15	1-15	N/A	1	180	2.80	4.30	65.28	93.62	87.51	88.77	84.54	77.01		-5.18	-3.39
10.1016/j.electacta.2019.135086	0.8	-	Ti	1-15	1-15	N/A	5	900	2.80	4.30	82.79	82.79	N/A	86.54				4.53	N/A
10.1007/s10854-019-01062-0	0.8	-	Mg	10-15	10-15	N/A	1	N/A	2.50	4.30	80.85	92.93	80.85	97.81	91.88			5.25	13.64
10.1016/j.jallcom.2010.07.148	0.8	-	Cr	0.1-0.4 (SC)	0.1-0.4 (SC)	RT	5	900	2.70	4.30	76.10	76.10	N/A	89.02				16.98	N/A
10.1016/j.proci.2020.06.332	0.8	-	Dy	0.2-0.6 (SC)	0.8-1.2 (SC)	25	1	200	2.80	4.30	77.00	77.00	N/A	91.60				18.96	N/A
10.1016/j.electacta.2018.08.124	0.8	-	Al	10.1	10.8	RT	1	170	2.70	4.30	48.62	89.29	75.00	93.90	85.98	78.92		5.17	14.63
10.1016/j.ceramint.2015.02.026	0.8	-	Ti	1.9	2.3	25	1	200	2.80	4.50	63.50	90.96	84.04	95.08	91.26	86.90		4.53	8.58
10.1016/j.mtener.2019.05.003	0.8	-	Ti	10	10	N/A	1	200	2.80	4.60	70.00	81.35	70.00	92.93	84.00			14.24	20.00

N/A - information not found in reference
SC - small, single crystal agglomerated primary particles, not forming secondary particles
RT - room temperature
xx - own calculations from given capacity fade curves

Līga Maskova was born in 1995 in Riga. She obtained a Bachelor's degree in Chemistry from the University of Latvia (UL) (2019) and a Master's degree with distinction in Materials Science and Technology from the University of Tartu (2021). She has worked at the Institute of Organic Synthesis, the Institute of Chemical Physics, and the Thin-Film Technology Laboratory at the University of Tartu, holding Laboratory Technician/Specialist positions. She is currently a Researcher at the UL Institute of Solid State Physics. Her research interests include enhancing renewable energy storage capacity in next-generation lithium-ion and sodium-ion batteries, as well as reducing battery waste through effective identification and mitigation of ageing processes